ORGANIC BIOELECTRONICS: CONDUCTING POLYMERS AT THE INTERFACE WITH BIOLOGY

A Dissertation

Presented to the Faculty of the Graduate School

of Cornell University

in Partial Fulfillment of the Requirements for the Degree of

Doctor of Philosophy

by

Alwin Ming-Doug Wan

January 2013

ORGANIC BIOELECTRONICS: CONDUCTING POLYMERS AT THE INTERFACE WITH BIOLOGY

Alwin Ming-Doug Wan, Ph.D.

Cornell University 2013

Organic bioelectronics is a growing interdisciplinary research field that seeks to integrate organic electronic transducers (i.e., electrodes, electrochemical/field effect transistors) with biological systems (i.e., live cell cultures, biomaterials, and living organisms) for applications in basic research, medical diagnostics, and tissue engineering. These transducers can operate by either converting a biological signal into a measurable electrical signal (as in a biosensor), or conversely, by providing an electrical stimulus that affects the behaviour or function of a biological system. This latter approach is the focus of the work presented in this dissertation.

First, a simple planar device is described based on thin films of the conducting polymer poly(3,4-ethylenedioxythiophene) doped with *p*-toluenesulfonate (PEDOT:TOS) or poly(styrenesulfonate) (PEDOT:PSS). When a linear potential gradient is applied to this device for one hour in the presence of cell culture medium, a gradient in oxidation state is established in the PEDOT:TOS film that remains after the bias is removed. When cells of different types are cultured on such surfaces, spatial gradients are established in two types of cell behaviour: 1) Cell adhesion is modulated, enabling gradients in cell density, and spatial control over cell adhesion; and 2) Cell motility is modulated, enabling continuum control over cell migration speed and persistence.

Next, the interface mechanism is investigated by which the electrochemical

oxidation/reduction of PEDOT:TOS thin films enables the observed modulation in cell behaviour. To this end, the important adhesion and signalling protein fibronectin (Fn) is studied, with regard to how its molecular conformation is directly altered by the local electrochemical oxidation potential of the underlying PEDOT:TOS film. Conformation is assessed via Förster Resonance Energy Transfer (FRET) studies, which reveal that a linear electrical potential gradient establishes a smooth, monotonic gradient in the molecular conformation of surface-adsorbed Fn. The gradient in conformation varies from compact at the oxidized end of the film, to extended at the neutral part of the film, to partially-unfolded at the reduced end of the film. Hence, the device is demonstrated to enable precise electrical control over the molecular conformation of adsorbed fibronectin.

This device's ability to control protein conformation as an isolated parameter is then exploited to enable studies of cell secretory behaviour that are inaccessible to traditional "biology-only" experiments. The specific role of protein conformation (both fibronectin and serum proteins) in modulating the secretion of vascular endothelial growth factor (VEGF) is investigated. In particular, cells cultured on proteins in an unfolded conformation (the condition found in the tumour environment) secrete larger quantities of VEGF (with verified pro-angiogenic properties), implicating the role of altered fibronectin conformation in tumour angiogenesis.

Finally, a three-dimensional macroporous PEDOT:PSS scaffold is introduced. This scaffold represents an electrically-active, three-dimensional environment for cell culture, offering tunable pore morphology and mechanical properties, in addition to the electrochemical tunability of conductivity, surface energy, and pH demonstrated in the two-dimensional thin-film system. This

platform enables confirmation that the electrically-controllable adhesion and secretion behaviours are recapitulated in three-dimensions, and paves the way toward more complex future studies and applications with greater physiological relevance.

BIOGRAPHICAL SKETCH

Alwin Ming-Doug Wan was born and raised with brother Felix in Toronto, Ontario, Canada, by parents Yin-Lok and Tina. When asked what he wanted to be when he grew up, young Alwin thought he might be a Chemist (because to him, chemistry meant colourful liquids in Erlenmeyer flasks), or an Engineer (because Dad was an engineer). Alwin learned about and enjoyed doing many different things growing up, a trait that remains to this day. Trained in mathematics and music (violin) from an early age, he went on to develop interests during high school in physics (the stuff *not* being taught in class), followed by computer programming, and finally organic chemistry (beyond colourful liquids in Erlenmeyer flasks).

Alwin attended the University of Toronto where he earned his B.A.Sc. in 2007 from the Engineering Science program—an often-times barbaric, but ultimately worthwhile training ground for developing an engineering and scientific mindset. Through a minor concentration in nanoengineering, he developed an interest in electronic materials, and got his start in laboratory research working on flexible organic light-emitting devices (OLEDs). This was a particularly exciting first area of research because the OLEDs were bright green and eye-catching, which Alwin found exciting. This was followed by work in the amorphous silicon photovoltaics (PV) field, where he found that the devices were less eye-catching and harder to see in the dark, but were instead rather shiny (owing to the shiny nature of silicon wafers).

Alwin enrolled in graduate school at Cornell University, where he earned his M.S. and Ph.D. degrees from the Department of Materials Science and Engineering. He joined the group of George Malliaras, expecting to work on either OLEDs or PV, and promptly found himself learning to culture cells. Through

his subsequent work in trying to contribute to the fledgling field of organic bioelectronics, he found that the devices here were neither particularly shiny, nor eye-catching (unless hit with a laser), but that the work was nonetheless rewarding. Through the mentorship and collaborations of George, Claudia Fischbach, Delphine Gourdon, and Christopher Ober, Alwin discovered new and interesting ways to pursue his passion for solving problems, and developed into a halfway-decent scientist (maybe).

Outside of the laboratory, Alwin developed a passion for cycling during his years at Cornell, fueled in no small part by the beautiful (although hilly) backcountry roads in and around Ithaca, NY. He also expanded his interest in food (as well as his skills in eating it), and developed an understanding for the critical importance of having fun.

Alwin's journey to obtain more degrees than a thermometer most likely ends here, for now, at three.

Dedicated to the pursuit of knowledge; to the joy of finding things out;
and to breakfast, the most important meal of the day.

"Do things that have never been done before."

—The guy who invented the computer.

ACKNOWLEDGEMENTS

First and foremost, my unending gratitude to my parents Yin-Lok and Tina Wan, for giving me the tools and the support that have enabled me to get this far, and for always allowing me to follow the path that I wanted; and to my brother Felix, for his kind heart and shared sense of humour that perhaps only exists between siblings.

To George Malliaras, thank you for taking a chance on me five years ago, for guiding me through those early years and molding me into the scientist I am becoming, and for being a truly wonderful mentor, advisor, and friend.

To Chris Ober, thank you for adopting me into your group part way through my Ph.D., for giving me the freedom to continue my work, and for helping me overcome the most difficult frustrations of the Ph.D. process. Your experience has been invaluable.

To Claudia Fischbach, thank you for your unending patience with my (initially non-existent) background in biomedical engineering, and for your instrumental help in guiding this collaboration from the painfully-slow beginning to where it is now.

To Delphine Gourdon, thank you for arriving at Cornell with exactly the right expertise that I needed, at exactly the time that I needed it! This is a constant reminder to me of how much luck can be involved in science. Most of all, thank you for having the patience to analyze raw data with me for hours, for *really* reading my manuscripts and ultimately making them better, and for preferring to have meetings over cappuccinos at Stella's.

To Grace Kim, thank you for our incredible friendship, for your boundless generosity, and for all the adventures we've shared in mind and in spirit, on two feet and on two wheels. You are forever the winningest bacon.

To Drew "Diwu Chaeng" Cheung, thank you for being a bigger dunce than me [citation needed], for the endless laughs over the years, and for enabling my love of cycling. There are no words to describe the good conversations we've had here, mostly because they didn't consist of real words (and should get in the fridge). Somehow, ironically, mind-bogglingly, you may have done more to keep me sane than anyone else. :\?

To Miki Kunitake, thank you for being a good friend, a tolerant housemate, a scientific muse, a moral beacon, and for telling me you thought we were almost at the top of those many hills. To my many other great friends—Melissa Takahashi, Anna Legard, Brendan Murday, Giffen Maupin, Carol Newby, Lou Estevez (for never failing to give me grief about being Canadian, eh?), and Jessie Lee (sorry, no nano-toilet)—thank you for all the fun.

Finally, thank you to all of the members of the Ober, Fischbach, Gourdon, and Malliaras (both old and new) Groups, as well as my many collaborators and colleagues who have made the work environment productive and dangerously fun—Emily Brooks, Maureen (Mighty Mo) Lynch, David Infanger, Liz Welch, Dion Khodagholy, Pierre Leleux, and Leslie Jimison.

I owe you all very much—thank you.

My work has been financially supported in part by the NSF (Grant Nos. DMR-0908994 and CMMI-1031068), the NIH (Grant No. RC1 CA146065), the Cornell Center on the Microenvironment & Metastasis through the NCI

(Grant No. U54CA143876), the Cornell Center for Materials Research, and a grant from the Partner University Fund (a program of French American Cultural Exchange). I gratefully acknowledge support from the staff and facilities at the Cornell Nanobiotechnology Center, the Cornell Nanofabrication Facility, and the Cornell Imaging Facility.

TABLE OF CONTENTS

LIST OF FIGURES

CHAPTER 1

INTRODUCTION

1.1 Polymers at the Interface with Biology

Synthetic materials have long been used at the interface with biological systems, particularly in the context of human care in the form of implants and therapeutic devices. Some such devices are passive in nature, often providing some form of structural or mechanical support, such as in the cases of hip implants, bone plates/screws, dental fillings, and arterial stents. Other devices, meanwhile, actively interact with their biological surroundings in the human body, such as in the cases of a pacemaker regulating a fibrillating heart, or a dialysis machine filtering blood.

In all of these cases, a variety of synthetic materials are used in intimate contact with the body and its tissues, and the characteristics of that materials/tissue interface govern the behaviour, and the success (or failure) of the device performance.

In the realm of "active" devices or "smart" surfaces at the interface with biology, polymers offer a number of distinct advantages over their metallic and ceramic counterparts. Some of the most important advantages are: similar mechanical properties to those of tissues, tremendous opportunities for (bio-)chemical functionalization, very tunable electronic properties, ease and low cost of processing, the ability to be naturally biodegraded, and an inherent compatibility with large-area and flexible substrates.

These many advantages have already made polymers a very successful class

of materials for biological applications, and the future potential for polymer-based systems may only be limited by our progress in the development and processing of new materials and systems.

1.2 Electronics at the Interface with Biology

Electronic devices that interface with biological systems are increasingly finding applications in basic research, medical diagnostics, and tissue engineering. This coupling of biology with electronics can be thought of in two ways, somewhat crudely as *read* and *write* operations with respect to the biological system (Figure 1.1).

In the *read* approach (facilitated by a generalized biosensor), a biological input is sensed by an electronic element, which converts that input into a measurable electrical signal (e.g., current or voltage). That signal can then be analyzed for its significance (or lack thereof). In the *write* approach, an electronic element (i.e., a circuit, an electrode array, a transistor, etc.) can provide an electrical stimulus that affects the behaviour or function of a biological system. This latter approach is the focus of the work presented here.

Studying and understanding the bioelectronic interface holds interest not only from a basic research perspective, but also with an eye toward numerous applications in health care and therapeutics. In the realm of biosensors, the blood glucose sensor represents the most widely successful example to date (Figure 1.2). Commercially available and relatively cheap, it is an accurate and important diagnostic and point-of-care device for diabetic patients throughout the world. Still, even for the glucose sensor there is room for improvement both

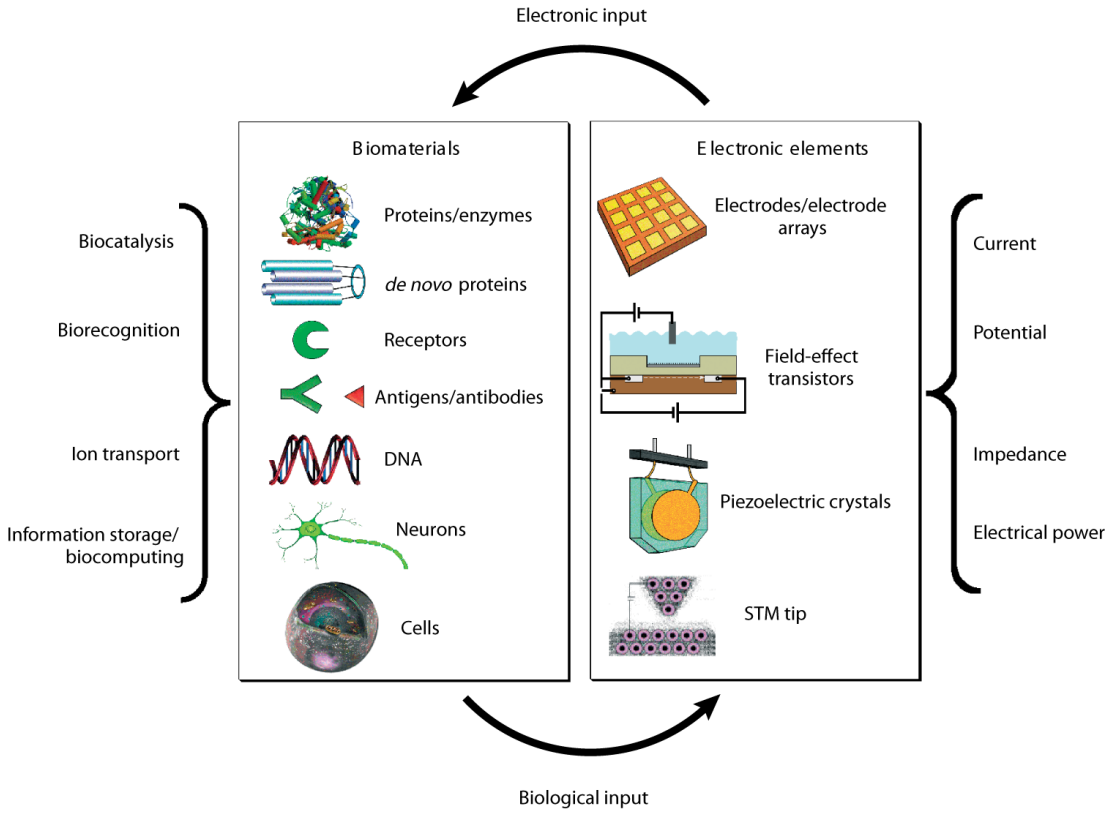

Figure 1.1: Integrated systems of biomaterials (left) and electronic systems (right) for bioelectronic applications. Reproduced with permission from *Bioelectronics: From Theory to Applications* [1].

in terms of availability and low cost, particularly with regard to wide-spread deployment and use in developing nations, where advancements in personalized and portable diagnostic devices may have the greatest benefits.

Progress also continues to be made in the design and implementation of biosensors that target a variety of other important analytes, including urea, lactose, and neurotransmitters such as dopamine and acetylcholine. Further development of such devices will serve to improve their detection capabilities and wide-spread availability at reduced costs, with perhaps the Holy Grail being a cheap, portable, customizable lab on a chip for multi-analyte sensing.

Figure 1.2: The blood glucose sensor, arguably the most successful example of a biosensor to-date. Reproduced by permission under the Creative Commons Attribution-Share Alike 3.0 Unported license.

In the realm of interfacing electronics with living tissue, the pacemaker and the cochlear implant stand out as examples of mature therapeutic technologies that can monitor and stimulate electrically-active cells. Strides continue to be made in the development of ocular implants to provide artificial vision, as well as prosthetic limbs that interface with the human nervous system—all examples of bioelectronic devices that can restore lost function for patients and greatly improve quality of life (Figure 1.3).

Much work remains to be done at the interface between electronics and living systems. While many successful examples of bioelectronic devices and systems exist, the functionality they provide, while impressive, is in many cases far less complex and complete than their natural analogs found in a healthy human body. As our materials and methods improve, along with our understanding of the bioelectronic interface, we will be able to design and implement increas-

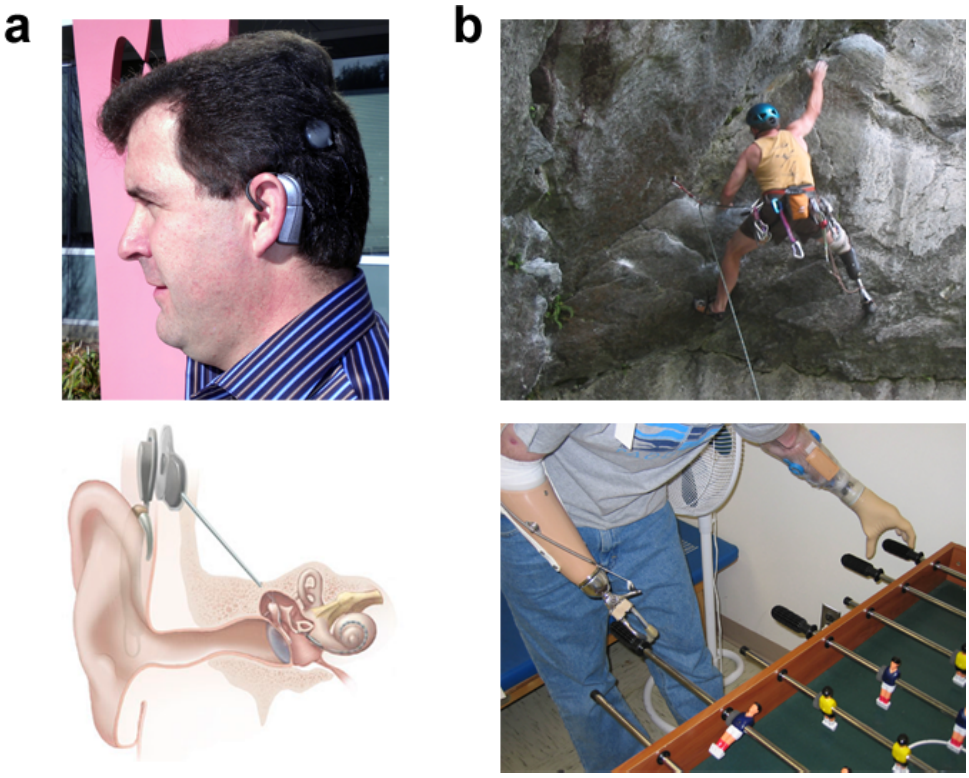

Figure 1.3: Examples of bioelectronic (prosthetic) devices interfacing directly with the human nervous system. **(a)** A cochlear implant is shown at left, and **(b)** examples of prosthetic limbs are shown at right. Reproduced by permission under the Creative Commons Attribution-Share Alike 3.0 Unported license.

ingly effective and functional devices to help treat patients, and perhaps, to one day augment our natural abilities. Indeed, the promise of interfacing our minds with computer systems in an efficient and useful way is a tantalizing possiblity.

The future for bioelectronics is bright, and we have only begun to scratch the surface in a field whose boundaries may only be limited by our imagination and willingness to explore what is possible. While it remains to be seen whether true brain-computer interfaces or functional cybernetic implants will become fact or remain as fiction, it seems certain that progress in these directions will provide an abundance of devices and technologies that will enable us to better

understand and treat diseases, and improve our capabilities and quality of life.

1.3 Organic Electronics

Materials naturally play a central role in the ongoing efforts to interface biology with electronics. There are many considerations to make when choosing what materials to employ, or envisioning what *new* materials might be needed for a given application. Bioelectronic devices must combine a mix of conductors, semiconductors, and insulators, that provide sufficiently high performance for the task at hand, but that also must be suitable for operation in the (often hostile) *in vivo* environment of the human body. On top of this, cost is an important factor to consider, as it must be for any technology geared toward real-world application.

Many of these considerations provide the impetus to consider the use of organic electronics for the active materials in bioelectronic devices. As (conducting) polymers, organic electronic materials offer many benefits over inorganic materials in the context of the biological environment, and also provide some capabilities that inorganics do not possess. Some of the most important benefits include: similar mechanical properties to those of tissue, the substantial availability of (bio-)chemical functionalization through various chemistries, their ease and low cost of processing, and their inherent compatibility with large-area and flexible substrates. The traditional drawbacks of organics, most notably their lower performance as compared to silicon-based electronics, are often not a concern due to the lower performance requirements inherent to bioelectronics applications.

In addition, conducting polymers are known to be ”smart materials” whose properties change upon electrochemical oxidation/reduction, a property that inorganic materials do not possess. This tunability of properties stems from the dual ionic and electronic conductivities of organics, which are coupled through the electronic doping/de-doping that occurs through the uptake or expulsion of ions. This process makes organics ideal electron-to-ion converters – a key property for communicating between the world of electronics, where information is transmitted via the electron, and the world of biology, where information is tramsitted via ions and larger molecules.

Many properties of an organic electronic material can be changed via the electrochemical doping/dedoping process, including: surface energy (and thus, hydrophilicity/hydrophobicity), local pH and chemistry, mechanical stiffness, surface roughness, and surface charge. These changes in properties enable organics to actively interact with living cells.

1.3.1 PEDOT:PSS and PEDOT:TOS

Poly(3,4-ethylenedioxythiophene) (PEDOT) is an intrinsically semiconducting, conjugated polythiophene, whose conductivity can be made semi-metallic with the inclusion of an ionic salt which dopes the polymer. The most popular dopant is poly(styrenesulfonate) (PSS), a polyanion which when added to PEDOT, forms PEDOT:PSS – a water-soluble, highly-conductive polymer (1000 S/cm) that is easily solution-processed into thin films with excellent transparency (Figure 1.4) . PEDOT:PSS films have traditionally been used in antistatic coatings, as well as more recently in a variety of electronic applications,

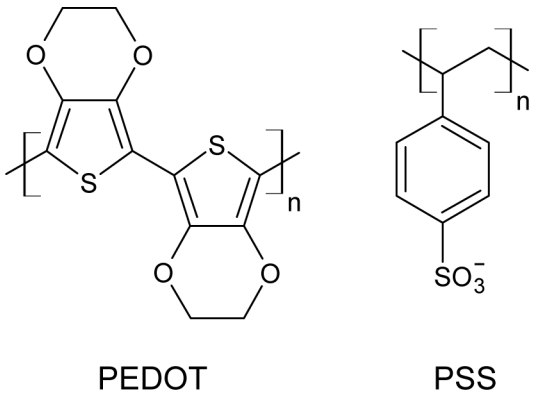

Figure 1.4: The chemical structure of poly(3,4-ethylenedioxythiophene) (PEDOT) and the anionic dopant poly(styrenesulfonate) (PSS), which comprise PEDOT:PSS.

including: as a hole-injection layer for optoelectronic devices [2], and as the active channel material in organic transistors [3, 4].

Although PEDOT:PSS is often described as a water-based solution, strictly speaking it is not soluble in water but instead forms a dispersion in water of small PEDOT:PSS gel particles [5]. In an untreated state, the outer surface of these particles is predominantly composed of the non-conductive PSS dopant chains, as PSS is truly soluble in water (unlike PEDOT). As a result, films formed from such a dispersion contain many PSS-rich domains which isolate the conductive PEDOT, and consequently limit the overall conductivity of the film [6]. This effect can be mitigated with the addition of a variety of conductivity enhancement agents – most popularly dimethylsulfoxide (DMSO) and ethylene glycol, but more generally including amides, sulfoxides, glycols, imides, surfactants, and salts. The inclusion of such addiditives can increase the conductivity of PEDOT:PSS films by several orders of magnitude [7, 8].

An alternative dopant is *p*-toluenesulfonate (tosylate, TOS), a small molecule

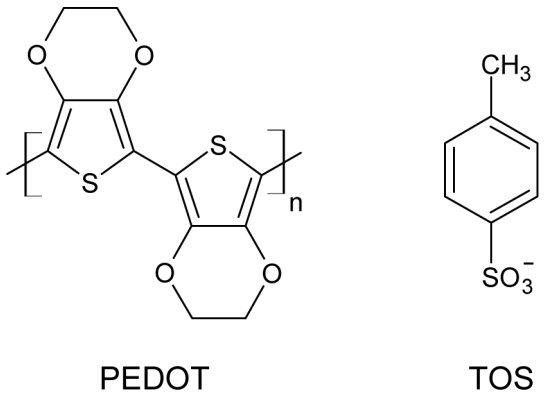

Figure 1.5: The chemical structure of poly(3,4-ethylenedioxythiophene) (PEDOT) and the anionic dopant *p*-toluenesulfonate (tosylate, TOS), which comprise PEDOT:TOS.

oxidant and anion, that both catalyzes the vapour-phase polymerization reaction of PEDOT, and acts as the electronic dopant in the resulting polymer (Figure 1.5). As compared to PEDOT:PSS films that do not include any additives, PEDOT:TOS films offer higher conductivities (100s of S/cm), better stability in aqueous environments, and the ability to conformally coat structures in a non-line-of-sight manner (due to the vapour-phase nature of the processing).

All of these factors made PEDOT:TOS a more attractive choice of material over PEDOT:PSS when this work first began (2007); however, recent advances in the additives and formulations of the more commercially-popular PEDOT:PSS have meant that at present (2012), PEDOT:PSS films now routinely offer higher conductivity and better water stability than their PEDOT:TOS counterparts. As a result, PEDOT:PSS would seem to be the logical material of choice for any future work that does not specifically require the benefits of vapour-phase processing over solution processing. (For additional notes on this discussion, see Section B.1).

1.3.2 PEDOT as an Electrochemically-Active Material

Like all conducting polymers, PEDOT has both electrical conductivity, as well as ionic conductivity. More importantly, these dual conductivities are coupled through the electrochemical doping/de-doping process that involves both types of charge carriers. This makes PEDOT an effective electron-to-ion converter; a key property that makes it an ideal candidate material to bridge the gap between the world of electronics, where the charge carrier is the electron, and the aqueous world of biology, where the charge carrier is the ion.

The coupling of an ionic flux into (or out of) the polymer to its electrical conductivity occurs due to a chemical doping/de-doping process similar in nature to how a dopant such as PSS or TOS increases the native conductivity of PEDOT. An anionic dopant such as these will partially (and locally) oxidize the PEDOT chain, introducing an electronic charge that self-localizes to form a polaron on the polymer backbone [9]. This polaron is free to move along the conjugated backbone, acting as an additional charge carrier in the material.

Energetically speaking, the introduction of such polaronic (or bi-polaronic) charge states introduces mid-bandgap energy states, which at heavier doping levels broaden into bipolaron bands within the bandgap [10]. These serve to effectively reduce the bandgap of the organic semiconductor, giving it semi-metallic conductivity.

Mechanistically, electrochemical *oxidation* (applying a positive bias to the polymer relative to an aqueous electrolyte) *increases* the electrical conductivity, while electrochemical *reduction* (applying a negative bias to the polymer relative to an aqueous electrolyte) *decreases* the electrical conductivity.

In addition to electrical conductivity, many other properties of PEDOT change under the influence of electrochemical oxidation/reduction.

1.3.3 Tunable Material Properties

Conducting polymers are known to be "smart" materials whose properties can change under electrochemical oxidation/reduction. Some of the these properties include: electrical conductivity, surface energy (hydrophobicity/hydrophilicity), colour/optical density (photochromism), mechanical stiffness, volume (swelling) surface charge, and pH; many of which could likely affect the adsorption (and steady-state molecular conformation) of proteins, and subsequently the eventual behaviour of living cells.

For PEDOT:PSS and PEDOT:TOS in particular, electrochemical oxidation (reduction) leads to an increase (decrease) in conductivity, a decrease (increase) in surface pH, and an increase in hydrophilicity (hydrophobicity) [Figure 1.6]. Additionally, colour/optical density changes due to the photochromic nature of the film, with the oxidized film appearing nearly transparent and the reduced film appearing clear, but with a darker blue/purple hue.

Meanwhile, mechanical stiffness in particular does not change appreciably under electrochemical oxidation/reduction, as measured by liquid-immersion atomic force microscopy (AFM) in our experimental system [11]. This is particularly important for cell studies, as it ensures that conformation is altered *in isolation* of stiffness, which has known effects on cell behaviour (adhesion, motility, etc.).

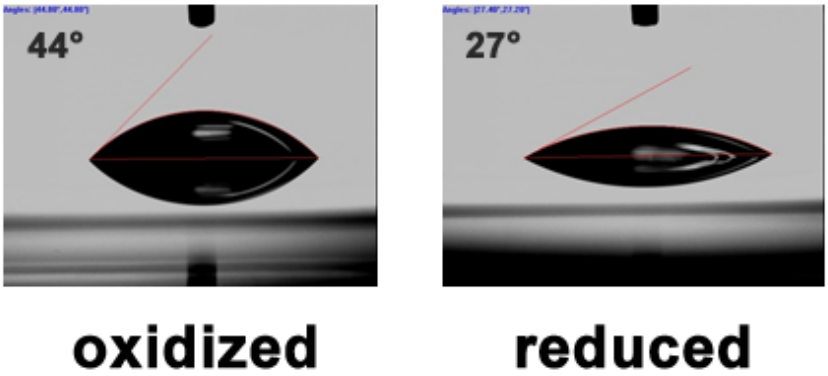

Figure 1.6: Water contact angle measurements on oxidized and reduced PEDOT:PSS surfaces, demonstrating tunability of surface energy/hydrophilicity.

Additionally, the microscopic structure (of PEDOT:TOS) does not change substantially with redox state, as shown by *in situ* grazing incidence x-ray diffraction [12]. While the crystallinity of the films does change slightly with redox state, the positions of the alternating PEDOT and TOS layers in the thin film do not change, indicating that the small tosylate counteranions in PEDOT are not mobile, and therefore do not leach from the film under an applied bias. This is particularly important as some anionic dopants used in PEDOT formulations show cytotoxicity (i.e., dodecylbenzenesulfonic acid, DBSA, the monomer of PSS) [13].

1.4 Biological Systems and Models

1.4.1 The *In Vivo* Environment

With an eye toward developing devices that may eventually operate within an *in vivo* environment, it is worth mentioning the conditions such a device will encounter. The relatively warm (37 °C), aqueous (conducting) environment of the body is not particularly hospitable to electronics, and materials must be chosen accordingly. At a minimum, the *in vitro* laboratory environment requires materials that are stable in water for long periods of time (up to weeks, preferrably longer, if any type of long-term cell study is desired), and certainly in all cases, materials must not be cytotoxic. Devices designed for use *in vivo* will face additional challenges, most notably the foreign-body/inflammatory immune response of the host organism, which may coat the device with scar tissue, effectively separating it (electronically) from the target tissue or analyte. Here, an anti-fouling strategy may need to be considered, in an attempt to mask the device from detection.

The *in vivo* environment itself is complex, being composed of different types of tissues, which are themselves composed of both cells, and the extracellular matrix (Figure 1.7). Of particular (but sometimes overlooked) importance is the fact that the *in vivo* environment is three-dimensional (whereas, in contrast, the vast majority of *in vitro* laboratory work is two-dimensional). Landmark studies have shown that cells often behave very differently in 3D environments as compared to 2D environments, in many contexts including enhanced biological activities, narrowed integrin usage, and the composition and function of matrix adhesions. [14]. This is an important consideration with regard to the assumed

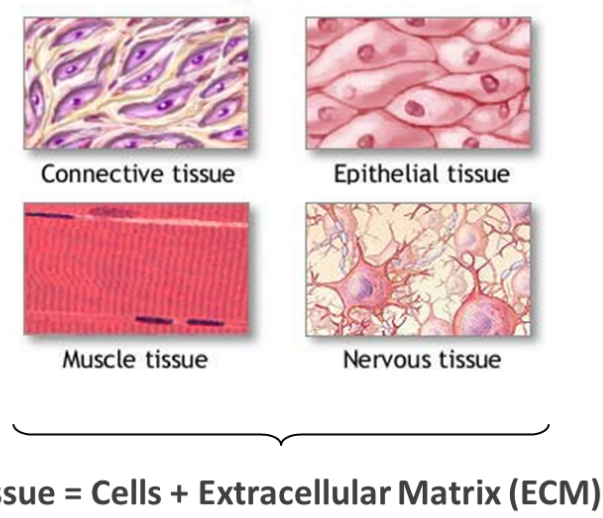

Figure 1.7: The four main tissue types in the human body. Each tissue is comprised of unique cell types, as well as proteins, proteoglycans, and other molecules that form the extracellular matrix. Adapted with permission from the National Institutes of Health.

physiological relevance of any findings stemming from 2D cell-culture experiments, and points to the need for improved 3D cell-culture systems.

1.4.2 The Extracellular Matrix

The extracellular matrix (ECM) forms the microenvironment for cells *in vivo*, and is comprised of proteins (such as collagen, fibronectin, laminin, etc.), proteoglycans, polysaccharides, and other molecules. The ECM provides mechanical support/anchorage for cells, enables migration, and plays a role in controlling cellular signalling, both by directly binding cell receptors, and by releasing soluble factors. Cell-ECM interactions are vital to an incredibly wide range of processes in healthy and diseased tissues, including growth/development,

wound healing, and metastasis in the context of cancer.

1.4.3 Proteins at the Cell-Surface Interface

Proteins in the ECM play a prominent role in guiding biological signalling and function, and it is their (often variable) conformation that governs their multiple biological functions. Proteins are involved in a multitude of signalling pathways, both inter- and intra-cellular, and also mediate many other interactions that cells have with their environment. In particular, cells adhere to their local environment by binding to adhesion proteins that are presented on nearby surfaces; this is true both *in vivo*, where cells bind to extracellular matrix proteins such as fibronectin (Fn), collagen, vitronectin, etc., as well as *in vitro*, where many of these same proteins must be coated or adsorbed onto surfaces of interest. Without the presence of these proteins, cells have no mechanism by which they can adhere to external surfaces.

1.4.4 Fibronectin

Fibronectin (Fn) is a prominent extracellular matrix glycoprotein that plays important roles in mediating cell adhesion [15], migration [16], differentiation [17], and growth [18], during processes such as embryonic development and tissue remodelling. It is a dimeric molecule with a relatively high molecular weight of 440 kDa, and can exist both as a soluble protein, as well as an insoluble component of Fn fibers that are prevalent in the extracellular matrix. Fn plays important roles in adhesion and signalling events, and binds to cells via membrane-

spanning receptors called integrins. Fn also binds to other extracellular matrix components such as collagen, fibrin, etc., and plays an important in processes such as collagen fibrillogenesis.

Fn is the most abundant adhesion protein present in the serum (Fetal Bovine Serum, FBS) added to cell culture media, and additionally has previously been studied and developed for conformation-dependent imaging techniques [19]. For these reasons, Fn was selected as the candidate adhesion protein for further study.

1.4.5 Structure and Conformations

Fibronectin is a 440 kDa protein dimer [20] composed of two similar or identical monomer subunits of molecular weight 220(20) kDa each, covalently linked together by disulfide bonds at their carboxy-terimini [21]. Each monomer is composed of three types of repeating subunits (named type I, II, and III) [20], as shown in Figure 1.8.

Of particular interest are the III_9 and III_{10} modules, which play important roles in cell integrin binding (see Section 1.4.7).

Like virtually all large protein molecules, fibronectin exists in a non-equilibrium state, and can vary substantially in shape (and therefore effective size), depending on its local environment. The molecular conformation of Fn can vary reversibly between the extremes of a compact state (globular, as in solution), to a state of partial unfolding, where subunits can become (reversibly) unfolded. It is this unfolding of the protein's tertiary structure that lends Fn

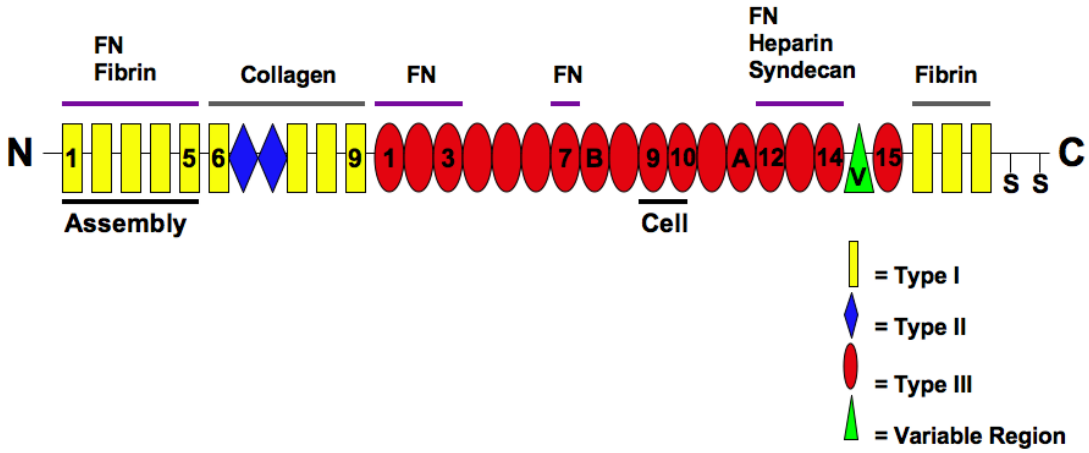

Figure 1.8: The modular structure of a single Fn monomer, composed of type I, II, and III repeating subunits. Of particular interest are the III_9 and III_{10} domains, which play important roles in binding cell integrins. Reproduced by permission under the Creative Commons Attribution-Share Alike 3.0 Unported license.

its tremendous extensibility, allowing Fn fibers to be reversibly strained by as much as 700% [22].

Electron microscopy studies have shown the contour length of the most extended Fn dimers to be 160 nm, with an average strand diameter of 2 nm [23]. Conversely, Fn can exist in a compact globular form in solution, with a variable Stokes (hydrodynamic) radius R_H ranging from 9.6 nm to 14.5 nm, depending on the ionic strength of the solvent [24].

1.4.6 Conformation-Dependent Cell Adhesion

As described in Section 1.4.5, fibronectin can exist in a variety of conformations, and changes in conformation can result in altered cell adhesion characteristics. In particular, changes to the arginine-glycine-aspartic acid (RGD) cell-binding peptide loop on the III_{10} module of the fibronectin molecule have important

implications for adhesion.

The RGD loop plays an important role in binding many cell-surface integrins, including the $\alpha_5\beta_1$ and $\alpha_v\beta_3$ integrins [15] (see Section 1.4.7 for details). The III_{10} module containing the RGD loop is one of the least mechanically-stable modules of fibronectin and is easily disrupted by strain. Even small strains (insufficient to cause unfolding) can change the angle of the RGD loop enough, relative to the neighbouring synergy site on the III_9 module, to inhibit $\alpha_5\beta_1$ binding in a conformation-dependent way [25].

1.4.7 Integrin Binding Model for Cell-Fn Adhesion

Cell-fibronectin adhesion in the work presented here is largely mediated by two important cell-surface integrins (receptors), named the $\alpha_5\beta_1$ and $\alpha_v\beta_3$ integrins. The $\alpha_v\beta_3$ integrin (historically known as the vitronectin receptor [26]), binds to the RGD loop found on the III_{10} module of fibronectin. Meanwhile, the $\alpha_5\beta_1$ integrin simultaneously binds both the III_{10} RGD loop and the synergy site found on the neighbouring III_9 module, requiring both to be in close spatial proximity. Hence, $\alpha_5\beta_1$ binds to fibronectin in a conformation-dependent manner, with binding activity suppressed in extended and unfolded conformations where the III_9 and III_{10} modules are separated [27].

1.4.8 Model Cell Lines Used for Cell Culture Studies

3T3-L1s as a Model for Fibroblasts/Stromal Cells

Fibroblasts are well-known for their role in producing and organizing the extracellular matrix, both in healthy and diseased (cancerous) tissues [28, 29]. To this end, a well-characterized murine preadipocyte cell line (3T3-L1) [30] was used for the majority of studies, and was chosen as being representative of fibroblast/stromal cells. Choosing this cell line that is well-studied and widely-used in the tissue engineering field enables the use of established protocols and comparisons to be made of observed cell behaviour with those in the literature.

MDA-MB231s as a Model for Tumour Cells

The MDA-MB231 cell line is a highly invasive metastatic breast cancer cell line, and was chosen as a representative model for diseased (cancerous) tissues.

1.5 Optical Microscopy Characterization Methods

1.5.1 FRET-labelled Fibronectin to Assess Conformation

In order to study the conformation of proteins in our system, a technique is clearly needed which is able to assess conformational changes. We utilized an optical techinque – Förster Resonance Energy Transfer (FRET) – compatible with cell culture, our polymer devices, and standard confocal light microscopy. By labelling fibronectin molecules with chromophores that have appropriate

emission-excitation spectral overlaps, the fibronectin molecules became optically active in a conformation-dependent manner, thus enabling us to directly probe the conformation of adsorbed fibronectin in our system.

This section describes the FRET phenomenon, how it is employed with chromophore-labelled fibronectin molecules, and how measurements are performed to assess conformation.

1.5.2 Förster Resonance Energy Transfer (FRET)

Förster Resonance Energy Transfer (FRET) is a non-radiative transfer of energy from one or more "donor" chromophores to one or more "acceptor" chromophores via a dipole-dipole coupling interaction. The process was first described by Theodor Förster in 1948 [31]. Efficient energy transfer is dependent on: 1) the spatial separation of the two chromophores; 2) the spectral overlap of the donor emission spectrum with the acceptor absorption spectrum; and 3) the relative orientation of the dipole moments of the donor and acceptor chromophores.

The FRET efficiency E can be thought of as the quantum efficiency of the energy transfer process; i.e., the number of transfer events that occur per donor excitation event. This can be written as

$$E = \frac{1}{1 + (r/R_0)^6} \tag{1.1}$$

where r is the donor-to-acceptor separation distance, and R_0 is the Förster radius for a given donor-acceptor pair (i.e., the separation at which the energy transfer efficiency in Eq. (1.1) is equal to 50%).

Of note is the very strong r^{-6} dependence, indicating that the energy transfer exhibits a strong sensitivity to the spatial separation of the fluorophores. Given that a typical value for R_0 is roughly 10 nm, the length-scale associated with FRET makes it candidate as a "molecular ruler" type of tool, able to provide information on distances at the molecular scale. For the particular FRET pair used in this work (Alexa Fluor 488 donor and Alexa Fluor 546 acceptor), the Förster radius is $R_0 = 6.4$ nm.

1.5.3 Fibronectin Labelling Scheme

A schematic of the Fibronectin labelling scheme is shown in Figure 1.9. The scheme utilizes four acceptor fluorophores per Fn dimer (two per monomer) attached to the cysteine residues of the III_7 and III_{15} modules, and ten donor fluorophores (five per monomer) randomly attached to lysine-containing modules. This scheme was optimized through prior work [19] to exhibit sensitivity over a maximum range of fibronectin strain (in contrast to a 2-donor, 2-acceptor scheme that is only sensitive to small strains). Depending on the molecular conformation of a labelled fibronectin molecule, the spatial overlap of the donor and acceptor fluorophores will increase (compact conformation) or decrease (extended to unfolded conformations). This can be assessed by measuring the emission spectra of the donor and acceptor fluorophores simultaneously, and calculating the FRET intensity ratio

$$I_r = \frac{I_{Acc}}{I_{Don}} \tag{1.2}$$

where I_{Acc} and I_{Don} are the emission intensities of the Acceptor and Donor fluorophores, respectively.

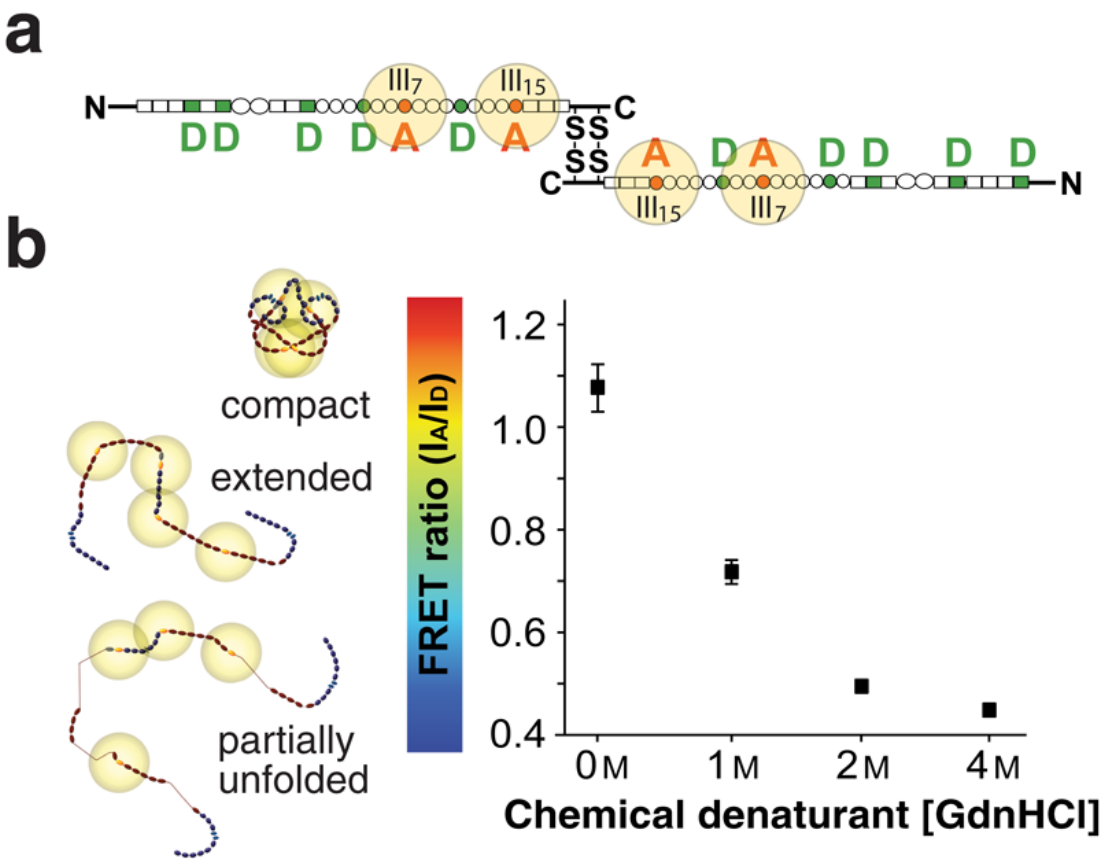

Figure 1.9: **(a)** Fluorophore labelling scheme for FRET-labelled fibronectin (Fn). A Fn dimer is shown with four acceptor fluorophores attached at the III_7 and III_{15} positions of each arm, and ten donor fluorophores attached at random positions. The yellow circles represent the Förster radii of the fluorophores (R_0 = 6.4 nm, omitted on donors for clarity). **(b)** Calibration curve of FRET ratio (i.e., acceptor intensity/donor intensity) and corresponding colour map as a function of chemical denaturant (guanidine hydrochloride) concentration. The schematics at left correlate FRET ratio (and colour map) to protein conformations obtained via circular dichroism measurements of free dilute molecules in solution. Reproduced with permission from Wan *et al.* (2012) [11].

In a compact conformation, large spatial overlap of the fluorophores leads to highly efficient energy transfer (Eq. (1.1)) from donor to acceptor. This results in (relatively) low intensity emission from the donor (green), and high intensity emission from the acceptor (red), resulting in a high FRET ratio.

Conversely, in a more extended conformation, decreasing spatial overlap leads to less efficient energy transfer. This results in higher intensity emission from the donor (green), and lower intensity emission from the acceptor (red), resulting in a lower FRET ratio. High sensitivity is also achieved at extended and unfolded conformations, because inter-monomer FRET is eliminated in extended conformations, followed by intra-monomer FRET being eliminated in unfolded conformations due to increasing spatial separation of fluorophores.

Importantly, < 10% of the total fibronectin used in any experiment is FRET-labelled (i.e., > 90% is unlabelled). This threshold was previously found to restrict FRET to intramolecular FRET, as opposed to *inter*molecular FRET due to a high fluorophore concentration, which would artifically raise the measured FRET value.

1.5.4 Confocal Microscope Measurements

FRET imaging can be performed on a (confocal) microscope with at least two separate emission detectors, allowing simultaneous measurement of the donor and acceptor emission spectra. Confocal microscopy enables imaging in a thin plane of focus (achieved via "point"-illumination and reduction of defocused light with a spatial pinhole) [32], allowing "z-stacks" of images to be acquired through the height of a sample (i.e., imaging slices of a 10 µm-thick layer of

protein laid down by cells).

Measurements were performed on a Zeiss LSM 710 Laser Scanning confocal microscope in the Cornell Life Sciences Core imaging facility. The microscope features two photomultiplier tube detectors (PMTs) with tunable wavelength detection ranges, allowing for simultaneous imaging of the donor and acceptor fluorophores.

The detection ranges of interest were 514 nm to 526 nm for the donor and 566 nm to 578 nm for the acceptor, corresponding to the emission maxima of the Alexa Fluor 488 and 546 fluorophores, respectively.

1.5.5 Spatial Resolution

Since imaging is performed with an optical microscope, the spatial resolution of this technique is at best diffraction-limited [33]. In an optical microscope, light of wavelength λ, travelling in a medium with refractive index n and converging to a spot with angle θ, will focus to a spot of radius

$$d = \frac{\lambda}{2\,(n \sin\theta)} \tag{1.3}$$

also known as the Abbe diffraction limit [34]. The term $(n \sin\theta)$ is the numerical aperture (NA) of the optical system, which can reach about 1.4 with modern optics. Thus, the Abbe limit is roughly $d \approx \lambda/2$ to $\lambda/3$, limiting spatial resolution to no better than ~200 nm.

This implies that the FRET-labelling strategy employed here cannot provide information about the conformation of individual Fn molecules. Rather, the ensemble average FRET ratio from many molecules in a small volume (or within

a fibronectin fiber) provides statistical information about the local conformation of Fn molecules. This is not a problem for the task at hand, as we are interested in average conformational changes over larger scales than individual molecules.

CHAPTER 2

ELECTRICAL CONTROL OF CELL ADHESION ON CONDUCTING POLYMER SURFACES

2.1 Contributors

This project was the initial collaboration between the former Malliaras group and the Fischbach group. Daniel Brooks (former lab manager in the Fischbach group) was instrumental in teaching and helping me with the cell-culture and imaging techniques that were required for this work. Claudia Fischbach provided invaluable guidance from the biomedical perspective at this early stage in the collaboration. George Malliaras proposed the initial project idea and helped design the original device architecture, and contributed tremendously to the rapid preparation of the manuscript – our total time of one month from start to acceptance is surely some sort of record!

2.2 Abstract

We describe a conducting polymer device that can induce electrically-controlled density gradients of normal and cancerous cell lines, and hence can be used as a tool for the study of cell-cell interactions.

This work was published in *Chemical Communications* in 2009 [35]. All figures reproduced with permission.

2.3 Introduction

Gradients in cell density control the functions of normal and pathological tissues by regulating the quality and quantity of cell-cell interactions. For example, spatial variations in cell density lead to the generation of growth factor gradients, which, in turn, influence cell migration, proliferation, and differentiation [36, 37]. Additionally, gradients in cell density can impact the number of physical connections a cell is able to form with neighbouring cells, which modulate intracellular signalling pathways and affect cell behaviour [38]. Perturbation of cell interactions in normal tissues (e.g., due to injury) typically triggers a cascade of events that re-establishes tissue homeostasis. However, in pathological tissues (e.g., tumours) these control mechanisms are dysfunctional and can lead to impaired tissue functions and patient prognosis [39]. The ability to establish controllable cell density gradients is critical to gaining a better understanding of the underlying cellular and molecular mechanisms.

A variety of techniques can be used to generate spatially controlled variations in cell density. For example, artificial, growth factor-sequestering extracellular matrices allow to probe the synergy between interstitial fluid flow and growth factor signalling on the formation of endothelial cell gradients [40]. Additionally, microfluidic devices capable of generating morphogen gradients provide useful tools to establish local variations in cell density as a result of directed cell migration [41]. These systems permit to establish gradients in cell density as a function of varying mechanical and chemical cues, but whether electrical stimuli may be used in a similar manner has not been investigated.

In 1994, Wong, Langer and Ingber discovered that aortic endothelial cells

grow differently on oxidized and on reduced polypyrrole films [42]. Since conducting polymers such as polypyrrole can be reversibly switched between oxidized and reduced states, these experiments pave the way for non-invasive control of cell growth. Subsequent work focused predominantly on neurons, where the stimulation of neurite outgrowth is important for, among other things, repair of spinal cord injury [43]. The topic of cell growth on conducting polymer surfaces is currently receiving renewed attention due to the interest in organic electronics [9]. A recent example is the work by the Berggren group demonstrating differences in neural cell adhesion on reduced and on oxidised conducting polymer electrodes [44].

2.4 Results and Discussion

In this Communication we report a device in which an applied bias causes a redox gradient in a conducting polymer film, which, in turn, leads to the creation of density gradients in normal and cancerous cells. We chose two cell lines that are representative models of normal and cancerous cells for this demonstration: The 3T3-L1 (ATCC CL-173) cell line, which consists of mouse fibroblasts capable of transforming into adipocytes and is representative of normal mesenchymal cells, and the MDA-MB-231 (ATCC HTB-26) cell line, which is derived from human breast cancer and is representative of an aggressive and invasive form of the disease.

Figure 2.1 shows the device that was used to create the redox gradients. A 3 mm wide, 2.5 cm long indium tin oxide (ITO) stripe was deposited on a glass substrate, onto which a PDMS reservoir that contained the cell growth medium

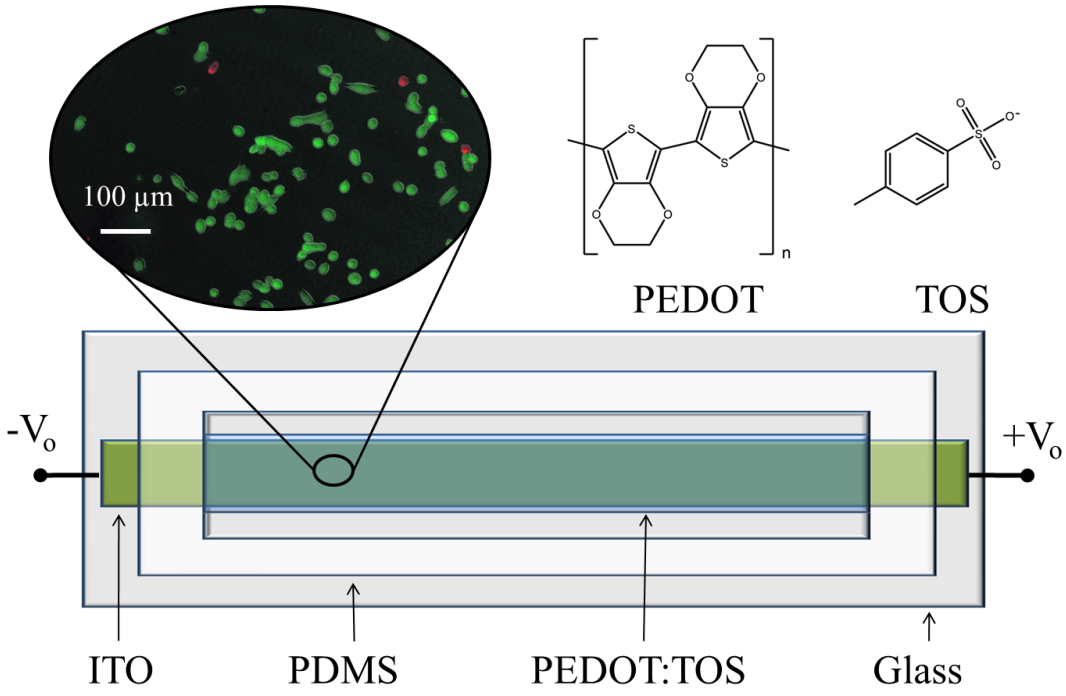

Figure 2.1: Device schematic and chemical structure of PEDOT:TOS. The inset shows a micrograph of MDA-MB-231 cells after performing a Live/Dead assay.

was attached. A ground electrode was immersed in the PDMS reservoir. A bipolar power supply sourced −1.5 V and +1.5 V at opposite ends of the ITO stripe (outside the PDMS reservoir), creating a linear potential gradient. A thin film of the conducting polymer poly(3,4-ethylenedioxythiophene) doped with *p*-toluenesulfonate (PEDOT:TOS) was deposited on top of the ITO stripe by vapour phase polymerization [45]. Its conductance was about 100 times lower than that of the underlying ITO stripe, and as a result it just replicated the local surface potential of the ITO. The linearity of the gradient was confirmed by measurements of surface potential, which was found to vary inside the PDMS reservoir between −1 and +1 V. Under this bias configuration, positive ions from the growth medium enter the PEDOT:TOS film near the negatively-biased end. The

local hole density decreases in order to maintain charge balance and the film is reduced. In a similar fashion, oxidation takes place near the positively-biased end, creating a redox gradient along the length of the PEDOT:TOS stripe. The redox gradient is accompanied by a characteristic colour change across the film [46]. It should be noted that without the underlying ITO stripe, the change of conductivity associated with ion uptake in the PEDOT:TOS films would result in highly non-linear potential gradients which might lead to ill-defined redox gradients.

Cell growth medium was added to the PDMS reservoir and the devices were biased for 1 hour to establish the redox gradient on the PEDOT:TOS. The bias was then removed and the cells were seeded. Hence, *cell growth took place in the absence of applied bias*. The colour change that accompanied the establishment of the redox gradient was immediately visible following the application of the bias and remained stable for the duration of the experiment, without noticeable change when the bias was removed. Cells were seeded on the device and allowed to grow for 24 hours before their viability was quantified with a Live/Dead assay, using Calcein AM (green, calcein acetoxymethyl ester; Invitrogen C1430) for live cells, and Propidium Iodide (red, Sigma-Aldrich P4170) for dead cells. Seeding densities were ~15 000 cells/cm^2 for the 3T3-L1 cells and ~30 000 cells/cm^2 for the MDA-MB-231 cells.

Figure 2.2 shows composite images mapping 3T3-L1 cell distributions along the PEDOT:TOS stripe in two devices that were biased in opposite directions from each other. Each composite consists of 6 individual fluorescence micrographs, obained through a 2.5× objective with a Zeiss Axio Observer.Z1 microscope. The images reveal regions of low cell density, where individual cells are

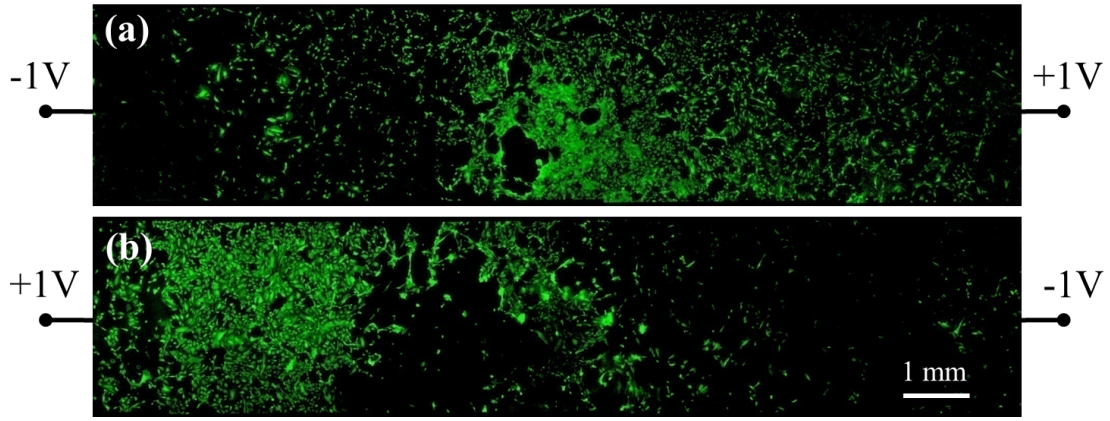

Figure 2.2: Fluorescence micrographs of calcein-green stained 3T3-L1 cells for two devices biased in opposite directions.

well separated from each other, as well as regions where the cells are beginning to form a confluent monolayer. From these plots it can be seen that large density gradients can indeed be established on the PEDOT:TOS surface. Moreover, in both plots, the regions of low density are close to the negatively-biased side of the PEDOT:TOS. Therefore, the direction of the cell density gradient is controlled by the direction of the applied bias.

Figure 2.3 shows population densities obtained from analysis of fluorescence images from both 3T3-L1 and MDA-MB-231 cells. The images were parsed in 20 segments along the length of the PEDOT:TOS stripe and the number of individual cells was counted using ImageJ (National Institutes of Health). The average cell density, obtained from analysis of data from two devices was then plotted as a function of the average local potential that was applied on each segment before seeding the cells. The experiment was repeated several times to ensure the reproducibility of these observations. The data shows that both types of cells prefer the oxidized side of the PEDOT:TOS film, and the cell density decreases gradually towards the reduced side of the film. It should be noted that quantifi-

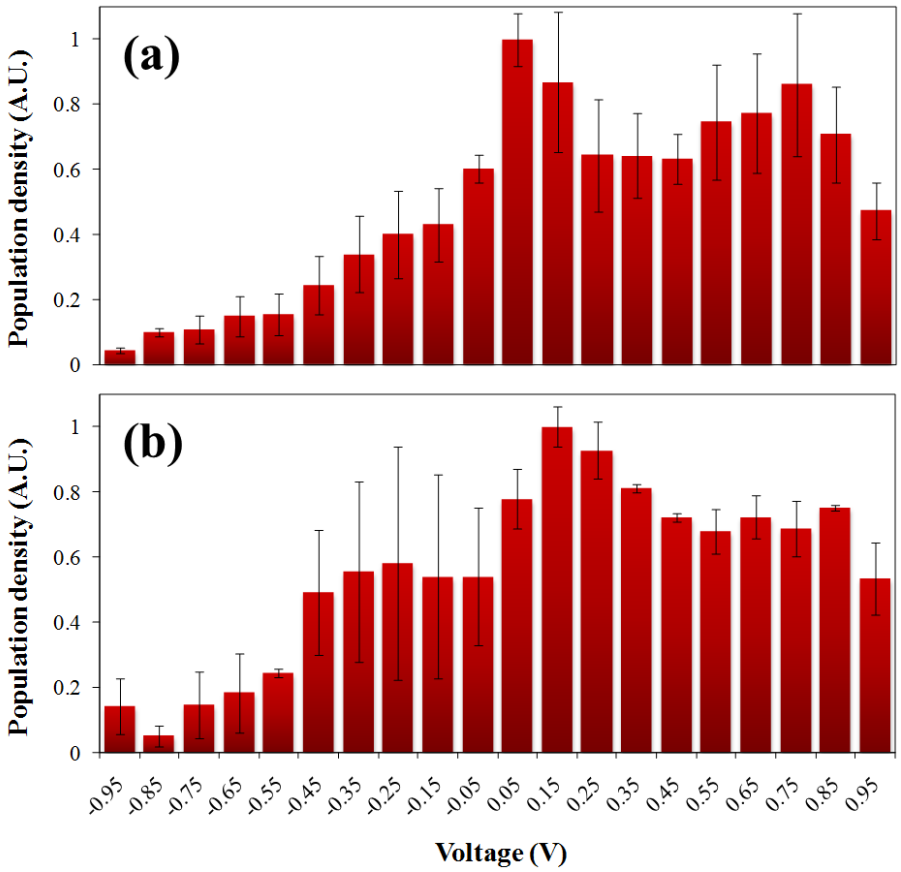

Figure 2.3: Population densities for 3T3-L1 cells **(a)** and MDA-MB-231 cells **(b)** across the PEDOT:TOS film.

cation of the total cell surface area at different locations of the established cell density gradient yielded similar results.

The observed density gradients are not caused by a change in the viability of the cells along the PEDOT:TOS film. The inset of Figure 2.1 shows a typical micrograph (phase-contrast, green and red fluorescence at 10×) of the MDA-MB-231 cells from a reduced region of PEDOT:TOS after performing the Live/Dead assay. In this image green fluorescence corresponds to live and the red to dead cells, indicating that the majority of the cells are alive. Cell viability was found to exceed 98 ± 1% regardless of the redox state of the PEDOT:TOS film. The 3T3-

L1 cells also showed similarly high viability on all regions of the PEDOT:TOS film. Cells grown on a control device that was never biased also showed the same viability. It should be noted though that if the applied bias is not removed prior to seeding the cells, their viability and morphology are quickly and adversely affected. In an experiment where the bias was maintained during cell culture, changes in cell morphology were detectable less than 30 minutes after seeding. After less than 2.5 hours of culture, nearly all adhered cells on the device had lost viability, as confirmed with a Live/Dead assay. It is likely that the observed cell density gradients arise due to differences in cell adhesion. The latter is mediated in part by the adsorption of adhesion proteins (e.g. fibronectin) that are contained in the serum of the growth medium. An immunostaining assay was performed to quantify fibronectin (FN) adsorption on different locations of the device. Devices were incubated under bias for 1 hour in a FN solution diluted in DI water. The concentration of FN corresponded to an area density of 15 micro g/cm^2 for each device.

The FN was fixed with neutral-buffered formalin for 30 minutes and the devices were washed twice in phosphate buffered saline (PBS) with 0.5% bovine serum albumin (BSA) to prevent non-specific binding of the primary antibody. The devices were then incubated for 1 hour in a 1:400 dilution of the anti-fibronectin primary antibody in PBS/BSA. The devices were washed twice with PBS/BSA and incubated for 1 hour in the dark in a 1:100 dilution of a fluorescent goat anti-rabbit secondary antibody in PBS/BSA. Subsequent washing and imaging of the fluorescence from the secondary antibody revealed the relative concentration of adsorbed fibronectin. The data were corrected for the dependence of the optical density of PEDOT:TOS on its redox state and are shown in Figure 2.4. The control corresponds to a device that was never biased. The

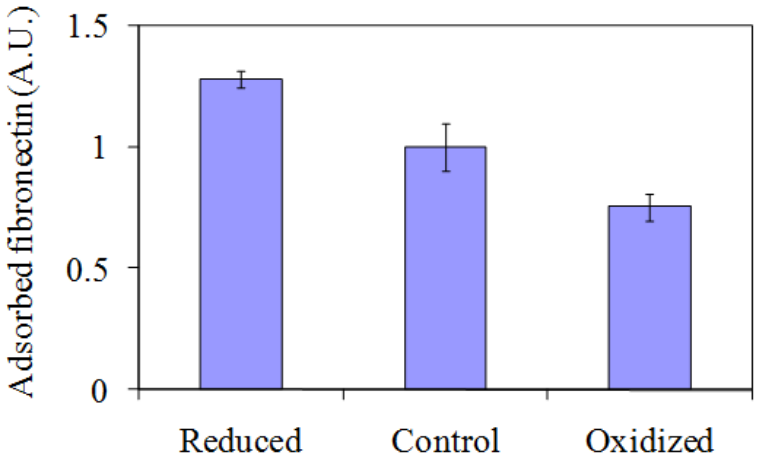

Figure 2.4: Quantification of adsorbed fibronectin as a function of the redox state of PEDOT:TOS.

data show that a redox gradient across a PEDOT:TOS film causes a gradient in adsorbed fibronectin concentration, with concentration decreasing from the reduced towards the oxidized side.

The higher concentration of adsorbed fibronectin on the reduced side of the device would imply better cell adhesion, leading to a higher cell density [47], which is the opposite of what we find here. The reason for the higher cell density on the oxidized side of PEDOT:TOS is currently not understood. A similar finding was recently reported by the Berggren group [44]. In a study of adhesion of c17.2 neural stem cells on reduced and oxidized conducting polymer electrodes, they showed a higher density of attached cells on the oxidized electrode. Moreover, they also showed that human serum albumin adsorbs preferentially to the reduced electrode. It was hypothesized that the orientation of adsorbed protein at the two electrodes might be different, or that the higher protein concentration on the reduced electrode might have a blocking effect on extracellular matrix proteins and hinder cell adhesion [44]. Understanding the

physics of protein adsorption on conducting polymer surfaces will be a major step towards uncovering the pathways leading to non-invasive, electrical control of cell adhesion. The device described here can create cell density gradients that range from isolated, well-spaced cells to confluent monolayers, and these are suitable for the study of cell-cell interactions. Compared to other techniques that can yield similar cell density gradients, it offers the advantages of simplicity and electrical control: There is no need for precise patterning of chemical cues on a surface the redox gradient is established automatically and its direction can be controlled by the applied bias. The spatial extent of the gradient (here, ~1 cm long) can be controlled by the dimensions of the conducting polymer film, or the applied bias. Moreover, the device described here offers open access to the cells an advantage over microfluidic techniques. Yet, conducting polymer devices similar to the one reported here have been integrated with microfluidic channels [48]. Therefore, electrical control of cell density gradients can also be obtained in a microfluidic format for systems-on-a-chip applications.

2.5 Conclusions and Perspectives

We described a simple device that can be used to establish redox gradients on a conducting polymer film. When cells are cultured on this film, density gradients are established. This was demonstrated for both normal and cancerous cells. A variation in the density of adsorbed fibronectin implies that the device works by controlling cell adhesion.

CHAPTER 3

ELECTRICAL CONTROL OF CELL MOTILITY USING A CONDUCTING POLYMER DEVICE

3.1 Contributors

This project was a collaboration between the former Malliaras group and the Reinhart-King group in Biomedical Engineering. The work was completed in parallel with the Cell Adhesion project described in Chapter 2, utilizing the same device architecture. The majority of the experimental work was carried out by Abdurrahman Gumus (a former graduate student in the Malliaras group), and Joseph Califano (a former graduate student in the Reinhart-King group).

3.2 Abstract

Control of cell migration is receiving a great deal of attention due to its relevance to the engineering of tissues. Here we report a device that consists of a conducting polymer stripe and achieves a continuum of microenvironments for cell growth under the influence of an applied bias. Marked differences are observed in the migration behaviour of bovine aortic endothelial cells (ECs) as a function of location along the polymer stripe, and a 3-fold variation is achieved in EC migration speed and directional persistence time. Moreover, the device induces directional cell migration along the conducting polymer stripe. A gradient in adsorbed fibronectin indicates that a spatial variation in cell adhesion

This work was published in *Soft Matter* in 2010 [49]. All figures reproduced with permission.

is at play. The ability to control cell migration behaviour using external electrical stimuli highlights the potential of using conducting polymers as "active" substrates for the non-invasive control of cell behaviour.

3.3 Introduction

Cell motility (movement) is not surprisingly related to adhesion characteristics. In particular, the speed of migration is dependent on adhesion strength. DiMilla and coworkers showed that cell speed exhibits a maximum at a certain level of cell-substratum adhesiveness [50]. This maximum occurs between the two extremes of excessively low adhesiveness that prevents cells from exerting adequate contractile forces to move, and excessively high adhesiveness that prevents cells from releasing their trailing edges during migration (Figure 3.1).

The directed assembly of cells into tissues is critical to embryonic development, wound healing and the engineering of tissues for organ regeneration and replacement [51]. Cell migration, which facilitates proper spatial localization during tissue formation, is largely controlled by the chemical and structural cues in the microenvironment that are integrated by the molecular machinery of cells. As a result, the engineering of well-defined extracellular matrix environments that control cell migration by altering the chemical, mechanical or structural properties of the extracellular scaffold [52] is receiving a great deal of attention.

Tissue engineering largely focuses on developing materials that induce physiological cell migration and tissue assembly by incorporating the extracellular cues found in vivo. It is well-established that soluble and insoluble chem-

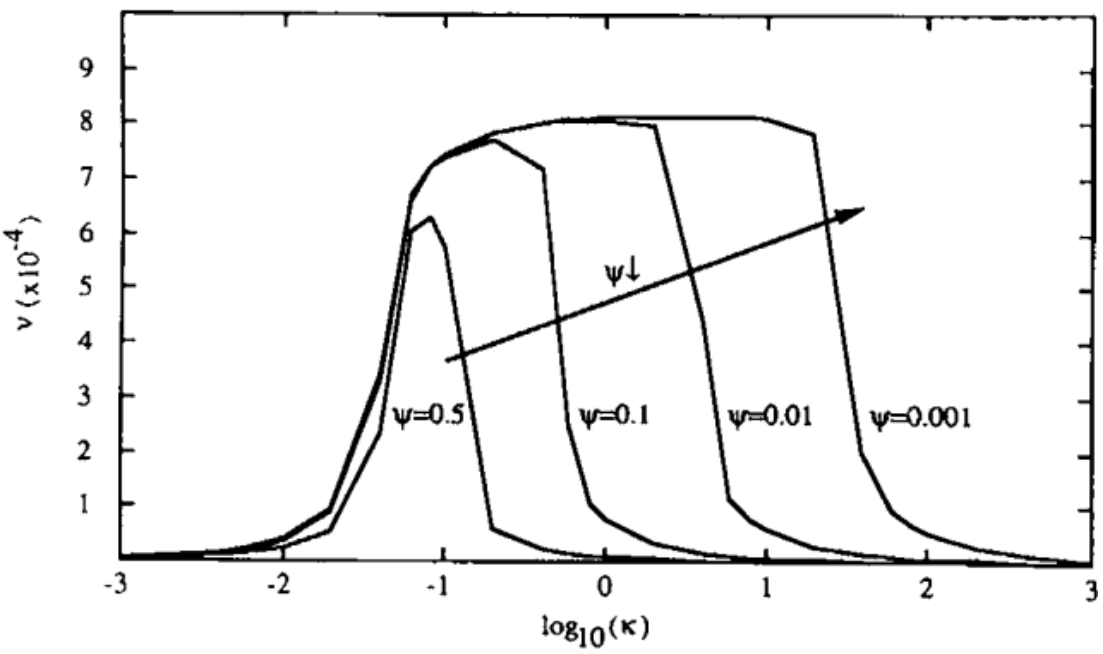

Figure 3.1: A biphasic relationship between dimensionless cell-substratum adhesiveness κ and dimensionless cell speed v can arise when bond distribution asymmetry results from a spatial variation in strength of adhesion-receptor ligand binding. Ψ is the ratio of uropodal to lamellipodal adhesiveness. Values of Ψ near unity correspond to small differences in bond affinity between front and rear of the cell, and the cell moves at nontrivial speeds over a restricted range of adhesiveness. Decreasing Ψ leads to the generation of greater adhesion-bond asymmetry, and cell movement can occur over a larger range of adhesiveness. Reproduced with permission from DiMilla *et al.* [50].

ical gradients [53, 54], gradients in mechanical stiffness [55, 56] and micro- and nano-topographical features [57] can be exploited to direct and/or enhance cell migration. It is known that cells can respond to chemical gradients of growth factors through chemotaxis and haptotaxis, and gradients in mechanical stiffness through durotaxis. As such, many biomaterials and devices have been engineered by using novel polymers, chemical conjugation techniques or microfluidics to present well-defined chemical or mechanical gradients to cells

The goal of these platforms has been to induce cell migration as a critical step in forming replacement tissues. Many of the current strategies have limitations. In the case of chemotaxis-based approaches, it has been difficult to achieve long-term, stable gradients to induce cell migration on an implantable device. In durotaxis, most materials that have been developed to incorporate tunable, well-defined mechanical gradients are not biocompatible and would not be suitable for implantation. Therefore, there is a clear need to develop better strategies to reliably and easily control cell migration using a method amenable to implantation.

The emergence of organic electronics – a technology that relies on carbon-based semiconductors to deliver devices with unique properties [9] – creates tremendous opportunities at the interface between electronic materials and living cells [58]: The soft nature of organics offers better mechanical compatibility with tissue than traditional electronic materials, while their natural compatibility with mechanically flexible substrates suits the non-planar forms often required for biomedical implants [59]. Their ability to conduct both ionic and electronic charges opens up a new communication channel with electrically active cells [60, 61]. Finally, the fact that the electronic properties of organics can be switched on or off in response to electrical stimuli [62] creates opportunities to use these materials as active substrates for cell growth.

In 1994, Wong *et al.* discovered that ECs grow differently on oxidized versus reduced polypyrrole films [42]. Since conducting polymers such as polypyrrole can be reversibly switched between oxidized and reduced states, these experiments paved the way for non-invasive control of cell behaviour by electrical means. More recently, devices based on a conducting polythiophene have been

used to demonstrate electrical control of cell adhesion [44], and the creation of density gradients in normal and cancerous cell lines [35].

3.4 Results and Discussion

In this chapter we demonstrate that organic electronic devices enable the electrical control of cell migration, hence they can serve as vehicles to help understand and engineer tissue formation. A device that allows one to create a continuum of microenvironments for cell growth is shown in Figure 3.2. An indium tin oxide (ITO) stripe was deposited on a glass substrate, onto which a polydimethylsiloxane (PDMS) reservoir containing cell growth medium was attached. A ground electrode was immersed in the PDMS reservoir.

A bipolar power supply sourced −1.5 V and +1.5 V at opposite ends of the ITO stripe (outside the PDMS reservoir), creating a linear potential gradient. A thin film PEDOT:TOS was deposited on top of the ITO stripe by vapor phase polymerization. Its conductance was about 100 times lower than that of the underlying ITO stripe, and as a result it replicated the local surface potential of the ITO. The linearity of the gradient was confirmed by measurements of surface potential, which was found to vary between −1 and +1 V inside the PDMS reservoir.

Under this bias configuration, positive ions from the growth medium enter the PEDOT:TOS film near the negatively-biased end. The local hole density decreases in order to maintain charge balance and the film is reduced. In a similar fashion, oxidation takes place near the positively-biased end, creating a redox gradient along the length of the PEDOT:TOS stripe. The redox gradient

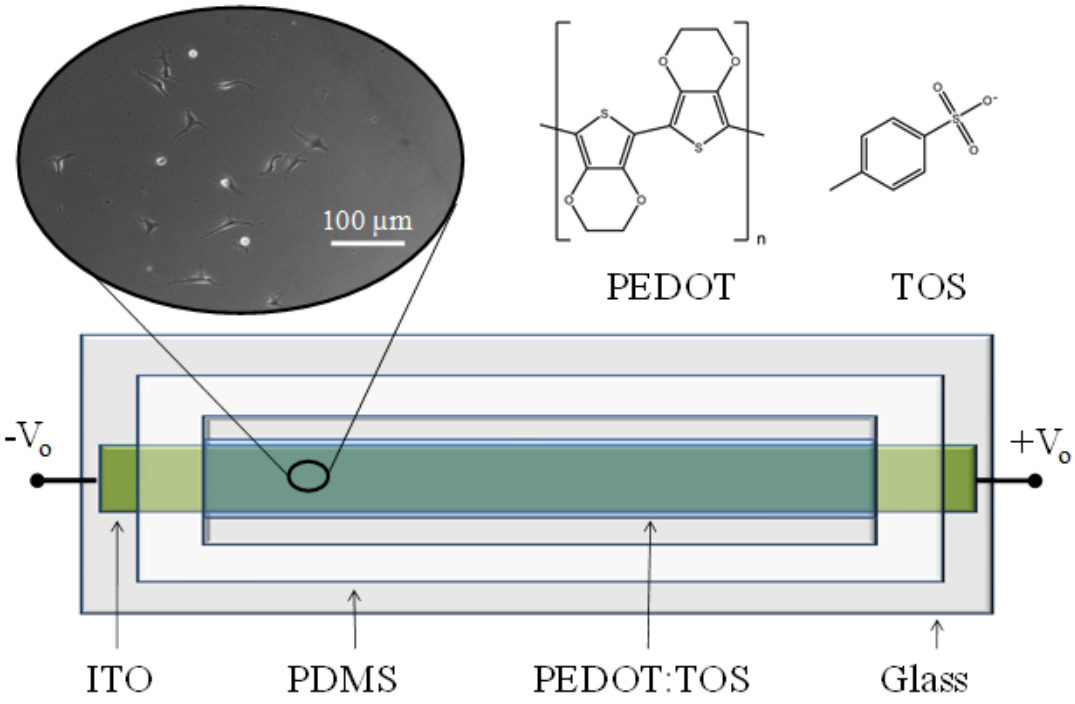

Figure 3.2: Device schematic and chemical structure of PEDOT:TOS. The inset shows a micrograph of endothelial cells adhered to the PEDOT:TOS surface.

is accompanied by a characteristic colour change across the film [46]. It should be noted that without the underlying ITO stripe, the change of conductivity associated with ion uptake in the PEDOT:TOS films would result in highly non-linear potential gradients which will fail to cause a well-defined continuum of microenvironments for cell growth.

Cell growth medium was added to the PDMS reservoir and the devices were biased for 1 hour to establish the redox gradient on the PEDOT:TOS. The bias was then removed and the cells were seeded. Hence, *cell migration was observed in the absence of applied bias*. The colour change that accompanied the establishment of the redox gradient was immediately visible following the application of the bias and remained stable for the duration of the experiment, without notice-

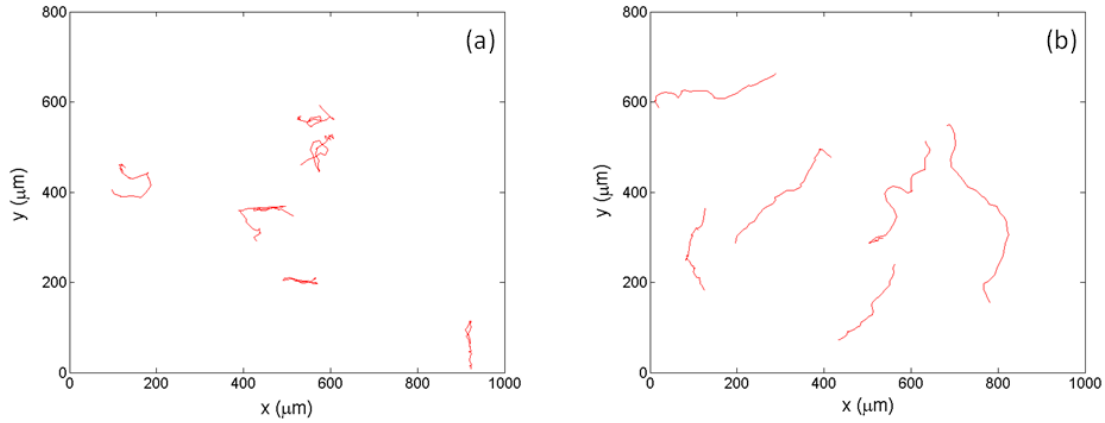

Figure 3.3: Trajectories of 6 ECs at a mildly reduced (**a**, V = −0.5 V) and at an oxidized (**b**, V = +0.9 V) location of the PEDOT:TOS stripe. The potential refers to the average local potential at a PEDOT:TOS pixel, as it was applied before seeding the cells.

able change when the bias was removed. The devices were placed on a Zeiss Axio Observer.Z1m inverted phase contrast microscope stage equipped with a chamber maintained at 37 degrees, 5% CO_2, and 40% humidity. Cells were plated at a density of 1500 cells/mL to minimize cell-cell collisions during migration and were allowed to adhere and spread for 6 hours prior to observation. Cell migration was measured using time lapse microscopy through a 10× lens, with images taken every 10 min for 6 hours. One such image is shown in the inset of Figure 3.2.

Images were acquired in five locations (pixels) across the PEDOT:TOS stripe that corresponded to an average local potential, as it was applied before seeding the cells, of −0.9 V (reduced), −0.5 V (mildly reduced), 0 V (reference PEDOT:TOS), 0.5 V (mildly oxidized), and 0.9 V (oxidized). Figure 3.3 shows the trajectories of six cells on the mildly reduced and oxidized pixels. Marked differences in the observed trajectories indicate that the redox state of the polymer significantly affects cell migration. Cells on the mildly reduced pixel seem to

only explore their immediate neighbourhood, as most of them remain within 100 µm from their origin during the 6 hour measurement period. On the other hand, cells on the oxidized pixel follow more open trajectories, moving as far as 400 µm away from their origin. It should be mentioned that in a control experiment, no spatial differences were observed on EC migration along a device that was not biased.

Cell trajectories were analyzed to extract mean-square displacement $\langle d^2 \rangle$ as a function of time t. Fitting to the persistent random walk equation [63]:

$$\langle d^2 \rangle = 2S^2 P \left[t - P\left(1 - e^{-(t/P)}\right) \right] \tag{3.1}$$

yielded the speed S, and the directional persistence time P of cells located in each pixel. Figure 3.4 shows the variation of S and P at the five pixels across the PEDOT:TOS. The speed for ECs on the reference pixel is 10.8 ± 1.7 µm/h, consistent with values measured for ECs on glass [37, 64]. While reduction of PEDOT:TOS does not have a significant effect on speed or persistence, oxidation does: The speed on the oxidized pixel increases to 32.53.8 µm/h, and a similar 3-fold increase is observed in the persistence. These results show that PEDOT:TOS can be used to electrically control cell migration behaviour. The 3-fold increase in speed achieved by oxidizing the PEDOT:TOS film compares well to improvements measured using fluid shear stress [64, 65] and chemical gradients [37] to induce migration. A larger change might be achievable using a higher applied bias, but electrolysis in the cell medium becomes an issue.

Cell migration involves the formation of new attachments at the front of the cell and the breaking of existing attachments at the rear. As a result, the maximum migration speed is predicted to occur at an intermediate value of

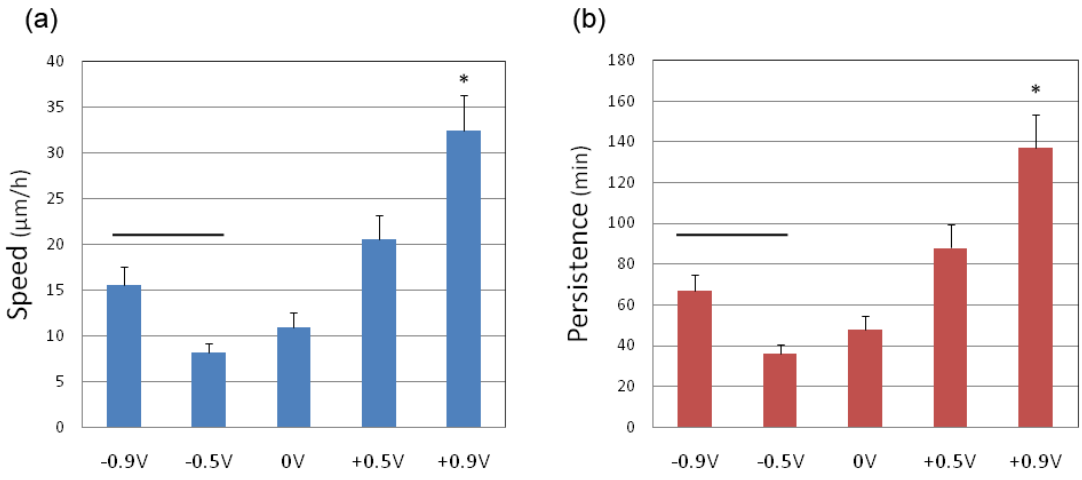

Figure 3.4: Migration speed and direction persistence time at various locations across the PEDOT:TOS stripe which are marked by the average local potential, as it was applied before seeding the ECs. * indicates $p < 0.0001$ compared to all other groups. Dash indicates statistically similar groups.

cell-substrate adhesiveness [50]. Increasing or decreasing adhesion beyond this optimum is therefore predicted to decrease cell migration speed. Cell adhesion is mediated in part by the adsorption of adhesion proteins (e.g. fibronectin) that are contained in the serum of the growth medium. We therefore conducted an immunostaining assay to quantify the density of adsorbed fibronectin (Fn) at different locations along the PEDOT:TOS stripe. The results, shown in Figure 3.5, reveal that the density of adsorbed Fn increases along the PEDOT:TOS stripe from the oxidized to the reduced end. The observed changes in cell speed along the PEDOT:TOS stripe can be understood by assuming strong EC adhesion on the reduced parts of the PEDOT:TOS stripe. In this limit, cells find it difficult to break existing attachments and their speed is low. The lower density of adsorbed Fn on the oxidized pixels would then decrease cell adhesion, thereby increasing cell speed. This interpretation is consistent with the observation of Palecek *et al.*, who have shown that increasing the density of adsorbed

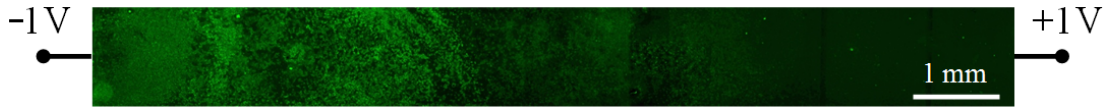

Figure 3.5: Fluorescence micrograph showing immunostained adsorbed fibronectin (green) along the PEDOT:TOS stripe. The direction of applied bias is indicated.

Fn above a certain value decreases cell speed [66].

An alternative interpretation is suggested by two recent studies of cell growth on conducting polymer surfaces [35, 44]. Both studies showed a higher density of attached cells on oxidized than on reduced PEDOT:TOS, suggesting stronger cell adhesion on the oxidized part of the film. However, human serum albumin and Fn were found to adsorb preferentially on reduced PEDOT:TOS. This was reconciled by hypothesizing that the orientation and conformation of the adsorbed protein at the two electrodes is different. According to these reports, the observed changes in speed along the PEDOT:TOS stripe can be understood by assuming that EC adhesion on the reduced parts of PEDOT:TOS stripe is below the optimum. In this limit, cells find it difficult to form new attachments and their speed is low. Stronger cell adhesion on the oxidized PEDOT:TOS pixels increases cell speed. At this point it is not possible to distinguish between these two interpretations and the only conclusion that can be drawn is that the redox gradient on the PEDOT:TOS establishes different microenvironments for cell growth. Understanding the physics of protein adsorption on conducting polymer surfaces will be a major step towards understanding the changes in migration behaviour observed here.

Adsorbed Fn density gradients, prepared using counter-propagating self-assembled monolayer techniques, are known to direct cell migration through

haptotaxis [37, 67]. Not surprisingly, directional cell migration was found to occur along the PEDOT:TOS stripe. Analysis of all cells trajectories on the reference pixel (which is located at the centre of the gradient) shows that there is net 7.7 µm migration (in 6 hours) from the reduced to the oxidized part of the PEDOT:TOS stripe. This displacement is similar in magnitude with values measured on static Fn gradients [37, 67]. However, the direction of cell migration in static gradients is from low to high Fn densities, opposite to what is observed here. This lends support to the hypothesis of stronger cell adhesion on the oxidized part of the film, as haptotaxis leads cells toward regions of higher adhesion [68].

3.5 Conclusions and Perspectives

Compared to other techniques that are used to control cell migration, the device discussed here offers the advantages of simplicity and electrical control, and might yield a useful tool for cell biology. Migration can be slowed down or accelerated, enabling the study of the signal transduction mechanisms governing cell speed, extension, sensing and directionality. Because these are the same cell behaviours critical to multiple biological processes, including cancer cell metastasis, inflammatory response, wound healing and embryonic development, implementing such a device could lead to the identification and study of molecular targets mediating these processes.

Multiple experiments could easily be assembled into one culture dish, enabling the study of multiple treatments and conditions simultaneously. Moreover, the device offers open access to the cells, an advantage over microfluidic

techniques. Yet, conducting polymer devices similar to the one reported here have been integrated with both traditional [3] and surface-directed [48] microfluidic channels. Therefore, electrical control of cell migration can also be obtained in a microfluidic format for systems-on-a-chip applications.

Directed migration can be induced without the need for precise patterning of chemical or mechanical cues on a surface – the redox gradient is established automatically and its magnitude, direction, and offset can be controlled by the applied bias. A smaller device, easily achievable with microfabrication, can support a steeper electrical gradient, creating an opportunity to control directional cell migration. PEDOT:TOS is biocompatible [58], and therefore can be incorporated into current biomaterial designs to enhance cell infiltration into tissue engineered constructs. As a wound healing dressing, for example, the use of PEDOT:TOS may decrease healing time by increasing directional cell migration into the wound. PEDOT:TOS redox gradients offer an easy-to-use, tunable platform which could be easily integrated into biomedical devices.

CHAPTER 4

ELECTRICAL CONTROL OF PROTEIN CONFORMATION

4.1 Contributors

This project was an extended collaborative effort between the (former) Malliaras, Ober, Fischbach, and Gourdon groups. Delphine Gourdon in particular provided tremendous (and timely) expertise regarding the terribly complicated realm of FRET measurements. Several times, her ability to see things in raw data that I had missed was critical in moving the project foward to (eventual) successful completion. Becky Schur (a former M.S. student in the Gourdon group) performed timely, reliable AFM measurements that made my life much easier. George Malliaras and Delphine Gourdon contributed tremendously to the preparation of the manuscript.

4.2 Abstract

We report conducting polymer devices that enable precise control of fibronectin conformation over macroscopic areas. Single conformations as well as conformation gradients are achieved by applying an appropriate potential. These surfaces remain biologically relevant and support cell culture; hence, they may serve as a model to understand and control cell-surface interactions, with applications in basic research, medical diagnostics, and tissue engineering.

This work was published in *Advanced Materials* in 2012 [11]. All figures reproduced with permission.

4.3 Introduction

Fibronectin (Fn) is a prominent extracellular matrix (ECM) glycoprotein that regulates cell adhesion [15], migration [16], differentiation [17], and growth [18], during processes such as embryonic development and tissue remodeling. Conformational changes of Fn are critically important in guiding these cell functions and have, for example, been linked to pathologies ranging from fibrosis to cancer [15, 69].

Here we report conducting polymer devices that enable precise control of protein conformation over macroscopic areas. Surfaces with single Fn conformations, as well as conformation gradients ranging from compact to unfolded, are achieved by applying the appropriate potential across the device. Importantly, the stiffness and topography of these surfaces remains unchanged, offering the potential to study protein conformation in isolation. These surfaces remain biologically relevant and support cell culture, therefore, they can enable a better understanding of the critical link between protein structure and function, with the ultimate goal of controlling cell-surface interactions. As such, they represent a new tool for biological research with many potential applications in basic research, medical diagnostics, and tissue engineering.

Proteins play a prominent role in guiding biological signaling and function, and it is their (often variable) conformation that governs their multiple biological functions. Previously, conformational changes in single molecules and macromolecular assemblies of proteins (including Fn) have been controlled and studied with techniques such as AFM [70, 71], MEMS actuators [22] and optical/magnetic tweezers [72, 73]. While these studies provide crucial insights into

protein structure and associated function, they are limited to controlling protein conformation over nanoscopic to microscopic areas, and mostly under non-physiological conditions, preventing their application in the presence of cells. Moreover, the microscopic and sophisticated nature of these experiments makes it very challenging to integrate them with common cell culture and biochemical analysis techniques that typically require the use of large populations of cells, and to readily apply them in conventional biological labs. Macroscopic surfaces with a precisely controlled protein conformation may be able to overcome these shortcomings and provide innovative tools for a broad range of physical and biological experiments.

Conducting polymers are known to be "smart materials" whose properties change upon oxidation/reduction, and this has spurred interest in their application at the interface with life sciences [58, 74]. In addition to having switchable properties, conducting polymer films are optically transparent, cytocompatible, and can be processed over large areas using low-cost fabrication techniques, rendering their integration with cell cultures facile. In one experiment, the redox state of polypyrrole was shown to affect cell adhesion [42], paving the way for smart Petri dishes that enable control of cell density on their surface. A recent study of cell viability and adhesion of epithelial cells on a conducting polythiophene suggested that changes in protein conformation underlie this effect [75], but no direct measurement of protein conformation was performed.

4.4 Results and Discussion

In this work we use Förster Resonance Energy Transfer (FRET) imaging [19] to directly assess Fn conformation on the surface of the cytocompatible conducting polymer [76] poly(3,4-ethylenedioxythiophene) doped with *p*-toluenesulfonate (PEDOT:TOS). We demonstrate two device configurations that achieve precise electrical control of protein conformation: One that establishes smooth gradients in Fn conformation, and another that establishes uniform Fn conformations over single, large area pixels. We used Fn molecules that were labeled for FRET and carried out a calibration measurement according to the scheme shown in Figure 1.9. We first measured FRET in solution as a function of increasing chemical denaturant concentration (guanidine hydrochloride, GdnHCl). The measurements were performed on a confocal microscope by simultaneously imaging both FRET fluorophores in separate channels, and calculating the FRET ratio as the acceptor fluorophore intensity (I_A) divided by the donor fluorophore intensity (I_D). We subsequently measured Fn conformation as a function of GdnHCl concentration via circular dichroism [19], and thus deduced a calibration curve of FRET ratio as a function of Fn conformation.

The device used to create gradients in Fn concentration consisted of a 2 cm-long, 0.7 cm-wide PEDOT:TOS film on top of an indium tin oxide (ITO) film of similar dimensions (Figure 4.1). A gradient in surface potential was established by applying ±1.0 V across this stripe while it was incubated for one hour in cell culture medium containing Fn. The underlying ITO film was used to ensure the linearity of the potential gradient, as conducting polymers are known to change their conductivity upon oxidation/reduction. This device configuration led to the establishment of a redox gradient along the PEDOT:TOS stripe, with the

most oxidized part close to the positive side of the device and the most reduced part close to the negative side. The incubation medium contained 30 µg/mL of Fn purified from human plasma, with less than 10% of the Fn labeled for FRET. This allowed us to assess protein conformation via analysis of intra- rather than intermolecular FRET [76]. We found that the applied bias established a monotonic gradient in FRET ratio, indicating a gradient in Fn conformations that varied smoothly from compact conformation at the oxidized end of the polymer stripe, to unfolded conformation at the reduced end of the polymer stripe (Figure 4.1a).

A second device configuration, consisting of two 1×0.7 cm^2 PEDOT:TOS pixels held at different potentials, was used to establish uniform Fn conformations. As in the previous device configuration, underlying ITO films were used to keep the potential of the pixels well-defined. In the example shown in Figure 4.1b, one of the pixels was brought to the most oxidized (+1 V) state, and the other to the most reduced (−1 V) state, while incubating in Fn-containing cell culture medium as before. Subsequent FRET imaging of the two pixels showed a uniform high FRET ratio (compact conformation) on the oxidized pixel and low FRET ratio (unfolded conformation) on the reduced pixel, respectively.

In order to assess the biological activity of the prepared Fn surfaces, we cultured mouse fibroblasts (3T3-L1) on both the oxidized and reduced pixels. Specifically, we seeded the cells on the different surfaces, and then quantified differences in cell adhesion by counting the number of adhered cells and assessing cell morphology 3 hours later. While overall morphology (spreading area, cytoskeletal arrangement) was not significantly different, the number of adhered cells was different on the two pixels, with 60% more cells adhering to

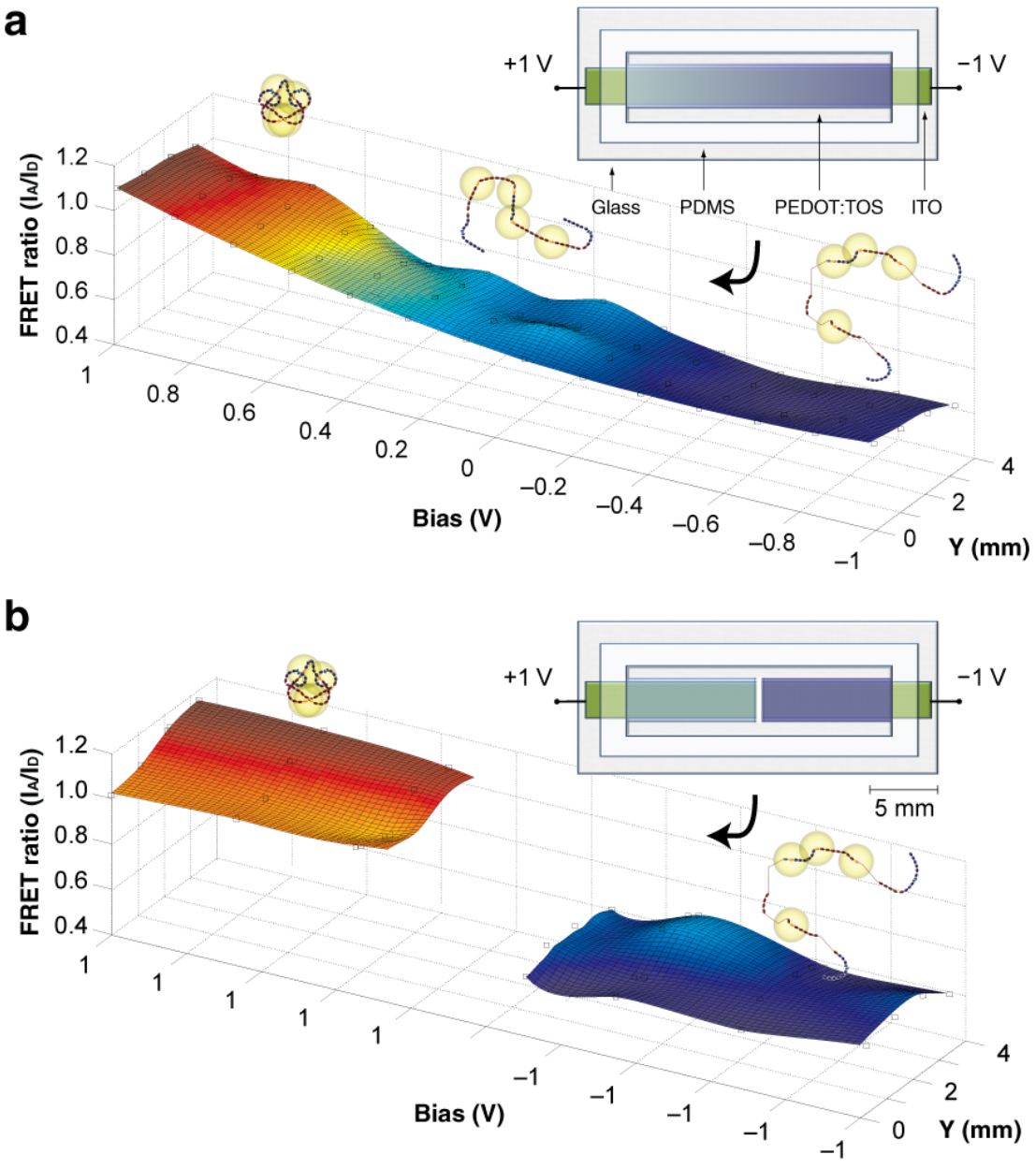

Figure 4.1: FRET ratios on the gradient **(a)** and pixel **(b)** devices as a function of applied bias and position. Images were taken at the locations indicated by open black squares, and the surface was interpolated. Colour of the surface indicates local Fn conformation as described in Figure 1.9b, and corresponding schematics of conformation are shown above the surface. The inset shows the device configuration.

the oxidized than to the reduced one. We hypothesized that the difference in cell adhesion was mediated by $\alpha_5\beta_1$ integrins – one of the major membrane receptors responsible for cell adhesion to Fn [77] – and that the ability of these integrins to bind to the oxidized vs. reduced pixels was altered due to conformational changes of adsorbed Fn. $\alpha_5\beta_1$ recognizes the synergy and arginine-glycine-aspartic acid (RGD) sites in the III_{9-10} modules of Fn [78, 79], and its binding affinity to Fn could be altered by Fn unfolding as this would change the spatial separation of the RGD and synergy sites. We tested this hypothesis by introducing a β_1 function-blocking antibody to inhibit $\alpha_5\beta_1$ binding, and observed that the differences in number of cells adhering to the oxidized and reduced pixels vanished (Figure 4.2). This response additionally indicated that the adsorbed Fn retained its biological activity and one of its primary functions; i.e., to support $\alpha_5\beta_1$ integrin binding.

Changes in Fn conformation, as well as changes in the redox state of a conducting polymer, may both be associated with modified mechanical [22] and/or topographical properties. Therefore, we used AFM to assess the elasticity (under compression) and surface roughness of the Fn-coated polymer pixels under different redox states. AFM measurements on the oxidized and reduced pixels (with adsorbed Fn), in buffer, yielded identical average Youngs modulus (90 kPa) and root-mean-square roughness (7 nm) for both.

We observed that the pH of the αMEM solutions (initially at physiological pH 7.4) attained pH values of 7.1 and 7.7 above the oxidized and reduced pixels, respectively. The observed changes of protein conformation may be related to local changes in pH near the surface of the conducting polymer. Changes in pH are known to affect protein conformation; in particular, Fn achieves more

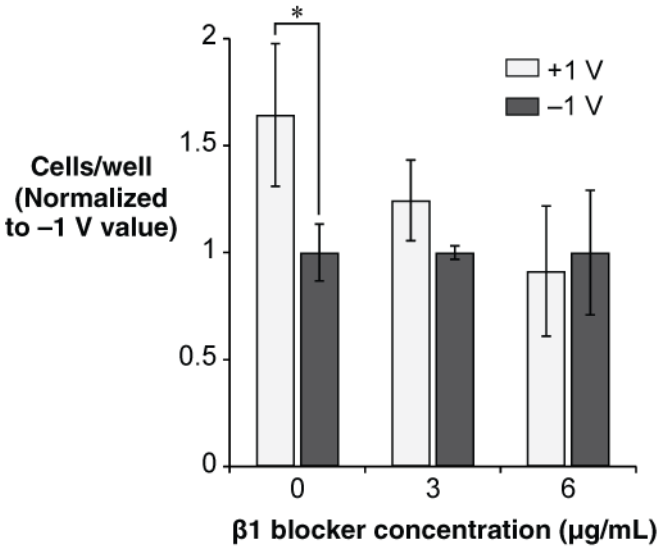

Figure 4.2: Relative number of adhered 3T3-L1 mouse fibroblasts on fully oxidized (+1 V) and reduced (−1 V) pixels, for varying doses of a β_1 function-blocking antibody. Cell numbers were recorded after 3 hours of incubation and are normalized to the values on the reduced pixels. ($^*P < 0.01$, unpaired t-test).

extended or unfolded conformations at higher pH levels [80]. This is in agreement with our findings that a lower pH over the oxidized pixel corresponds to a compact conformation of Fn, and a higher pH over the reduced pixel corresponds to an unfolded conformation of Fn. It should be noted that a lowering of pH over the oxidized pixel is consistent with expulsion of protons from the PEDOT:TOS film into the electrolyte, which is more negative. Similarly, protons in the neighbourhood of the reduced pixel will be driven into the PEDOT:TOS film, decreasing proton density in the electrolyte over the pixel and increasing the local pH.

Our experiments show that the conformation of adsorbed Fn can be varied continuously from compact, to extended, to unfolded by means of applying a linear potential gradient to a conducting polymer stripe. The FRET gradient

shown in Figure 4.1a provides, in essence, a calibration curve that maps the various conformations to a corresponding potential applied to the conducting polymer. Accordingly, one can select a desired protein conformation, and uniformly establish that conformation across a macroscopic surface by applying the corresponding potential on a conducting polymer pixel. In the particular setup described above, the size of the conducting polymer pixels was much larger than the size of individual cells and is therefore suitable for experiments with cell cultures. Pixels can, however, be made with dimensions on a cellular, or even on a sub-cellular level, providing a vehicle to study the influence of protein conformation on cell behaviour and signalling across multiple scales. Additionally, both stiffness and topography remain unaltered upon voltage application, showing that our technique allows control over protein conformation in isolation, and, therefore, enables studies of cell behaviour exclusively as a function of this variable.

The difference in cell adhesion between the compact and unfolded Fn pixels is consistent with a well-established integrin binding model. In particular, cell adhesion to Fn is largely mediated by $\alpha_5\beta_1$ integrins, which bind simultaneously the arginine-glycine-aspartic acid (RGD) sequence and synergy site of Fn, located on the neighbouring III_{10} and III_9 domains of Fn, respectively [78, 79]. These two peptide sequences must be in close proximity to enable $\alpha_5\beta_1$ binding, which only occurs when Fn is in a compact conformation [25, 81, 82]. In the extended to unfolded conformations, increasing spatial separation of the RGD and synergy sites would progressively inhibit $\alpha_5\beta_1$ binding, and thus weaken adhesion. Introducing the β_1 function-blocking antibody served to inhibit this conformation-dependent adhesion mechanism, resulting in similar numbers of cells adhering to both pixels.

4.5 Conclusions and Perspectives

In conclusion, we have demonstrated electrical control of protein conformation over macroscopic areas. Gradients as well as uniform conformations of adsorbed Fn can be established and are compatible with cell culture experiments. Moreover, conformation is controlled independently of other relevant parameters such as stiffness and surface roughness, which remain constant. As such, these surfaces constitute a model to understand and control cell-surface interactions. They will allow, for example, to study the effects of Fn conformational changes on cell function (i.e., adhesion, proliferation), and to tune the latter by dialling in a specific conformation. Moreover, as conducting polymers can be processed into many forms, including 3D architectures (e.g. hydrogels [83], electrospun networks [84], etc.), this method may pave the way toward physiologically-relevant 3D platforms with precise control over adsorbed protein conformation, with applications in tissue engineering and regenerative medicine.

4.6 Supporting Information

FRET Measurements: Lambda scans (495 nm to 580 nm) were performed under excitation from a 488 nm laser on devices in the gradient configuration, both with and without FRET-labelled Fn. The devices without Fn served as controls to measure background autofluorescence from the underlying PEDOT:TOS and ITO layers. A typical resulting lambda scan is shown in Figure 4.3a, and the resulting FRET ratios are shown in Figure 4.3b. FRET ratios are calculated from the lambda scan spectra by integrating the emission over the regions of interest

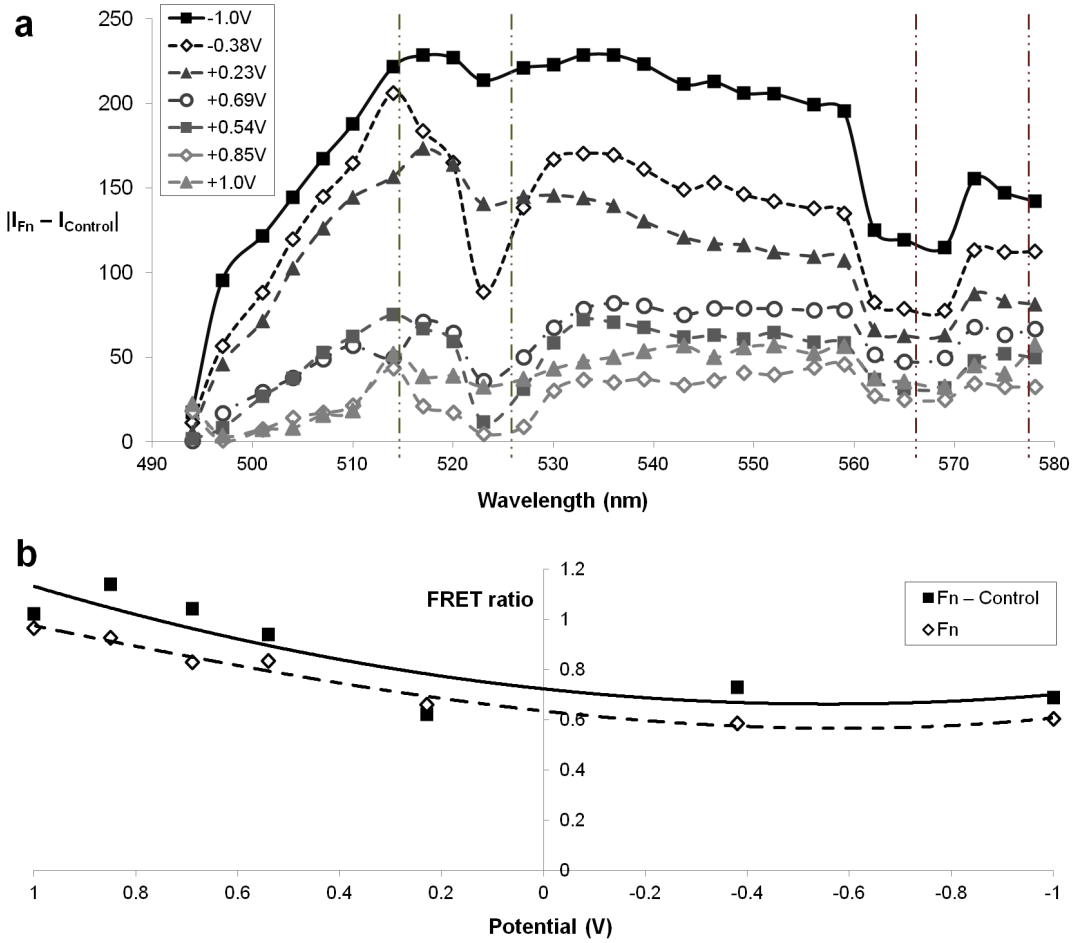

Figure 4.3: **(a)** Lambda scan of fluorophores emission intensity (after background subtraction) recorded as a function of potential on a gradient device, with adsorbed FRET-labelled Fn. The vertical dashed lines indicate the regions of interest for the donor (514 – 526 nm) and acceptor (566 – 578 nm) fluorophores, respectively. **(b)** FRET ratio ($I_{Acceptor}/I_{Donor}$) calculated from the integrated emission of the lambda scan, in the appropriate regions of interest.

for the donor (514 – 526 nm) and acceptor (566 – 578 nm) fluorophores, respectively.

CHAPTER 5

CONDUCTING POLYMER SURFACES ALTER PROGENITOR CELL ADHESION AND SECRETION

5.1 Contributors

This project was a strong collaborative effort with Emily Brooks in the Fischbach group. Emily and I contributed roughly equally to the experimental work, an are co-first-authors on the manuscript. I fabricated all of the PEDOT:PSS devices, and performed all of the seeding experiments with Emily. Emily (along with Maya Madhavan, an undergraduate in the Fischbach group) performed all of the ELISA assays. Maya was instrumental in helping me finish the project after Emily's graduation and departure in July 2012. Maya continued to run ELISAs and also collected the data and images for the cell-derived matrices and the HUVEC migration assays.

Claudia Fischbach provided invaluable guidance throughout this project, helping to guide the experimental designs and develop/prepare the manuscript. The device architecture used in this work was a modification I made on the design developed with George Malliaras. Chris Ober provided general support and guidance.

This work is being submitted as an invited article to *Biochimica et Biophysica Acta – General Subjects*. All figures reproduced with permission.

5.2 Abstract

We report conducting polymer devices that alter the adhesion and secretion characteristics of progenitor cells by controlling the conformation of surface-adsorbed fibronectin and serum proteins. By using these devices to alter conformation in isolation (i.e., without changing matrix stiffness, composition, or quantity), changes in protein conformation are shown to be responsible for the upregulation of pro-angiogenic secretions from fibroblasts in the tumour environment.

5.3 Introduction

The portion of tissues external to a cell, or the extracellular compartment, is comprised of a matrix providing support and structure to the cellular component of tissue. This extracellular matrix (ECM) is composed of fibrous proteins, proteoglycans, and adhesive glycoproteins, as well as signalling molecules including cytokines and growth factors [85]. By binding to, rearranging, and applying force to the ECM, cells are able to utilize the ECM as a signalling depository. The main structural proteins within the ECM include collagen, fibronectin (Fn), elastin, and laminin, to which cells are able to bind at specific adhesion sites [85]. The abundance of each specific protein type varies throughout the diverse tissues of the body (i.e., Fn is a major component of connective tissues and is also found in the blood plasma [86]). Additionally, Fn is one of the two major adhesive proteins in serum, making it one of the most widely utilized adhesive proteins in cell culture [87].

In addition to the broad role Fn plays in the ECM, it is particularly known to undergo changes within the tumour ECM [88]. During a process termed desmoplasia, ECM synthesis in the tumour is enhanced, which leads to the deposition of a thick protein matrix dense with Fn. This amplification of the Fn content in the tumour as compared to normal epithelial ECM promotes tumour progression [89], metastasis [88], as well as chemotherapeutic resistance [90]. Fibroblasts within the tumour microenvironment are largely responsible for these changes to the tumour ECM [28]. In fact, Chandler *et al.* previously showed that tumour-derived soluble factors cause fibroblasts to produce an ECM containing Fn in a more extended conformation [69]. These changes in the tumour ECM prompt questions regarding the role of this ECM protein in tumourigenesis.

The abundance of Fn in the ECM and in serum leads to its ubiquitous use in cell culture, and thus a thorough understanding of how Fn signals various cellular functions is necessary. This large dimeric glycoprotein contains three types of repeating modules which contain cell adhesion sites, such as the arginine-glycine-aspartic acid (RGD) site as well as protein binding sites [91]. Cell adhesion to Fn is largely mediated by the $\alpha_5\beta_1$ integrin through the combination of the RGD and synergy sequence sites [91]. While cells are able to actively reorganize Fn in their ECM, this exceptionally extensible protein can undergo conformational changes that expose cryptic binding sites [22]. The conformation of Fn can vary throughout the ECM and it is not fully understood how these changes may alter cell behaviours. Fn can cause changes in the cell behaviour not only because of altered cell binding as the protein conformation changes but also due to changes in stiffness as changes in conformation also lead to altered protein stiffness [22]. Various means including hydrogel artificial ECMs have been implemented to investigate the role of stiffness in altering key cel-

lular functions including proliferation [92, 93], differentiation [94], malignancy [95], and angiogenesis [96]; however, the ability to independently investigate the role of protein conformation on these behaviours have been limited.

Many tumourigenesis-promoting processes are likely altered by changes in Fn; in particular, one such process of paramount importance is the in-growth of vasculature, as tissue survival and growth requires the ability to receive nutrients and oxygen while disposing of unwanted cellular waste. tumours achieve this through a process termed angiogenesis, which is reliant on a variety of pro-angiogenic growth factors including vascular endothelial growth factor (VEGF) [97]. As its name implies, VEGF directly impacts the function of endothelial cells by promoting their ability to form the vasculature that enables tumourigenesis. Here we present our investigation of the effect of altered tumour ECM structure on the pro-angiogenic potential of tumour stromal cells. To this end, we cultured fibroblasts in matrices derived from normal and tumour stromal cells and quantified their pro-angiogenic potential by measuring VEGF secretion levels.

As changes to the ECM occur at sites of disease, means to decipher how these changes contribute to disease progression are necessary. Diseased ECMs often contain proteins in altered composition and conformation which can lead to changes in both protein stiffness as well as overall tissue stiffness (Figure 5.1). To decipher the role of ECM protein conformation independent of these other ECM alterations on cell function, we utilized a conducting polymer device that we previously showed could establish precisely-controlled protein conformations over large areas [11]. Here, we take the next step by culturing cells on these devices, allowing us to assess the isolated impact of ECM protein conformation on the pro-angiogenic potential of tumour stromal cells. These findings stress

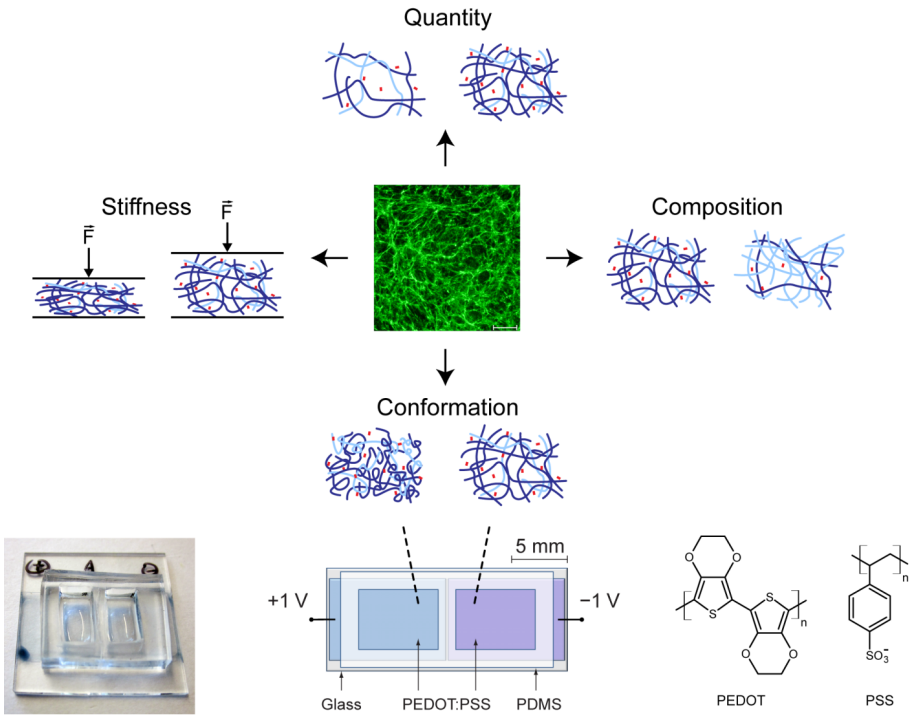

Figure 5.1: Changes to the extracellular matrix (for example, in the tumour microenvironment) lead to simultaneous changes in many matrix properties, such as quantity, stiffness, composition, and conformation. Traditional experiments using cell-derived matrices are unable to isolate one experimental parameter, such as conformation. By using a PEDOT:PSS conducting polymer device (bottom), protein conformation can be controlled in isolation, enabling studies of the role of altered conformation in altered cell behaviour.

the importance not only of ECM content but also protein conformation.

5.4 Results and Discussion

5.4.1 Tumour Stromal Cell-Derived Matrices Enhance Stromal Cell Pro-Angiogenic Behaviours

Tumour-mimicking ECMs were produced by culturing 3T3-L1 cells for 3 days in TCM or control media which as previously reported [69] produces matrices with varying quantities of extracellular Fn (Figure 5.2A). These tumour and control cell-derived matrices were then isolated from the cells through a cell extraction process, maintaining the differential Fn (Figure 5.2B). Using these methods, the propagation of signals within the tumour matrix due to stromal cell alterations to the matrix were measured. To assess changes in cell response to the varying matrices, normal 3T3-L1 cells were reseeded onto the cell-derived matrices and their pro-angiogenic capacity was quantified after 24 hours. Fibroblasts seeded onto tumour rather than control fibroblast-derived matrices produce more VEGF, as measured via ELISA (Figure 5.2C).

5.4.2 Assessment of Altered Stromal Cell Secretions on Endothelial Cell Angiogenic Functions

We next investigated the response of endothelial cells to the altered pro-angiogenic potential of stromal cells cultured on compact vs. unfolded ECM protein conformation. We collected media after 24 hours from the 3T3-L1s that were reseeded onto the cell-derived tumour and control matrices, and assessed pro-angiogenic potential via a transwell migration assay with human umbilical

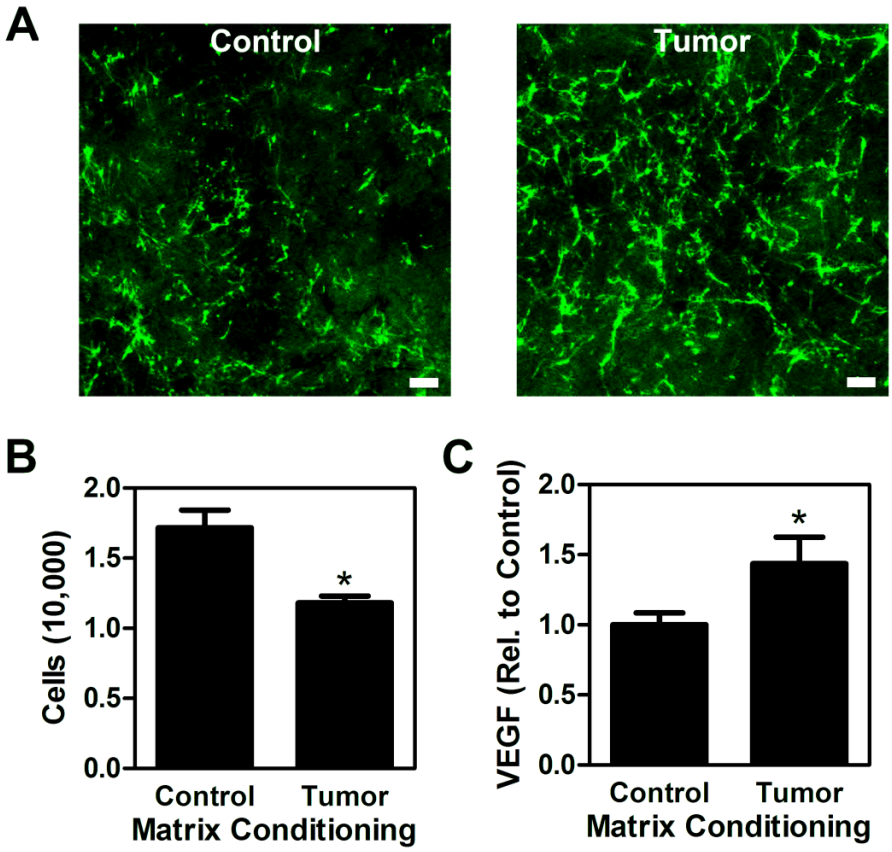

Figure 5.2: 3T3-L1 cells produce a matrix of varied Fn content when cultured in the presence of TCM [30]. The 3T3-L1 cells were then extracted from these matrices leaving a cell-derived matrix containing enhanced levels of Fn in the tumour condition (**A**, scale bar = 10 µm). When 3T3-L1 cells were subsequently cultured on these matrices, more cells adhered to control as compared to tumour-derived matrices (**B**). VEGF content in the media from normal 3T3-L1 cells seeded onto these matrices was greater for those cells on tumour as compared to control 3T3-L1-derived matrices (**C**).

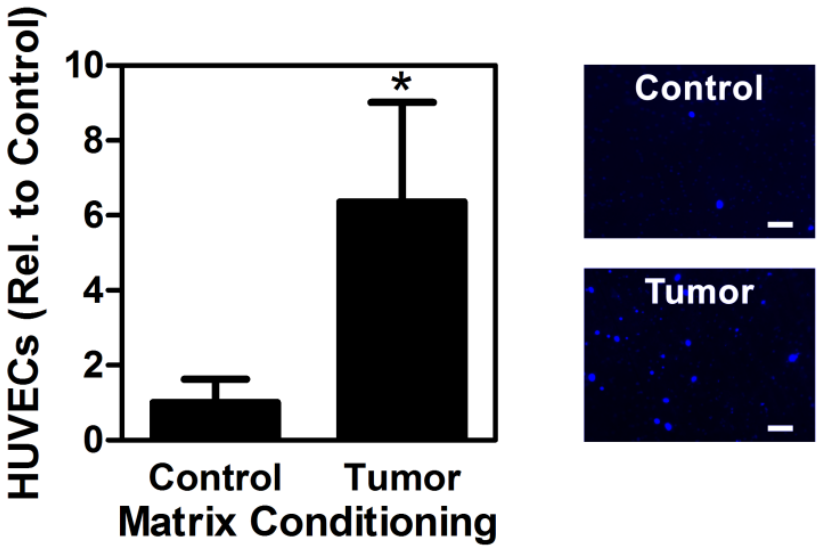

Figure 5.3: Pro-angiogenic potential is assessed via a transwell migration assay with HUVEC cells. Six times more HUVECs migrate toward media from 3T3-L1s cultured in tumour conditions as compared to the control. Representative micrographs are shown at right (nuclei stained blue with DAPI, scale bar = 10 µm.)

vein endothelial cells (HUVECs). As shown in Figure 5.3, six times more HUVECs migrated toward the tumour media, as compared to the control, confirming the increased pro-angiogenic potential of the stromal cell secretions cultured in tumour-mimicking ECMs.

5.4.3 Assessment of the Role of Fn via pUR4 Peptide Inclusion

In agreement with previous findings [69], the TCM-treated 3T3-L1 cells produced an ECM containing elevated quantities of Fn. To further identify whether Fn was a key regulator in the upregulation of VEGF secretion, pUR4 – a peptide

previously reported to block Fn incorporation into the matrix [98] – was used to produce Fn-null matrices. The addition of pUR4 inhibited Fn incorporation into the TCM treated stromal cell matrices (Figure 5.4A) and while the increased VEGF secretion by reseeded 3T3-L1 cells was still seen in the tumour condition, those matrices lacking Fn did not produce significantly higher VEGF secretion than controls (Figure 5.4B). The tumour ECM has long been known to contain higher quantities of Fn [88], and while Fn has been shown to influence various pro-tumourigenic functions including: angiogenesis [99], metastasis [100], and drug resistance [101], we show that it may additionally contribute to changing the local stromal pro-angiogenic behaviour.

5.4.4 Fn Conformation Alters Stromal Cell Pro-Angiogenic Behaviours

In addition to increasing Fn content in matrices, treatment of 3T3-L1 cells in TCM was previously shown to increase the concentration of Fn in an unfolded conformation within these matrices [69]. Accordingly, we continued by investigating the role of Fn conformation in causing alterations to the pro-angiogenic function of stormal cells. We hypothesized that the changes in Fn conformation played a key role in altering the pro-angiogenic potential of the 3T3-L1s, and we sought to isolate the effect of conformation from other potential variations in the ECM with the use of a conducting polymer device. This device is capable of establishing over a large area, any single conformation (or range of conformations) of adsorbed Fn from compact, to extended, to partially unfolded. Further, this is achieved without the accompanying changes to mechanical stiffness or

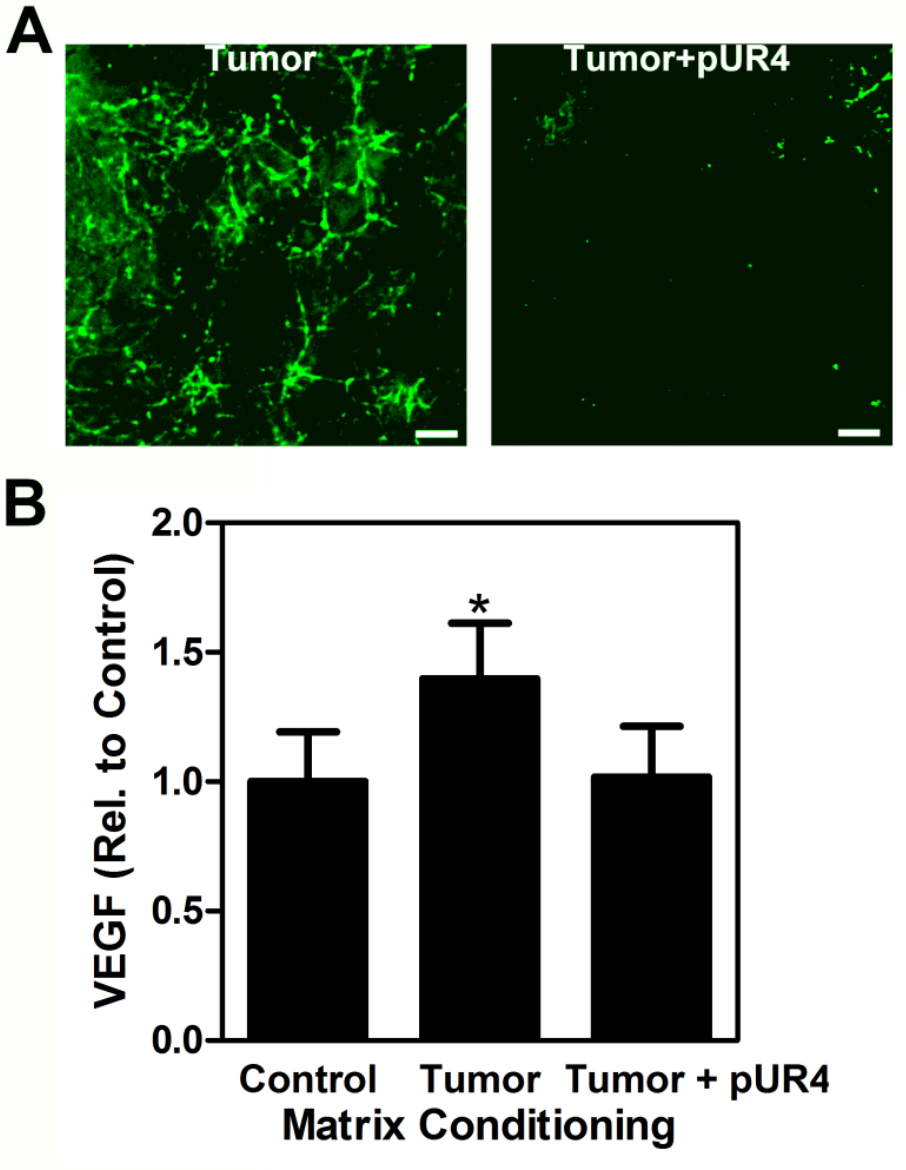

Figure 5.4: Matrices produced by 3T3-L1 cells in the presence of TCM (tumour) show elevated Fn content which is no longer enhanced when TCM is supplemented with the peptide (pUR4) that inhibits Fn incorporation into the matrix (**A**, scale bar = 20 µm). When normal 3T3-L1 cells are reseeded onto these matrices, only the matrix produced in the presence of TCM alone results in elevated VEGF secretions (**B**, * indicates $p < 0.05$).

biochemistry (i.e., composition) that likely occur in a complete ECM [11].

We first coated our devices with Fn in serum-free media for one hour under an applied bias of +1 V (1 V) to establish a compact (unfolded) conformation. We then seeded 3T3-L1s on the prepared surfaces and collected their media after 24 hours of culture to measure the amount of VEGF produced by cells on the different conformations. We observed that fewer (25%) cells adhered to the unfolded Fn as compared to the compact Fn (Figure 5.5A) the same behaviour observed with the tumour ECMs as compared to the control ECMs (Figure 5.2A), and in agreement with previous results that treatment of 3T3-L1 cells in TCM increased the incorporation of Fn in an unfolded conformation [69]. We found that cells cultured on our devices on unfolded Fn produced 40% more VEGF than cells cultured on compact Fn (Figure 5.5B), thus confirming that the observed changes in pro-angiogenic potential are linked to changes in Fn conformation.

We next repeated this experiment with serum-containing media (10% FBS) to test this effect in conditions more relevant to typical cell culture. We coated our devices with serum-containing media (no additional Fn) and subsequently cultured 3T3-L1s on them, as before. Under serum conditions, we again observed that fewer (40%) cells adhered to the unfolded Fn as compared to compact, and that the cells cultured on the unfolded conformation again produced more (65%) VEGF than those cultured on the compact conformation (Figure 5.5B).

We additionally investigated these effects with other cell types, including human mesenchymal stem cells (hMSCs), a stem cell often studied for its role in the tumour stromal compartment. We observed similar trends in VEGF production on the compact and unfolded protein conformations (Figure 5.5C), suggesting the applicability of these findings in a broader context of different, more

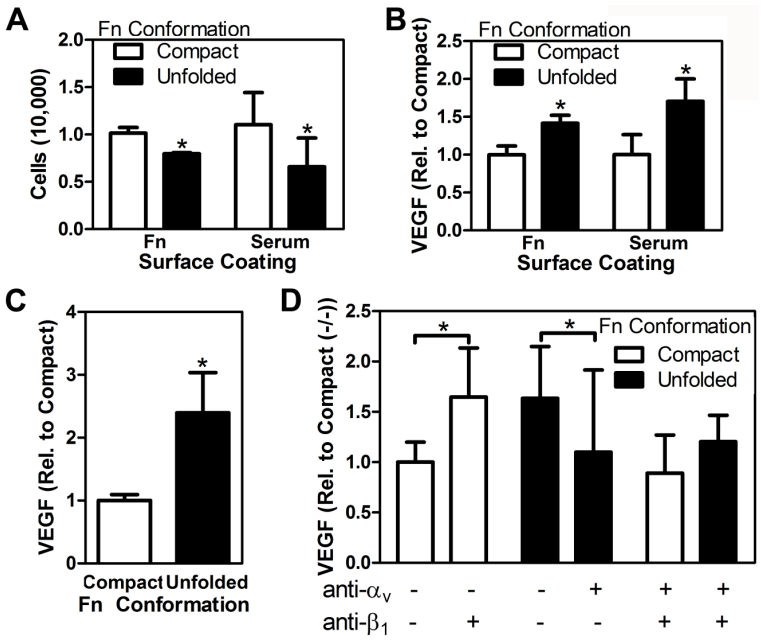

Figure 5.5: Oxidized or reduced PEDOT:PSS surfaces were coated with either fibronectin (Fn) only or 10% serum (containing Fn) in medium for 1 hour prior to cell seeding. With both types of coatings, Fn on the oxidized side assumed a compact conformation while Fn on the reduced side assumed an unfolded conformation. 3T3-L1 cells were seeded onto these surfaces, and fewer cells adhered to the unfolded conformation (**A**, * indicates $p < 0.05$ from matched compact conformation condition). The media from the 3T3-L1 cells seeded onto the surfaces was then analyzed via ELISA for VEGF content (**B**, * indicates $p < 0.05$ from matched compact conformation condition), showing increased secretion on the unfolded protein. Further analysis of other cell types (human mesenchymal stem cells) indicates similarly enhanced secretion of VEGF on the unfolded protein following serum coating (**C**, * indicates $p < 0.05$ from matched compact conformation condition). Neutralization of the and β_1 integrin subunit in the 3T3-L1 cells seeded onto the Fn in a compact conformation lead to an increase in VEGF secretion (**D**, white paired bars, * indicates $p < 0.05$). Meanwhile, neutralization of the α_v integrin subunit in 3T3-L1 cells resulted in a decrease in VEGF secretion by these cells on unfolded conformation (**D**, black paired bars, * indicates $p < 0.05$). No significant difference in VEGF secretion is seen between cells seeded onto compact vs. unfolded Fn when both integrin subunits are neutralized (**D**, final paired bars).

human-relevant cell types.

With these results implicating the importance of Fn conformation, we investigated the mechanism behind this effect by studying the roles of $\alpha_5\beta_1$ and $\alpha_v\beta_3$, two of the main integrins responsible for cell-Fn binding [102]. One of the key differences between the binding mechanisms of the two integrins is that $\alpha_5\beta_1$ binding is conformation-dependent, whereas $\alpha_v\beta_3$ binding is not [102, 103]. The $\alpha_5\beta_1$ integrin simultaneously binds the arginine-glycine-aspartic acid (RGD) sequence and synergy site on the neighbouring III_10 and III_9 modules of Fn, respectively [78]. As a result, extended and unfolded conformations would progressively increase the spatial separation between the RGD and synergy sites, thus progressively inhibiting $\alpha_5\beta_1$ binding. In these situations, cells might utilize more $\alpha_v\beta_3$ integrins for binding, to compensate for the reduced engagement of $\alpha_5\beta_1$ integrins [102]. Indeed, increased engagement of $\alpha_v\beta_3$ (historically known as the vitronectin receptor) has been linked to increases in VEGF production [26].

To further test this hypothesis, we investigated the effect that blocking the $\alpha_5\beta_1$ and $\alpha_v\beta_3$ integrins would have on VEGF production levels. We first inhibited $\alpha_5\beta_1$ with a β_1 function-blocking antibody in cells seeded on prepared serum-coated electrochemically-oxidized polymer devices where Fn was in a compact conformation. We observed that VEGF levels were increased on the compact Fn as compared to the control conditions with no antibody (Figure 5.5D, white paired bars). This suggests that these cells do increase VEGF production through some means of decreased $\alpha_5\beta_1$ utilization.

Next, we tested whether this increased secretion was due to a compensation of $\alpha_v\beta_3$ in response to decreased $\alpha_5\beta_1$ engagement. To this end $\alpha_v\beta_3$ was inhib-

ited, by adding an α_v function-blocking antibody to cells seeded on prepared serum-coated electrochemically-reduced polymer devices where Fn was in an unfolded conformation. Here, we observed that the typically enhanced VEGF production on unfolded conformations was inhibited, and VEGF levels were reduced back down to the levels observed on a control compact conformation surface (Figure 5.5D, black paired bars). This further supports the hypothesis that in the absence of any function-blocking antibodies, $\alpha_v\beta_3$ engagement is up-regulated on unfolded ECM protein conformations, which leads to a concomitant increase in VEGF production. This is in agreement with previous findings showing that conformational changes in Fn control the specificity of integrin engagement, specifically as a balance between $\alpha_v\beta_3$ and $\alpha_5\beta_1$ usage [102].

Finally, we inhibited both $\alpha_5\beta_1$ and $\alpha_v\beta_3$ simultaneously in cells seeded on prepared serum-coated conducting polymer devices (with compact and unfolded conformation surfaces). Here, we observed that the amount of VEGF secreted by stromal cells on both the compact and unfolded conformation surfaces were not significantly different from the amount of VEGF produced on a control compact surface (Figure 5.5D, final paired bars). This suggests that VEGF secretion does not increase while $\alpha_v\beta_3$ is inhibited, regardless of whether or not $\alpha_5\beta_1$ is also inhibited. This is likely due to a compensation by the cell to utilize $\alpha_v\beta_3$ when $\alpha_5\beta_1$ engagement is inhibited either due to conformational misalignment with Fn or due to function blocking antibodies. However, with blockade of the $\alpha_v\beta_3$ integrin, the upregulation in VEGF secretion that would result from increased $\alpha_v\beta_3$ integrin engagement is not achievable.

As a check, we verified that the measured differences in VEGF (shown in Figure 5.5**B** and **C**) were due to changes in cell secretions, rather than differ-

ential binding of VEGF to the altered conformations of fibronectin. We coated oxidized or reduced PEDOT:PSS surfaces with 10% serum (containing Fn) in medium for 1 hour to establish surfaces with altered Fn conformation. Then, we incubated the prepared surfaces with medium containing a known concentration of VEGF (150 pg/mL) for 2 hours to allow VEGF to bind to the surface-adsorbed Fn. After 2 hours, we collected the supernatant and measured the VEGF content via ELISA. The amount of surface-adsorbed VEGF was calculated by subtracting from the initial concentration. As shown in Figure 5.6, 15% more VEGF adsorbed to reduced surfaces (unfolded conformation). This is in agreement with previous work showing increased VEGF binding to unfolded Fn [104], and importantly, shows that the measured VEGF increase from cells on reduced surfaces is indeed due to enhanced cell secretions.

5.5 Conclusions and Perspectives

These findings have significance for a broad range of areas from tissue engineering to cancer biology. While our previous work has shown the conformation of Fn within in vitro tumour stromal cell matrices to be in a more unfolded conformation [69], we show here the significance of this conformational variability in Fn on the pro-angiogenic capacity of a tumour. As stromal cells only contribute in part to tumour angiogenesis, further work is necessary to understand the role of altered Fn conformation on the tumour cells, as well as other cells resident within the tumour microenvironment. Furthermore, as Fn and other proteins assume altered conformations when in contact with various surfaces [105], understanding how these conformational changes can alter cell functions, such as angiogenesis, will both improve our understanding of cell-biomaterial

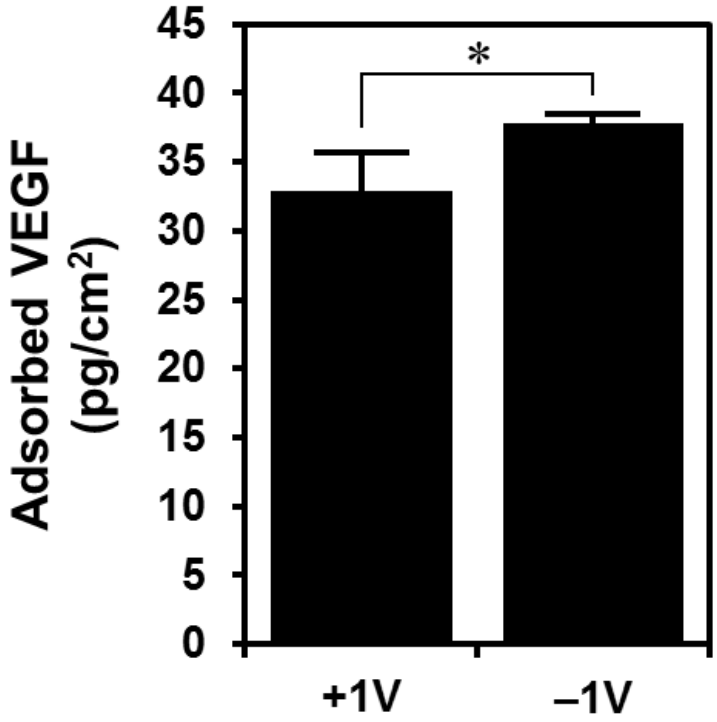

Figure 5.6: Oxidized or reduced PEDOT:PSS surfaces were coated with 10% serum (containing Fn) in medium for 1 hour to establish surfaces with altered Fn conformation, and then incubated with medium containing a known concentration of VEGF (150 pg/mL) for 2 hours to allow VEGF binding to surface Fn. After 2 hours, the supernatant was collected and VEGF content was measured via ELISA. 15% more VEGF was found to bind to reduced PEDOT:PSS surfaces (unfolded conformation), as compared to oxidized surfaces (compact conformation). * indicates $p < 0.05$).

interactions and expand our ability to harness those interactions for better tissue engineering approaches.

CHAPTER 6

3D CONDUCTING POLYMER SCAFFOLDS FOR CELL CULTURE

6.1 Contributors

This project is a collaboration between the Ober, Fischbach, and Giannelis groups. Lou Estevez (a graduate student in the Giannelis group) developed the original idea for the project with me, and led the initial efforts to develop 3D macroporous PEDOT:PSS scaffolds. Lou passed the project on to Tiffany Williams (a graduate student in the Giannelis group), who has been instrumental in optimizing the fabrication process, as well as characterizing the scaffolds. Claudia Fischbach, Delphine Gourdon, George Malliaras, and Chris Ober have provided useful suggestions in all experimental aspects of the project. Emmanuel Giannelis has contributed to the preparation of the manuscript.

6.2 Abstract

We report three-dimensional macroporous scaffolds made from a conducting polymer via ice-templating, that support live cell culture for upward of 7 days, and provide electrical control over cell adhesion and pro-angiogenic potential. Such structures may serve as a model to understand and control three-dimensional cell-surface interactions via electrical stimuli, with applications in basic research, medical diagnostics, and tissue engineering.

This work is in preparation for submission.

6.3 Introduction

Cell culture in two dimensions is convenient and can be well-controlled in the laboratory environment, leading to the widespread use of petri dishes, tissue culture flasks, and other planar substrates for cell culture. While 2-dimensional systems offer the benefits of consistent, repeatable structures, and ease of use, we must always be mindful that cells *in vivo* exist in a 3-dimensional microenvironment (even those cells that grow in monolayers), and that their behaviour can be radically different due to the microenvironmental changes implicit in a 3-dimensional system [14, 106–108]. For this reason, much recent work has focused on developing 3-dimensional scaffold systems that can both support 3D cell cultures and mimic *in vivo* tissue properties to some degree.

While many strategies for such structures exist, including hydrogels, electrospun networks, and macroporous scaffolds of various kinds, all must be designed with the ability to support cell attachment and allow for oxygen and nutrient transport (diffusion).

With the goal of developing an electrically conducting 3D scaffold, we fabricated 3-dimensional macroporous scaffolds made from PEDOT:PSS, yielding an electrochemically-active device architecture capable of supporting 3-dimensional cell culture. Using such scaffolds, we examined the behaviour of cell adhesion and secretions in a 3D environment, as a function of the oxidation state of the PEDOT:PSS scaffolds.

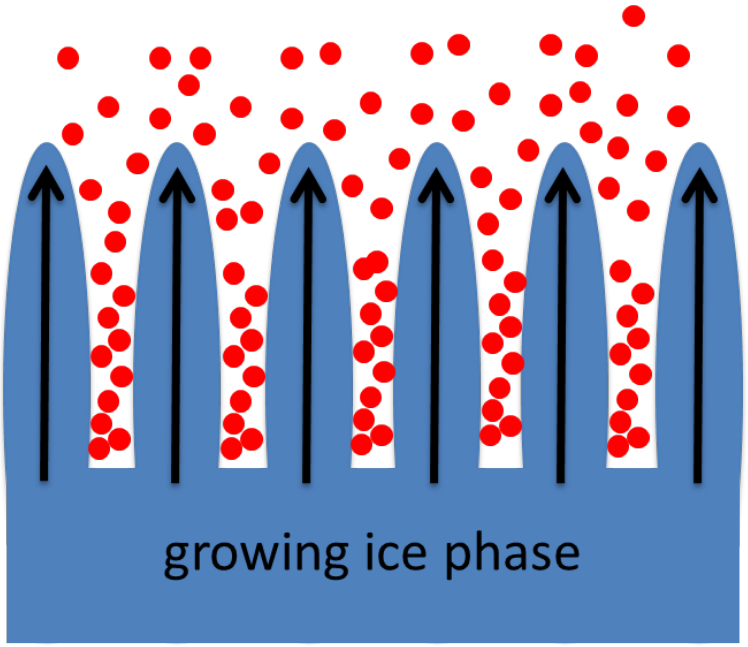

Figure 6.1: As the suspension freezes, the growing solvent ice phase (blue) confines dispersed particles (red) into the regions between ice domains.

6.4 Ice Templating

Among the various methods that have been developed for preparing macroporous scaffold-type structures, ice templating (freeze casting) has attracted considerable attention due to its versatility and low cost. As shown schematically in Figure 6.1, ice templating exploits spontaneous phase segregation during the solidification of a suspension, leading to induced ordering of dispersed particles that are confined to the regions between solvent crystals [109–112]. Subsequent sublimation of the solvent ice phase leaves behind the solid scaffold structure composed of the dispersed particles, which can be baked or sintered as required to stabilize the structure.

To date, ice-templating work has emphasized suspensions of ceramic

nanoparticles (occasionally with an organic binder) [110–113], with other work focusing on scaffolds based on poly(vinyl alcohol) (PVA), poly(vinyl laurate) (PVL), poly(lactic acid) (PLA), poly(acrylamide), and polystyrene (PS), either with or without inorganic nanofillers (i.e., silica, ceria, clay, carbon nanotubes) [114–118]. More recently, scaffolds with electronic and/or ionic conductivity have been demonstrated, such as in the case of graphene/platinum/nafion hybrid scaffolds [119], and preliminary studies into sheet-like 3D structures of PEDOT:PSS [120].

6.5 Macroporous PEDOT:PSS scaffolds

Scaffolds were fabricated from an aqueous dispersion of PEDOT:PSS (PH-1000, Heraeus) at a concentration of 1.25 wt%, with 3-glycidoxypropyltrimethoxysilane (GOPS) added as a crosslinker at 3 wt% to improve stability in water for long-term cell culture. The PEDOT:PSS/GOPS solution was poured into rectangular teflon molds, $7 \times 4 \times 2$ mm in size. The samples were then placed in a freeze-dryer, where they were frozen from 5 °C to −40 °C at a controlled rate of −0.9 °C/minute, after which the ice phase was sublimed from the scaffolds. Following sublimation, the scaffolds were baked at 140 °C to anneal the PEDOT:PSS phase.

Mercury porosimetry revealed that the remaining PEDOT:PSS scaffolds were highly porous, with a total pore area of 2.34 m^2/g and a median pore diameter of 35 µm (Figure 6.2). Pore volume was measured at upward of 98%, confirming the porous, open structure of the scaffolds.

A dynamic mechanical analysis (DMA) instrument was used to measure

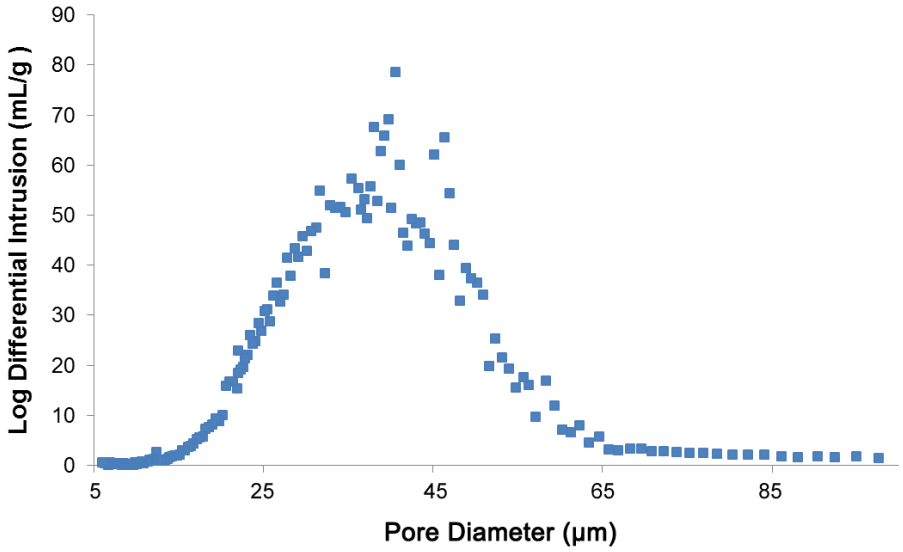

Figure 6.2: Mercury porosimetry data for a PEDOT:PSS scaffold, yielding a total pore area of 2.34 m^2/g and a median pore diameter of 35 µm.

the elastic modulus of scaffolds made from PEDOT:PSS either with or without 3 wt% GOPS, and in either dry or wet conditions (in αMEM cell culture medium). Measurements were performed with a single loading cycle, with an initial contact force of 0.05 N and loaded at a fixed force-rate of 0.005 N/minute. A fixed force-rate was used rather than a fixed strain-rate, for reasons of better control (as recommended by the manufacturer, TA Instruments). Typical force curves obtained from the measurements are shown in Figure 6.3. Elastic modulus was calculated as the slope of the linear part of the stress-strain curve near zero strain. Dry scaffolds without GOPS were found to have an elastic modulus of 360 Pa, while wet scaffolds with 3 wt% GOPS had an elastic modulus of 750 Pa, indicating good matches with the mechanical stiffnesses of a variety of tissue types *in vivo* [121].

These values for both pore size and elastic modulus can be tuned by adjust-

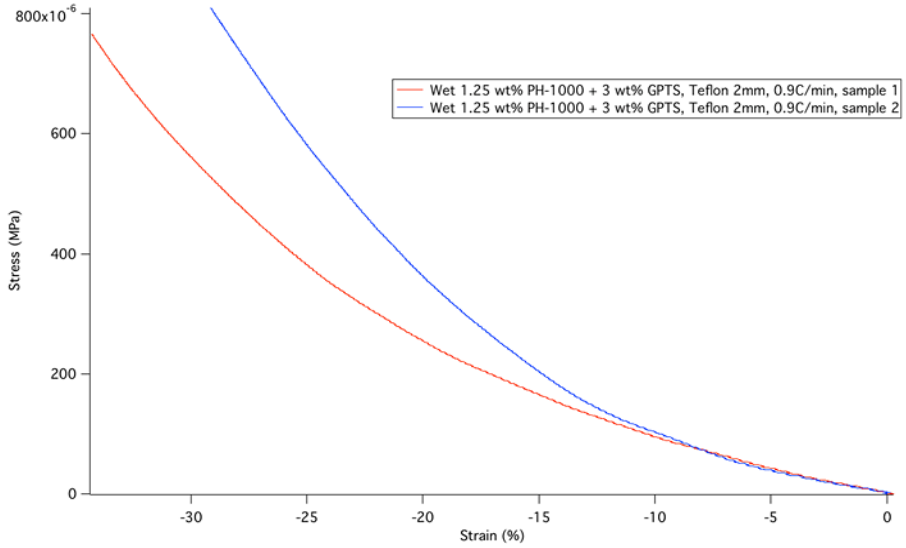

Figure 6.3: Representative force curves from a compression cycle, obtained with a dynamic mechanical analysis tool, from a PEDOT:PSS scaffold with 3 wt% GOPS, submerged in αMEM. Elastic modulus is calculated as the slope of the linear part of the curves near zero strain.

ing the fabrication protocol. Lowering the freezing rate generally increases pore diameter, which would be preferred for this application (pore sizes on the order of 100 µm to 300 µm would be better for cell culture, similar to the pores found in PLGA scaffolds used by the Fischbach group and others). Additionally, reducing the amount of GOPS crosslinker would slightly increase the median pore size.

6.6 Electrical Control of Cell Behaviour

Electrodes were attached to pairs of scaffolds, which were submerged in electrically-grounded αMEM with 10% fetal bovine serum (FBS) and 1% penicillin-streptomycin. A bipolar power supply sourced an oxidizing poten-

tial of +1 V to one scaffold, and a reducing potential of −1 V to the other. The bias was maintained for 1 hour at 37 °C, after which the scaffolds were removed from the electrodes and placed in individual wells of a 12-well plate. 3T3-L1 mouse preadipocytes were seeded at a density of 1.5 million cells in 30 µL of αMEM (containing 33% matrigel, to promote adhesion), and allowed to adhere in an incubator for 30 minutes. Fresh media was then added to the wells and the plates were incubated on a shaker plate to promote media circulation for oxygen/nutrient diffusion.

It should be noted that the use of matrigel often led to the formation of a thick white layer (likely of collagen) at the top (seeding) surface of the scaffolds, even though the cell suspension (containing matrigel) was kept cold (on ice) prior to seeding to prevent collagen polymerization. This collagen layer made surface-characterization difficult (i.e., via SEM imaging). Seeding was attempted in the absence of matrigel, but many cells flowed through the scaffold and out onto the plate underneath, significantly lowering seeding density. Future efforts should focus on seeding the cells with a lower amount of matrigel, or in a smaller volume in the absence of matrigel, to mitigate these problems.

Cell behaviour was typically investigated after 24 hours of culture (with the exception of viability assays performed out to 7 days of culture to verify the long-term viability of cells cultured in such scaffolds). Scaffolds were rinsed in PBS and soaked in 4% ice-cold paraformaldehyde for 45 minutes for chemical fixation.

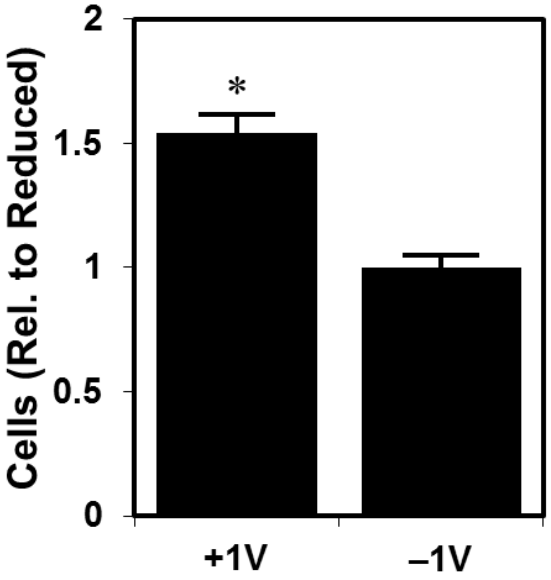

Figure 6.4: Cell number was quantified via fluorometric DNA assays. 50% more cells adhered to oxidized (+1 V) scaffolds as compared to reduced (−1 V) scaffolds. * indicates $p < 0.05$.

6.6.1 Cell Adhesion

Cell adhesion was quantified after 24 hours of culture via a fluorometric DNA assay, after the scaffolds were cut apart and their cells were lysed. Adhesion to the oxidized scaffolds was stronger, with 50% more cells counted in oxidized scaffolds as compared to reduced scaffolds (Figure 6.4).

Scaffolds were also prepared for scanning electron microscopy (SEM) to assess and visualize cell infiltration of the scaffolds. After 24 hours of culture, the scaffolds were chemically fixed as described above, and either rinsed in PBS or DI water to remove excess formaldehyde. They were then placed in a freeze-dryer to remove the water via sublimation (to avoid structural damage from evaporation due to the high surface tension of water). The scaffolds were

then microtomed at a shallow angle relative to the top face, to expose a range of depths for imaging. After being coated with a conductive Au/Pd sputtered layer, the scaffolds were imaged in an SEM.

Rinsing the scaffolds after chemical fixation in PBS retained cell integrity (due to PBS being isotonic), but resulted in undesired salt crystals that were visible in SEM images on some occasions. Salt crystals were not always visible, however, as seen in the micrograph in Figure 6.5, showing successful intrusion of cells into the scaffolds. The presence of salt crystals may have been mitigated in this case by using a smaller volume of PBS for the final rinse just prior to freeze-drying.

Rinsing in DI water removed any possibility of remaining salt crystals, but resulted in undesired cell lysis (due to DI water being hypotonic); however, this did enable imaging of cell-made protein fibers in the scaffolds (Figure 6.6) that would otherwise have been obscured by the cells themselves. The size of the fibers suggests that they are too large to be fibronectin, and may be made from matrigel-derived collagen.

Fibronectin immunostaining of scaffolds after 24 hours of culture revealed that fibronectin fibers are also present in the scaffolds (in addition to the fibers observed via SEM that were likely collagen), as shown in Figure 6.7.

Viability assays were performed to investigate whether cells could survive in the PEDOT:PSS scaffolds for long periods of time. To this end, cells were cultured in scaffolds for up to 7 days (with media replacement every 2 days). After 7 days, a viability assay confirmed that the vast majority of cells at the scaffold surface remained alive (Figure 6.8). Future imaging of a scaffold cross-section

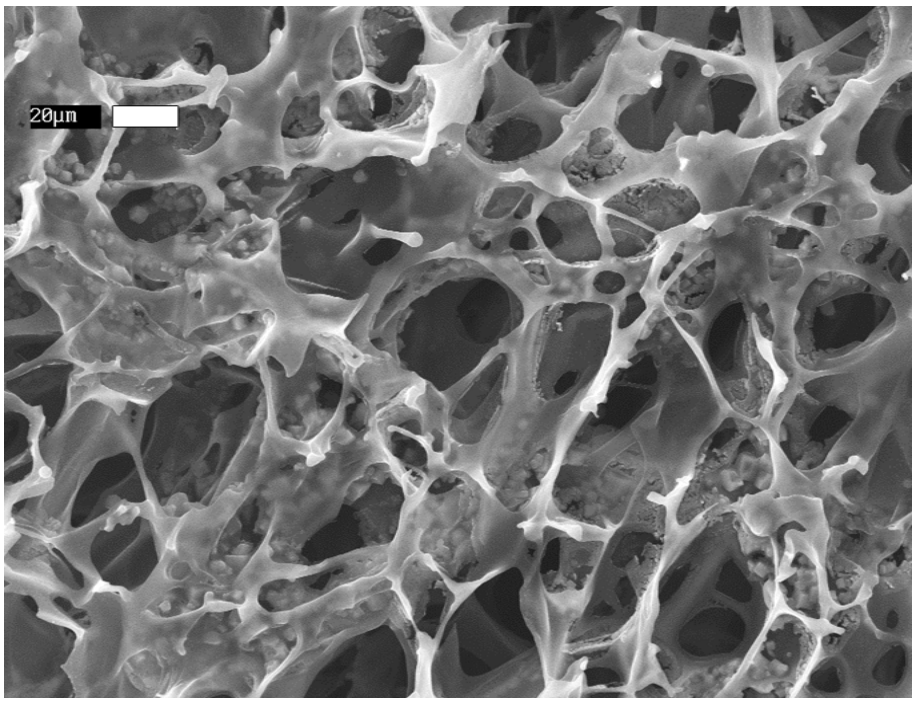

Figure 6.5: Scanning electron micrograph showing a PEDOT:PSS scaffold after 24 hours of culture, infiltrated by 3T3-L1 cells that were seeded with matrigel. Scale bar is 20 µm.

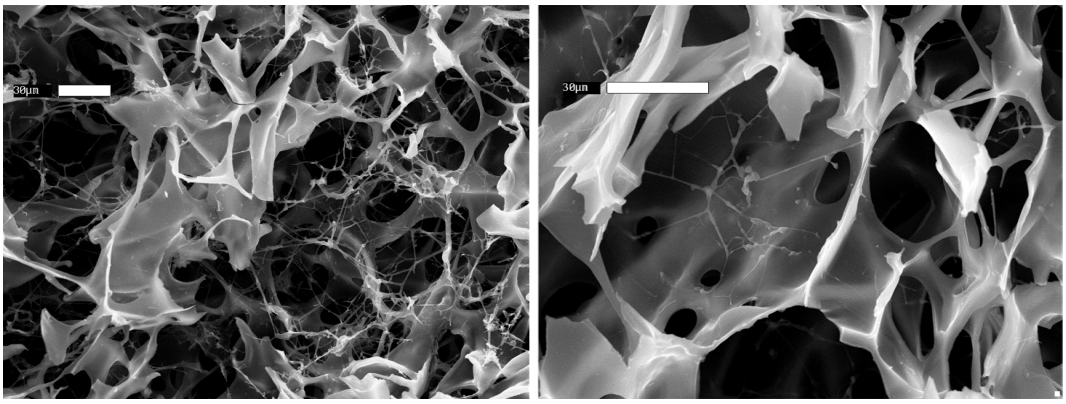

Figure 6.6: Scanning electron micrographs taken after 24 hours of cell culture, showing protein fibers made by 3T3-L1 cells seeded with matrigel into a PEDOT:PSS scaffold. Cells were lysed in a DI water rinse prior to imaging, resulting in improved visibility of the fibers. The fibers are likely too large to be fibronectin, and are likely made from matrigel-derived collagen. Scale bars are 30 µm.

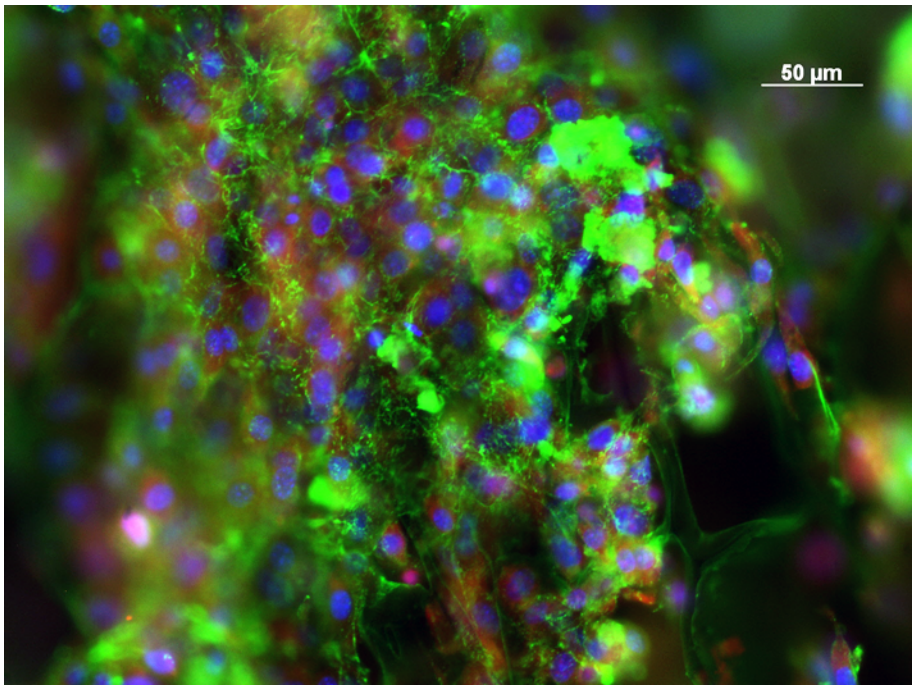

Figure 6.7: Fluorescence micrograph showing immunostained fibronectin fibers (green) within a scaffold after 24 hours of culture. Nuclei are stained with DAPI (blue) and dead cells are stained with propidium iodide (red).

would provide useful information about viability throughout the scaffolds.

6.6.2 Pro-Angiogenic Potential

To assess changes in the pro-angiogenic potential of 3T3-L1 cells cultured in oxidized vs. reduced conditions, we measured the amount of VEGF secreted over 24 hours via ELISA. We found that cells cultured in reduced scaffolds secreted 4 times more VEGF than those cultured in oxidized scaffolds (Figure 6.9. This is in agreement with previous results (Chapter 5), where 3T3-L1 cells on reduced PEDOT:PSS surfaces (where surface-adsorbed fibronectin was electrochemically-induced into assuming an unfolded conformation) also secreted more VEGF

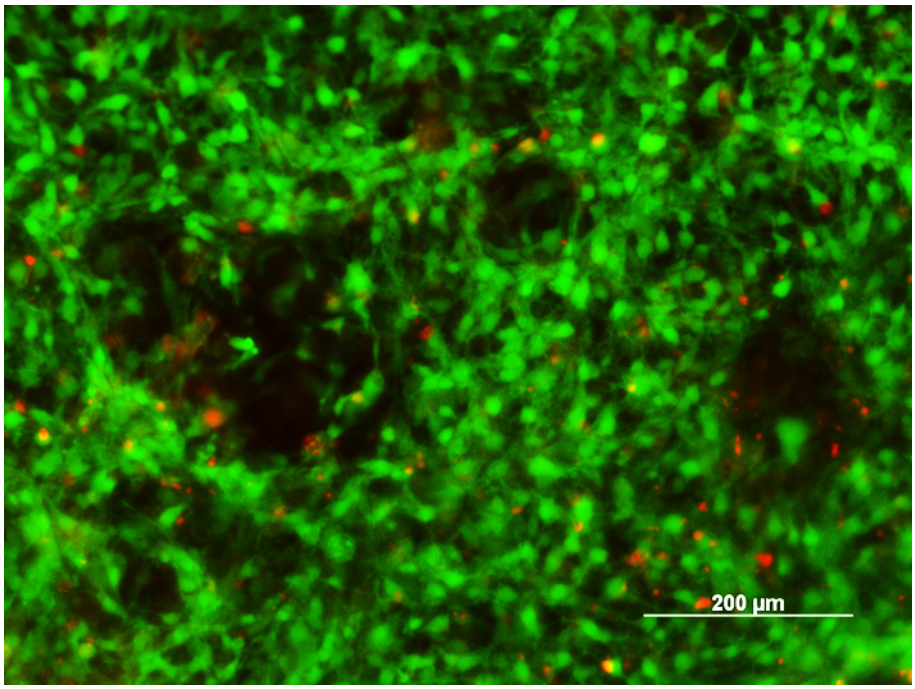

Figure 6.8: Fluorescence micrograph of a scaffold surface after viability staining at $t = 7$ days. Live cells are stained with calcein (green), and dead cells are stained with propidium iodide (red). The pores of the scaffold are visible as large circular darkened regions.

than those cultured on oxidized surfaces (with compact fibronectin).

Importantly, this is in agreement with previous results [69] showing that fibronectin in the tumour microenvironment assumes a more unfolded conformation as compared to healthy tissue. The observed up-regulated secretion of the pro-angiogenic molecule VEGF in the 3-dimensional environment of the PEDOT:PSS scaffolds implicates the role of protein conformation in the pro-angiogenic reponse of cells in the tumour microenvironment.

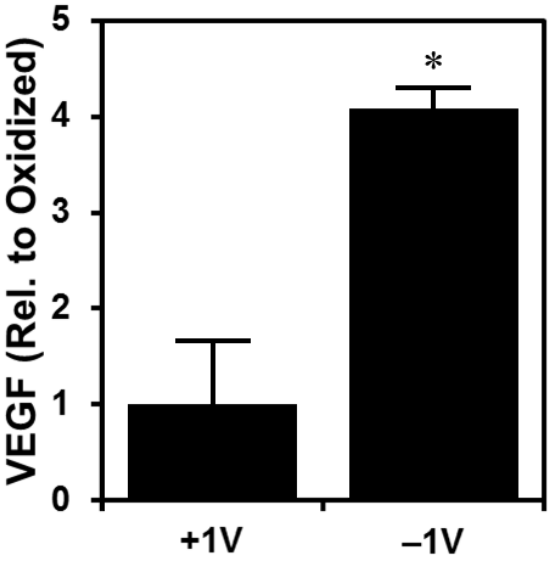

Figure 6.9: Four times more VEGF was secreted by cells cultured in oxidized (+1 V) scaffolds as compared to reduced (−1 V) scaffolds. * indicates $p < 0.01$.

6.7 Conclusions and Perspectives

We developed 3-dimensional macroporous scaffolds made from PEDOT:PSS, which exhibit electrical conductivity, and possess mechanical stiffness values that provide a good match with a variety of tissue types. 3T3-L1 cells were successfully cultured in theses scaffolds, and remained viable for over 7 days of culture. Additionally, electrochemical oxidation/reduction of the scaffolds prior to cell-seeding allowed control over the subsequent adhesion and secretions of 3T3-L1 cells cultured therein.

After 24 hours of culture, cells adhered in greater numbers (50% more) in oxidized scaffolds as compared to reduced scaffolds, and levels of secreted VEGF were 4 times higher in reduced scaffolds as compared to oxidized scaffolds. These trends recapitulate both the redox-dependent adhesion and secre-

tion behaviours observed in 2-dimensional thin-film systems, but appear to be enhanced in magnitude.

These results demonstrate the suitability of ice-templated macroporous PEDOT:PSS scaffolds for 3-dimensional cell culture experiments under electrochemical stimuli. Models could be developed for a variety of tissue types with stiffnesses ranging from ~0.1 kPa to 10 kPa, owing to the simple adjustability of scaffold stiffness (by varying the amount of crosslinker). Using this scaffold architecture for mono- or even co-cultures of different cell types could enable interesting 3-dimensional studies of cell behaviour as a function of local protein conformation and the electrical microenvironment.

CHAPTER 7

CONCLUSIONS AND PERSPECTIVES

The work presented in this dissertation centred around the use of two variants of the conducting polymer poly(3,4-ethylenedioxythiophene): one doped with *p*-toluenesulfonate (PEDOT:TOS) and one doped with poly(styrenesulfonate) (PEDOT:PSS) as presented in Chapter 1. This organic electronic material was used at the interface with proteins and live cell cultures in two different architectures – as planar thin-film devices, and as three-dimensional macroporous scaffolds. Results were presented demonstrating the electrochemically-mediated control of cell adhesion, cell motility, protein conformation, and pro-angiogenic cell secretions. This work establishes the use of this class of organic electronic materials as active interfaces for cell studies, and points toward many possible interesting extensions and areas for future investigation.

Cell Adhesion

In Chapter 2, a simple planar device was introduced based on thin films of PEDOT:TOS. Applying a linear voltage gradient from +1 V to −1 V established a semi-permanent redox gradient in the PEDOT:TOS film which remained after the bias was removed. Two different types of cells (3T3-L1 mouse fibroblasts and MDA-MB231 human breast cancer cells) were cultured on these surfaces and their adhesion characteristics were evaluated.

Cell adhesion was modulated for both 3T3-L1s and MDA-MB231s, and quantified in terms of the local density of cells as a function of applied redox

potential. In both cases, cell density gradients were established, with large numbers of cells (at densities reaching those of confluent monolayers) on the oxidized and neutral regions of the PEDOT:TOS films, and increasingly fewer cells toward the reduced end of the film. Thus, this device demonstrates the ability to spatially control cell adhesion with an electrical stimulus.

It is worth noting that while both cell types tested in these experiments exhibited the same adhesion characteristics, finding two cell types that adhered preferentially to opposite redox states (for example, as demonstrated for MDCK cells by Bolin and coworkers [122]) could enable interesting cell-sorting capabilities.

Cell Motility

In Chapter 3, the same planar PEDOT:TOS thin-film device described in Chapter 2 was used to investigate electrical control over cell motility. Bovine aortic endothelial cells (BAECs) were cultured along a PEDOT:TOS stripe which had been pre-biased with a linear voltage gradient. When the BAECs were observed over a period of six hours, marked differences were observed in their migration behaviour on oxidized vs. reduced regions of the polymer. In terms of both migration speed and persistence time, a 3-fold increase was observed on the most oxidized regions of the polymer as compared to the most reduced regions. Thus, this device demonstrates the ability to control the migration characteristics of cells, in addition to the spatial control over cell adhesion demonstrated in Chapter 2.

It is worth noting that although persistence time was substantially increased

on oxidized surfaces, cells did not migrate in a preferential direction with respect to the electrochemical gradient (i.e., toward either the oxidized or reduced end). This is likely because the slope of the gradient is too weak to be noticeable on the length-scale of a single cell: a gradient of ±1 V over a length of 2 cm (an electric field strength of 1 V/cm) translates to an equivalent potential drop of 2 mV across a 20 µm-wide cell. Such a small potential difference likely results in virtually undetectable differences in the oxidation state (or surface energy, pH, etc.) of the polymer substrate, thus preventing the likelihood of directed cell migration.

With the powerful repertoire of available lithographic techniques, much smaller PEDOT:TOS channels could be created to enable significantly stronger electric fields without exceeding the ~1.3 V potential barrier (with respect to the electrolyte) beyond which undesired electrolysis of the electrolyte would occur. Sufficiently strong electric fields could establish a steep enough redox gradient that would be detectable by single cells. Such conditions would likely result in directed cell migration along the direction of the gradient (either parallel or anti-parallel) on oxidized surfaces, where persistence time is elevated. This could enable interesting cell-sorting capabilities, if different cell types are found to migrate at sufficiently different speeds.

Fibronectin Conformation

In light of the results presented in Chapters 2 and 3, we sought to investigate the biological mechanism by which the altered local redox state of a PEDOT:TOS substrate was affecting cell adhesion and motility. Owing to the critical role

played by adhesion proteins in cell-substrate adhesion characteristics, we chose to investigate the role of fibronectin, an adhesion protein of known importance. Initial studies of differential Fn (mass) adsorption via immunostaining and XPS were inconclusive, so we proceeded to study Fn molecular conformation via Förster Resonance Energy Transfer (FRET) studies.

In Chapter 4, two variants of the PEDOT:TOS thin film device used in the preceding cell adhesion and secretion studies were used to investigate the molecular conformation of fibronectin molecules that were adsorbed under an applied bias. Under a potential gradient from +1 V to −1 V, Fn conformation was found to vary monotonically and gradually from compact, through extended, to partially-unfolded. This monotonic relationship between FRET ratio (and therefore, Fn conformation) and applied bias gives, in essence, a calibration curve that conveniently maps any desired conformation to a corresponding electrical potential.

Using a modified device architecture with two large pixels (rather than a single connected stripe), single conformations were established across entire pixels. This enables cells to be cultured on a surface with a precisely-defined fibronectin conformation, allowing definitive studies of cell behaviour as a function of protein conformation. To this end, 3T3-L1s were cultured on oxidized and reduced PEDOT:TOS pixels with compact and unfolded fibronectin, respectively. More cells adhered to the oxidized pixels (with compact Fn) as compared to the reduced pixels (with unfolded Fn). Further, when a function-blocking antibody was introduced to block usage of the $\alpha_5\beta_1$ integrin, cell numbers equalized on the compact and unfolded conformations. This implicates the role of the $\alpha_5\beta_1$ integrin in conformation-dependent cell adhesion, providing a biolog-

ical mechanism underlying the adhesion and motility characteristics observed earlier (since motility is intimately related to strength of adhesion).

Importantly, mechanical stiffness of the protein-coated surfaces was unchanged regardless of oxidation state, indicating that such devices control protein conformation *in isolation*, without associated changes to mechanical properties or biochemistry.

Conformation-Mediated Pro-Angiogenic Potential

The ability to control protein conformation as an isolated parameter was exploited in Chapter 5 to study protein conformation-mediated pro-angiogenic potential in stromal cells, in a way that is inaccessible to traditional experiments. Previous work by Chandler and coworkers [69] showed that fibronectin fibers were altered in the tumour environment, where they exhibited a more extended conformation and higher mechanical stiffness than fibers produced in healthy tissue. Since tumours are associated with increased pro-angiogenic activity, we sought to investigate the role played by fibronectin in this process.

Using cell-derived matrices produced in tumour and normal conditions, alterations to fibronectin were implicated in the increased pro-angiogenic potential of 3T3-L1s cultured in a tumour environment; however, the specific role of altered (extended) conformation could not be isolated from changes to protein quantity (increased) and matrix stiffness (increased). Thus, devices with PEDOT:PSS pixels were used to establish surfaces with adsorbed proteins (including fibronectin) in compact (control) and unfolded (tumour) conformations, while maintaining stiffness and the concentration of the coating solution (it is

not clear whether differential *mass* adsorption occurs. A definitive answer could be obtained by employing a Quartz Crystal Microbalance to measure mass directly, or perhaps more simply with singly-labeled fluorescent fibronectin to measure molecular density directly).

By culturing large populations of 3T3-L1s on the prepared pixels and measuring the amount of secreted VEGF in the supernatant after 24 hours, the role of altered fibronectin conformation was confirmed in increasing pro-angiogenic potential. Additionally, integrin blocking experiments revealed the conformation-dependent mechanism by which VEGF production is affected. By blocking the $\alpha_5\beta_1$ and $\alpha_v\beta_3$ integrins separately, and simultaneously, we observed that unfolded fibronectin inhibited $\alpha_5\beta_1$ binding, which caused a compensatory increase in $\alpha_v\beta_3$ binding (and increased levels of $\alpha_v\beta_3$ are linked to increased VEGF production).

3D Macroporous PEDOT:PSS Scaffolds

With all of the previous results coming from 2-dimensional thin-film device studies, we sought to develop a similar electrically-active cell culture system that could provide the increased physiological relevance of a 3-dimensional environment. In collaboration with the Giannelis group, we developed a method to produce macroporous PEDOT:PSS scaffolds via ice-templating.

In Chapter 6, scaffolds were produced with control over pore size and mechanical properties, and were found to be biocompatible and to support viable 3T3-L1 cultures for upward of 7 days. Entire scaffolds could be oxidized (+1 V) or reduced (−1 V) in media for 1 hour prior to seeding cells, allowing adhesion

and secretions studies to be performed similar to those reported in Chapters 2 and 5, respectively.

Cell adhesion was quantified after 24 hours of culture by cutting apart the scaffolds and lysing the cells in it to release their DNA into solution. The total amount of DNA was measured with a fluorometric DNA assay, allowing quantification of the total number of cells in each scaffold. Oxidized scaffolds contained 50% more cells than reduced scaffolds, suggesting that the adhesion trends observed in Chapter 2 in 2D are recapitulated in the 3D environment as well.

Presumably the differences in cell adhesion are due to differences in protein (fibronectin) conformation, as observed in the 2D thin-film system. FRET studies were not conducted to verify this due to the expense of the experiment in terms of the large volumes of FRET-labeled Fn that would be required (and that were not available at the time). With some system optimization, the required volume could be reduced to a more reasonable level, which should theoretically enable experimental confirmation that protein conformation is altered on the 3D scaffold surface as it is on 2D films. The curvature of the scaffold pores would somewhat complicate the FRET imaging process, but acquiring images with sufficiently large regions in focus should be possible.

It is worth noting that the voltage-dependent conformation of adsorbed proteins may well be similar to that found in the 2D film system of Chapter 4 due to the relatively large radius of curvature of the pores ($R \sim 10\,\text{s}$ to $100\,\text{s}$ of μm) with respect to the size of the adsorbed protein molecules ($10\,\text{s}$ of nm). Hence, on the local scale of a protein molecule, the majority of a pore surface is likely to be effectively 2-dimensional, with smaller pore edge and protrusion features pos-

sibly having a small enough radius of curvature that they might substantially affect fibronectin conformation. A careful FRET study could investigate whether such a geometrical/topological effect exists with regard to the different-sized features found in a scaffold.

Cell secretions from 3T3-L1s were evaluated by measuring VEGF content (via ELISA) in the supernatant collected from scaffolds cultured for 24 hours. Cells in reduced scaffolds secreted substantially more (4 times more) VEGF than those cultured in oxidized scaffolds. This matches the trend observed in Chapter 5 in the 2D thin-film system, but the increase observed in 3D is much more pronounced. It is unclear at this time why the increase is so much larger in 3D, but may be related to increased cell-cell contact (due to the nature of the 3D environment, as well as a potentially higher cell density).

The conducting polymer scaffold system presented here offers potential for further studies into cell behaviour (i.e., differentiation, proliferation, etc.) as a function of protein conformation (via oxidation state) in a 3-dimensional environment. The mechanical stiffness measured for the scaffolds matches well with the moduli of a variety of soft tissues *in vivo* [121]. Further tuning of pore size is required, however, with the goal to increase the mean pore diameter from ~40 µm up to 100 – 400 µm (to better match the pore sizes found in the well-studied gas foaming particulate leaching PLGA scaffold system [123]).

This can be achieved via three separate strategies: by lowering the ratio of cross-linker (3-glycidoxypropyltrimethoxysilane, GOPS) to PEDOT:PSS in the scaffold, by lowering the overall concentration of the solution from which the scaffolds are freeze-casted, and by decreasing the rate of cooling during the freeze-casting step.

The current amount of crosslinker (3% by weight in the casting solution) is unnecessarily high for the intended purpose of providing long-term stability in an aqueous environment – a recent test showed that scaffolds produced with 0.125% GOPS were stable in cell culture medium for 24 hours with no apparent degradation, although they showed significantly more electrochemical degradation when under an applied bias. A GOPS concentration closer to 1% by weight should provide sufficient electrochemical (and aqueous) stability, while increasing pore size slightly.

Pore size can also be increased by diluting the starting solution to a lower overall concentration. The stock PEDOT:PSS solution is purchased at 1.25% by weight in water, to which GOPS can optionally be added. Diluting this solution with water should yield final scaffolds with larger pores, although likely with a concomitant decrease in mechanical stiffness. If the resulting stiffness was undesirably low for the application at hand, increasing the GOPS content should raise stiffness considerably without entirely offsetting the increased pore size due to the dilution.

Finally, pore size can be further tuned by adjusting the freezing conditions during the freeze-casting process. A slower freezing rate (lower than the current $-0.9\,^{\circ}\mathrm{C}$/minute) should produce larger pores, and is easily controlled by the freeze dryer. All of the three strategies presented above are currently being investigated, and further study should yield protocols to produce scaffolds with any desired pore size and elastic modulus.

Final Perspectives

Opportunities exist to better characterize the materials property changes that occur in the PEDOT systems under electrochemical oxidation and reduction, in particular regarding the temporal dependence of many of the property changes observed.

For example, surface energy in thin films was measured via water contact angle in Figure 1.6, several hours (in air) after electrochemical oxidation/reduction. While this change in redox state appears to be relatively permanent in air (on the time-scale of months to years, as assessed by eye due to the photochromic change), it is much less permanent in solution where it appears to dissipate over the course of days. It would be interesting to investigate the time-dependent evolution of the water contact angle due to immersion in an aqueous medium. This could yield interesting materials science information, although it is worth noting that in the context of cell culture, the chemical/energy properties of the surface are likely of significantly decreased importance once the surface has been coated with cells that then produce a (microns) thick protein matrix.

Similarly, surface pH changed with redox state as measured (in solution) in Chapter 4. The change is likely due to the expulsion of protons from the oxidized film (thus deprotonating the sulfonic acid groups in PSS or TOS and lowering pH), and the reverse for the reduced film. It would be worth investigating the time dependence of this chemical change after immersion in cell media, and additionally, measuring the actual local pH at the surface of the film (both during and after the applied bias) would be challenging but could yield

useful information.

Further, detailed characterization of the precise nature of the chemical change in PEDOT is required. While the sulfonic acid moiety is almost certainly responsible for the pH change, it is important to understand the chemical change in greater detail (and to determine if other mobile species from solution become present in the film). Understanding this could allow the rational design of surfaces via chemistry alone, that could exhibit the same cell-altering properties while avoiding some of the technical complications introduced by the need for an external electrical circuit. While the conducting polymer system was certainly needed for the gradient configurations presented in Chapters 2–4, it offers no significant benefit over chemical functionalization for the pixel configuration presented in Chapter 5 other than reversibility, which has not been successfully utilized to date. Therefore, future studies utilizing functionalized surfaces (without the need for a gradient) could benefit from the greater control and variety offered by chemical functionalization.

One area of great interest to many who have seen the work in Chapter 4 is the dynamics of protein folding on the surfaces presented here. Information on both the time-scale and reversibility of conformational changes would be very interesting, and in theory should be obtainable. In practice, the experiment involves pseudo-real-time FRET measurements during reversible electrochemical oxidation/reduction, and it has proven to be extremely difficult. Briefly, a two-pixel thin-film sample is mounted onto a coverslip with an electrolyte solution containing FRET-labeled Fn, and is placed on a confocal microscope for imaging. The device is simultaneously connected to an external voltage source via a single-pole, double-throw switch, which allows the polarity of the circuit to be

rapidly reversed. A sufficiently slow scanning speed is selected on the microscope such that a single image takes on the order of 1–2 minutes to fully raster line-by-line. During the acquisition of the image, the polarity of the circuit can be switched as desired, and FRET values can theoretically be calculated as a function of time from the known scan-speed. Currently, there exists too much intensity variation within a single field of view (due to sample-tilt, etc.) to extract believable FRET data. With optimization, however, this could prove to be fruitful.

In all, the work presented in this dissertation represents an initial investigation into the ways that organic electronic materials can be used to influence and study the behaviour of cells and proteins in response to electrochemical stimuli. The results demonstrate the ability to direct the molecular conformation of surface-adsorbed proteins, and to use such surfaces to affect cell adhesion, motility, and pro-angiogenic potential. Initial findings point to changes in surface properties (surface energy, chemistry and pH, short-range charge) that affect the conformation of protein molecules, and specific conformation-dependent integrin binding mechanisms that subsequently affect cell behaviour. These results suggest that such devices may serve as a platform to study more complex biological phenomena, and a greater (characterization) understanding should enable more variable and finely-tuned surfaces.

Additionally, there is immense potential to utilize the significant capabilities of lithographic patterning in conjunction with such systems, to enable precise studies on the length-scale of cells that have not been previously possible. In particular, the promise of biologically-benign *Orthogonal* lithographic processing points to many new possibilities that could involve an indefinite number of

lithographic steps.

Further, as polymer systems can take many forms (such as macroporous scaffolds, electro-spun networks, hydrogels, etc.), the potential to develop "smart" cell-culture environments in the increased physiological relevance of three dimensions is very promising, and likely represents the next major area of development in this field of research.

APPENDIX A

MULTICOMPONENT CELL PATTERNING WITH PHOTOLITHOGRAPHY

A.1 Contributions

This project was a collaboration between the Ober and Fischbach groups. Youyong Xu (former postdoctoral research associate in the Ober group) and Yosuke Hoshi (former visiting scientist in the Ober group) developed the chemistry for the photoremovable polymer brush. Yosuke synthesized brush samples for me to use. David Infanger (postdoctoral research associate in the Fischbach group) provided invaluable discussions and expertise in the early design stages of the project to refine the choice of cell lines and relevant antibodies.

A.2 Introduction

Photolithography is a mature field with well-developed techniques for patterning substrates on the micrometre and nanometre scale. There are tremendous opportunities to adapt photolithographic techniques for use in biological research, where they could enable precise patterning of biological molecules (e.g., proteins) and cells. Existing methods for micron-scale (and sub-micron-scale) biological patterning are based on protein patterning by way of techniques such as parylene lift-off masks [124], micro-contact printing [125, 126], nano-imprint

This work went unfinished because of a lack of samples. The M.S. student who was hired to learn the synthesis ultimately never produced any samples, which effectively killed the project.

lithography [127, 128], and biologically-benign lithography (i.e., with *Orthogonal* (nano-imprint) lithography and fluorinated solvents).

Challenges exist with regard to the existing techniques: Parylene lift-off masks can create very clean patterns of a single protein on the length-scale of tens of microns, but lift-off is difficult with micron-sized features or smaller, and patterning multiple protein types is not possible; Micro-contact printing provides the possibility of multicomponent protein patterning, but is dependent upon adhesion of the proteins to the PDMS stamp; Finally, traditional nano-imprint lithography cannot be used for multicomponent protein patterning due to its reliance on harsh chemistries and plasma etching that would damage adsorbed proteins during subsequent patterning steps.

The use of biologically-benign solvents and chemistries in *Orthogonal* processing (or in nano-imprint lithography) presents possibilities for accurate multicomponent protein patterning at any desired length scale. This has been shown by Priscilla Taylor and coworkers for nano-imprint lithography, and is as-yet unproven for *Orthogonal* photolithography (although discussions with Carol Newby have suggested it should be possible). In both of these cases, however, while protein patterning should be achievable, subsequent cell patterning would not be possible without additional work to functionalize the un-patterned regions of the substrate with anti-fouling properties to prevent non-specific adhesion of cells.

The work presented in this Chapter represents an alternative method for multicomponent protein patterning using photolithography, with the added benefit of retaining anti-fouling functionality on the un-patterned regions of the substrate. This strategy utilizes an anti-fouling, photoremovable polymer

brush, which is shown to enable multicomponent antibody patterning on a single surface, and subsequent multicomponent targeted capture of live cells from solution.

Successful completion of this work would represent the first demonstration of a surface capable of selectively capturing multiple cell types from a single solution onto precisely-patterned regions of the substrate. This would enable complex studies of the interactions between multiple cell types, as a function of cell colony size and their separation distance. Studies of this type have are not possible at present, and could provide a powerful tool to the biological community for precise micron-scale experiments in co-cultures.

A.3 Photoremovable Polymer Brush

A photoreactive surface-initiated atom-transfer radical polymerization (SI-ATRP) initiator was deposited onto glass substrates and an anti-fouling polymer brush was prepared on it. The SI-ATRP initiator contains a photo-cleavable group, which adds photoreactivity to the polymer brush itself. The brush was removed in specific regions by UV lithography to enable antibody adsorption in the exposed areas.

A.3.1 SI-ATRP Initiator

The synthesis of the SI-ATRP initiator is shown in Figure A.1. To immobilize the photoreactive initiator on glass substrates, glass microscope slides were treated with a piranha solution (H_2SO_4/H_2O_2 (7:3 v/v)) at 60 °C for 30 min. The sub-

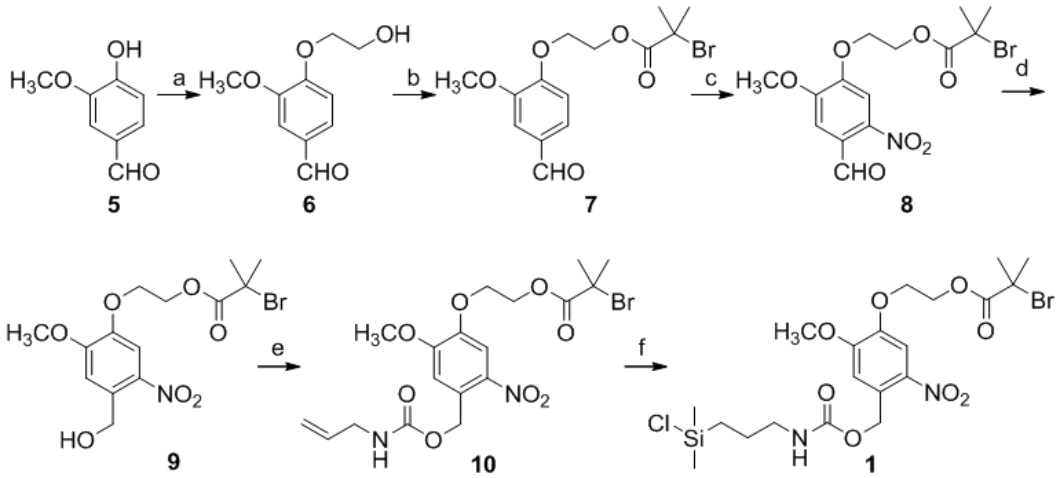

Figure A.1: Preparation of photoreactive SI-ATRP initiator (**1**). (a) $BrCH_2CH_2OH$, K_2CO_3, CH_3CN. (b) 2-Bromoisobutyl bromide, triethylamine, CH_2Cl_2. (c) HNO_3, H_2SO_4, AcOH. (d) $NaBH_4$, THF-H_2O. (e) Allylisocyanate, DMAP, CH_2Cl_2. (f) Dimethylchlorosilane, Pt(C), CH_2Cl_2. Figure prepared by Youyong Xu and reproduced with permission.

strates were washed with water and 2-propanol, blown to dry and dried in an oven (100 °C) for 1 h. After cooling to room temperature under N_2, the substrates were soaked in a solution of toluene solution of *1* (*0.2*M, 0.1 mL), triethylamine (0.03 mL) and anhydrous toluene (10 mL) overnight under N_2. They were then washed with CH_2Cl_2 and water, sonicated in CH_2Cl_2 and soaked in CH_2Cl_2 for 1 day. The substrates were blown dry and used for the polymerization reaction.

A.3.2 Preparation of PSBMA Brush

The PSBMA brush was prepared using a reported procedure [129] with some modification. The initiator-immobilized glass substrate was placed in a flask.

CuBr (28.5 mg, 0.2 mmol) and $CuBr_2$ (4.2 mg, 0.02 mmol) were placed in a round-bottomed flask. SBMA (1.40 g, 5 mmol) and 2,2'-bipyridyl (68.1 mg, 0.44 mmol) were placed in another round-bottomed flask. All flasks were pumped and purged with N_2 3 times. N_2 bubbled MeOH (15 mL) and water (7.5 mL) were added into SBMA/2,2'-bipyridyl, and the resulting solution was added into $CuBr/CuBr_2$. This mixture was stirred vigorously for 5 min and then added into substrate. After 12–30 min, the substrate was taken from the solution, washed with water and soaked in hot water (50 °C) for 30 min. The substrate was washed with water and 2-propanol and blown dry.

The thickness of the resulting brush was measured via ellipsometry to be 23 nm. Under 365 nm UV irradiation for 15 hours in PBS, the thickness is reduced to 1.7 nm. The photoreaction is shown in Figure A.2.

A.4 Antibody Patterning for Live Cell Capture

The goal of the experimental design was to perform targeted capture of human cardiac microvascular endothelial cells (hCMECs) and tumour stem cells (TSCs), in order to study potential pro-angiogenic behaviours induced in the hCMECs by the nearby presence of TSCs. To achieve this, dual antibody patterning was attempted with anti-CD31 (an antibody specific to the CD31 marker of endothelial cells) and anti-SOX2 (an antibody specific to the SOX2 marker of cancer cells).

Patterning was achieved by first exposing the PSBMA brush to 365 nm UV light (at 4 mW/cm^2) for 15 hours in PBS, using a test-pattern shadow mask. This exposed amine groups in the patterned areas, while maintaining the anti-

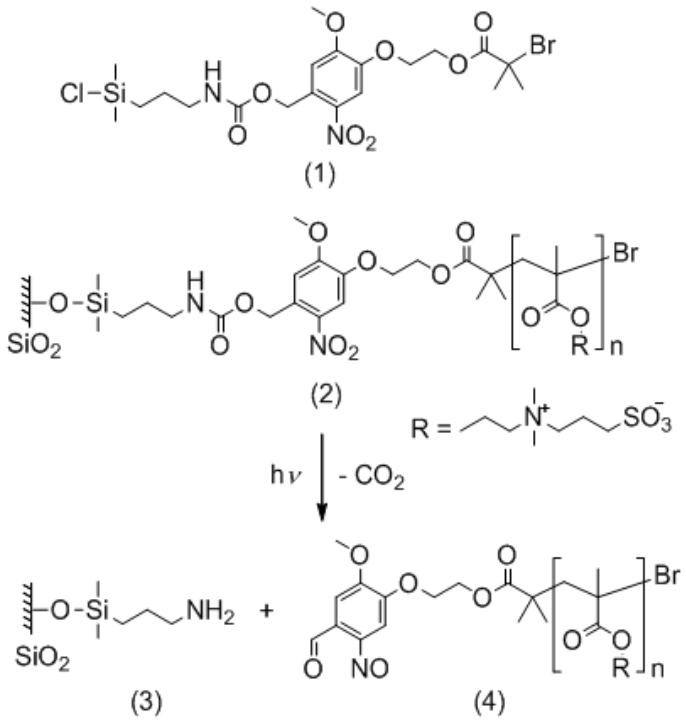

Figure A.2: SI-ATRP initiator and photoreaction of photo-removable polymer brush. Under UV irradiation, the brush is cleaved at the photo-sensitive ortho-nitrobenzyl (ONB) group. Figure prepared by Youyong Xu and reproduced with permission.

fouling brush in unpatterned areas. The substrates were incubated in a solution containing the appropriate antibody and then optionally stained for visualization with a fluorescent secondary antibody. Patterning of both the CD31 and SOX2 antibodies were successful, as shown in Figure A.3.

Subsequent patterning steps could be achieved by repeating the exposure process with a different (or shifted) mask. The first layer of antibodies is kept hydrated in PBS and shielded from UV by the mask, and so is able to maintain its biological function. In this way, dual (protein) patterning on a single substrate was demonstrated by Yosuke Hoshi (Figure A.4).

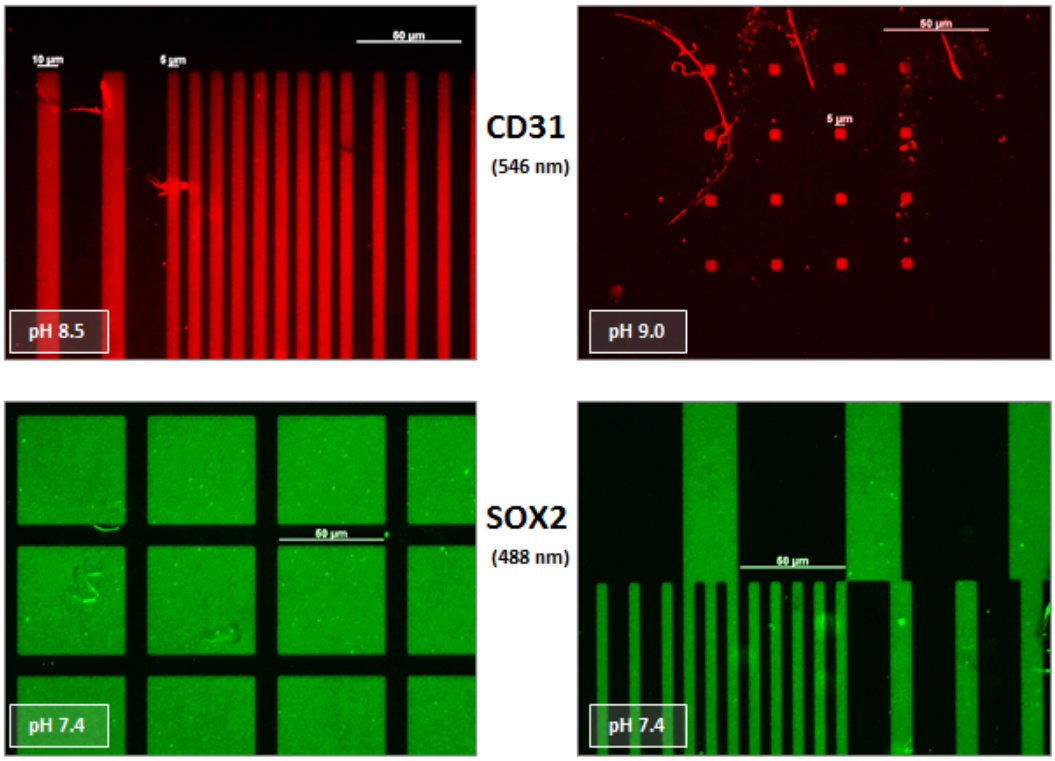

Figure A.3: Fluorescently-stained anti-CD31 (top) and anti-SOX2 (bottom) antibody patterns on glass substrates. Line and square patterns are transfered with good fidelity in a variety of pH conditions. Some scratches are noticeable, likely due to damage during handling which removed the anti-fouling brush from those areas.

After each antibody was patterned onto a separate glass substrate, the substrates were incubated in a solution of the appropriate cell-type (hCMECs for CD31 and TSCs for SOX2) for 24 hours. The samples were then stained with a secondary antibody for the surface-adsorbed antibody (CD31 or SOX2), and a different secondary antibody for the captured cells. A representative image is shown in Figure A.5, demonstrating successful targeted capture of hCMECs from solution onto an array of 100 µm squares.

The patterned anti-CD31 was also demonstrated to successfully capture hu-

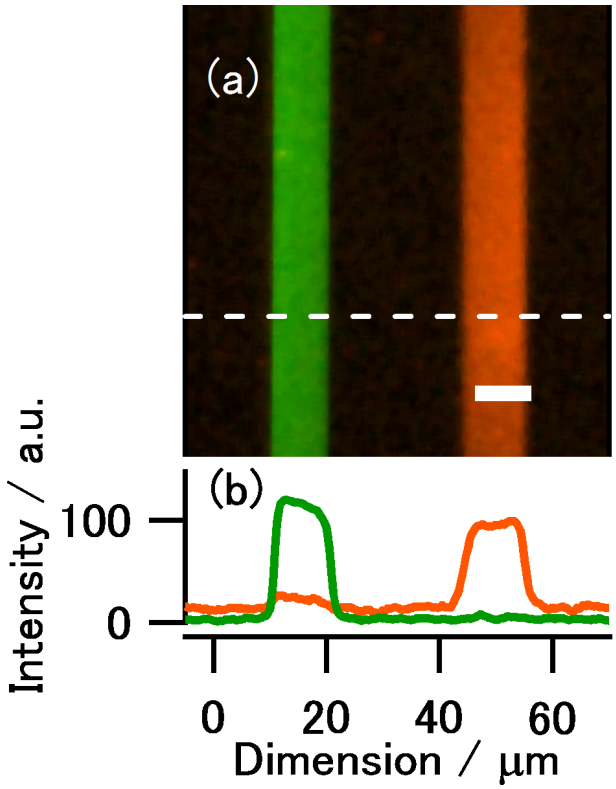

Figure A.4: **(a)** Dual colour fluorescence microscope image of patterned DNP-BSA and anti-human IgG_1 mouse antibody detected with fluorescently-labeled antibodies and **(b)** their intensity profiles on the dotted line. The green line shows the fluorescence intensity of the green fluorophore-labeled anti-DNP rabbit antibody and the orange line shows that of the orange fluorophore-labeled anti-mouse rabbit antibody. Scale bar = 10 μm.

man umbilical vein endothelial cells (hUVECs), as shown in Figure A.6.

While anti-SOX2 patterning was successful, as shown in Figure A.3, surface-capture of TSCs proved difficult. This was in no small part due to the fact that TSCs are a non-adherent cell-type, and grow in suspension. This was a fact I was unaware of when designing the experiment, and added an obvious complication to the goal of capturing cells on the substrate surface.

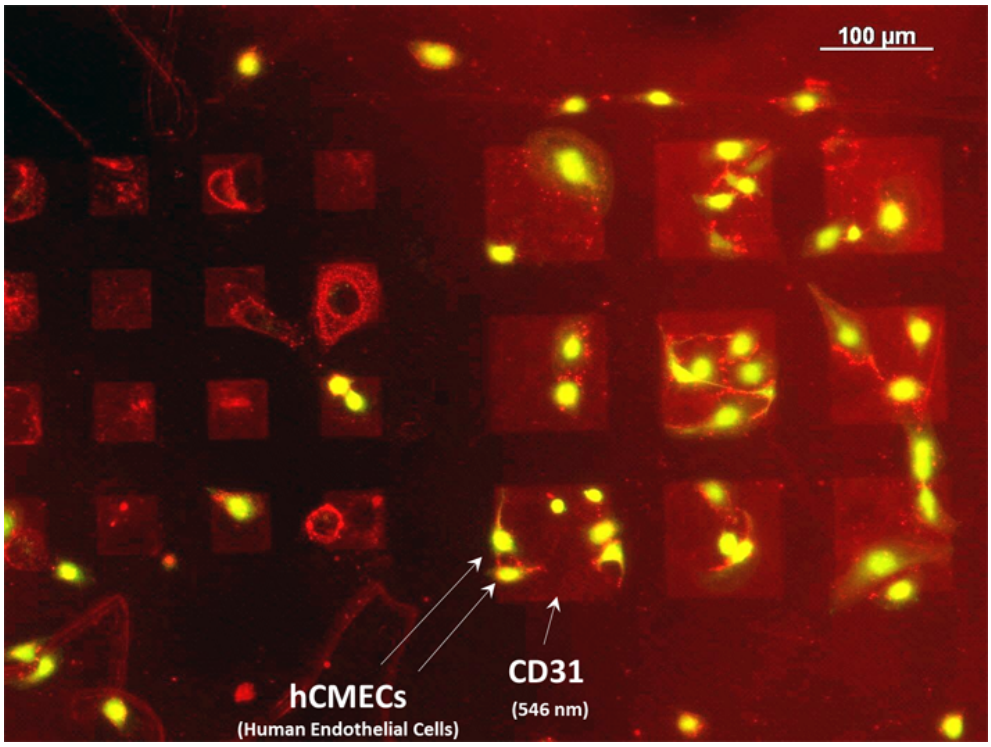

Figure A.5: Fluorescently-stained hCMECs (green) are seen to preferentially adhere to 100 µm square patterns of anti-CD31 (red). Adhesion to the smaller 50 µm patterns is less successful (left), and undesired adhesion to scratches in the anti-fouling brush are seen at top and bottom left.

A.5 Conclusions and Perspectives

The completed experiments outlined above indicate that the goal of multicomponent cell patterning is likely achievable, and it is rather unfortunate that the project was not completed.

The choice of tumour stem cells was not ideal, as they grow in non-adherent conditions and it was difficult to capture reasonable numbers of cells at the surface. Rather than experiment with novel seeding conditions such as extremely high concentrations of cells, or low-speed centrifugation, in order to attempt to

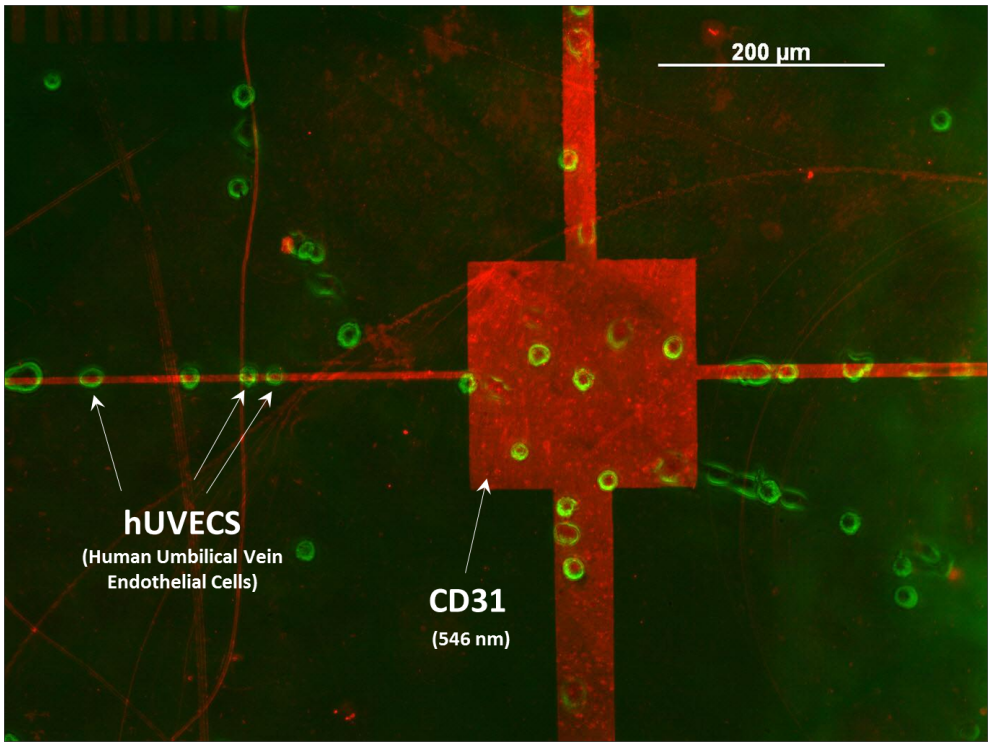

Figure A.6: Fluorescently-stained hUVECs (green) are seen to preferentially adhere to the cross pattern of anti-CD31 (red). An insufficiently high seeding density led to low numbers of adhered cells, and undesired adhesion to scratches in the anti-fouling brush are seen at top left. Some cells are also seen adhering to the brush at lower-right, suggesting that the anti-fouling properties of the brush could be more potent.

capture more cells, it would likely be easier to simply select an adherent tumour cell-line. So long as that cell-line exhibits cell-surface markers for which there exist appropriate antibodies, it should function as desired from a patterning perspective and still offer an interesting biological interaction with endothelial cells to study.

Admittedly, the materials system is far from ideal. The anti-fouling properties of the brush were only borderline-sufficient, with small but finite numbers of cells adhering to some areas of the unexposed brush (Figure A.6). The

brush was also mechanically fragile and was easily scratched during the patterning process, although this may be difficult to fully address (or "fix") from a chemistry perspective. The scratched regions naturally lost their anti-fouling properties, which further led to cell adhesion in undesired regions.

Perhaps the greatest drawback of the current system is the unwieldy and lengthy patterning process. Since the photocleaving reaction needs to take place in an aqueous environment, samples cannot be exposed in an instrument such as the ABM Mask Aligner. This means mask alignment is done by hand, and is necessarily imprecise. While I believe some tricks can be played to achieve precision within 100 µm, this is still a non-starter for precise, directed patterning. My solution was to intentionally design two masks with a gradually-varying relative offset between adjacent patterns, such that no matter what the relative placement of the two masks on the substrate, there would be a high probability that the desired pattern spacings would be found *somewhere* on the substrate.

The second problem is the extremely long exposure time of ~15 hours when using our laboratory UV lamp, due in large part to the apparent low sensitivity of the photoactive group. A higher-power lamp might help mitigate this somewhat, but clearly an exposure time counted in numbers of hours requires serious optimization for to be adapted for more practical usage.

These various drawbacks notwithstanding, I still believe that this system, or an improved/optimized version of it, can achieve live-cell capture of multiple cell types onto precisely-patterned features. I believe this would represent an important contribution to the biological community, as I am unaware of any existing technique or technology that can enable the precisely-controlled multiple cell-type studies that should be possible with this system. An unoptimized sys-

tem could certainly produce results worthy of a high-impact publication, but its utility for others would likely be limited without improvements to the brush chemistry and the patterning process.

APPENDIX B

THIN-FILM DEVICE FABRICATION

B.1 Notes on PEDOT:TOS vs. PEDOT:PSS

The motivation for choosing PEDOT:TOS over the more conventional and popular PEDOT:PSS was somewhat historical in origin. When this work first began (circa 2007), PEDOT:TOS offered higher reported conductivities than PEDOT:PSS in thin-film form, offered better stability in aqueous environments, and also had the benefit of being a vapour-phase technique, enabling the possibility of creating complex conducting architectures in a non-line-of-sight manner.

At present (2012), PEDOT:PSS has advanced to the point that commercially-available PEDOT:PSS (PH-1000, Heraeus) can routinely achieve conductivities in excess of 1000 S/cm with appropriate additives (DBSA, ethylene glycol), a value several times higher than what is achievable with the PEDOT:TOS materials and methods used for this work. Additionally, crosslinking additives such as GOPS can impart remarkable stability to PEDOT:PSS films in aqueous environments, exceeding the stability of PEDOT:TOS films (particularly under the destabilizing conditions of electrochemical oxidation or reduction).

PEDOT:PSS is also substantially easier to process than vapour-phase polymerized PEDOT:TOS – both in terms of the time, effort, and equipment required to fabricate thin films, as well as in terms of the (reproducible) quality of the resulting films. A prime example of the latter is the strong sensitivity of the VPP reaction to the ambient relative humidity. In the absence of a very well-

controlled environment or closed system in which the PEDOT:TOS processing can take place, the rate of the VPP reaction varies substantially from season to season (and even day to day) as the humidity changes, and film quality varies accordingly. Some level of humidity is required to catalyze the polymerization reaction, and so during the dry winter months in Ithaca, water needs to be added to the VPP chamber to simply enable the VPP reaction to proceed.

Additionally, it is insufficient to simply control the relative humidity within the VPP chamber, as the preceding steps of spin coating and transferring the sample into the VPP chamber provide opportunities for airborne moisture to affect film properties. In particular, we observed small crystallites or domains (~5 µm) in PEDOT:TOS films processed in humid conditions. These crystallites have been shown to reduce the conductivity of the resulting film [130]. We hypothesized the source of these domains to be water-induced crystallization that likely occurred during the spin-coating step (as evidenced by the typically radial orientation of the domains). This effect can be somewhat mitigated (although not entirely prevented) with the addition of a high boiling-point solvent such as PGMEA to the Fe(III):TOS precursor solution.

PEDOT:TOS does still hold the advantage over PEDOT:PSS of being able to conformally coat architectures with non-line-of-sight structures (assuming those structures can first be coated with the precursor solution); however, this is perhaps the only remaining feature in its favour.

From a practical (and personal) standpoint, I have recently found it far more reliable (and far less frustrating) to use PEDOT:PSS instead of PEDOT:TOS for any applications that do not require thin conformal coatings (all 2-dimensional applications for me thus far). While PEDOT:TOS was used for all of the early

studies presented here [11, 35, 49], the final study (*Progenitor Cell Adhesion and Secretion*, Chapter 5) was started on PEDOT:TOS, but ultimately completed on PEDOT:PSS due to problems that arose with poor adhesion and poor electrochemical stability of the PEDOT:TOS films.

It is worth noting that the Malliaras group has had recent success with a different PEDOT:TOS protocol reported by Winther-Jensen [45], which uses a *non-hexahydrated* Fe(III):TOS precursor, purchased in-solution. The resulting films are reportedly more stable than those produced with the Fe(III):TOS hexahydrate salt. This new precursor solution is not widely available at present, but can be purchased from some Chinese vendors (when it is in stock).

In the realm of fabricating conducting 3D architectures, PEDOT:TOS was successful used to coat porous poly(lactic-co-glycolic acid) (PLGA) scaffolds with a conductive PEDOT layer, while maintaining the desired open pore structure necessary for cell culture. In this endeavour, PEDOT:PSS may have been less successful than PEDOT:TOS, in part due to its much higher viscosity as compared to the Fe(III):TOS precursor solution, which might fill the pores of the scaffold with excessive amounts of material.

However, with the development of the three-dimensional ice templating technique (Chapter 6) to create 3D porous conducting scaffolds that support cell culture very well, the need to coat PLGA scaffolds may now be obsolete.

B.2 Adsorbing Fn Monolayers on PEDOT:TOS surfaces

We chose PEDOT:TOS as the electrochemically-active material on which to adsorb proteins and culture cells. As described in Section 1.3.1, PEDOT is an electrically and ionically conductive polymer, and shows excellent biocompatibility with a variety of cell types. Additionally, PEDOT's tunable properties as a function of electrochemical oxidation/reduction made it a strong candidate as a substrate material for electrically-active cell culture.

B.2.1 PEDOT Thin-Film Device Fabrication

Devices (with either PEDOT:PSS or PEDOT:TOS) were fabricated on 1″×1″ patterned Indium Tin Oxide (ITO)-glass substrates (Kintec), or on bare glass substrates as required. The ITO stripe was used to ensure the linearity of potential gradients, since conducting polymers change their conductivity upon oxidation/reduction (e.g., applying a potential gradient directly to a conducting polymer film would result in a highly non-linear potential profile, with nearly all of the potential dropped near the reducing electrode).

In device configurations that did not require a gradient (i.e., in the pixel device configuration), bare glass substrates (without ITO) were used to avoid two complications: 1) the strong autofluorescence of ITO in the green wavelength range (under 488 nm excitation); and 2) the additional contact resistance between the ITO and PEDOT films that led to unnecessary voltage drop at that interface.

Substrate Cleaning

Substrates were cleaned according to a standard device-fabrication protocol: They were first cleaned with regular laboratory detergent and water, and then placed in a sonicator for 5 minutes each in subsequent solutions of deionized (DI) water + detergent, followed by DI water. The substrates were then rinsed in a DI water rinse tank under flow for 4 minutes.

Substrate patterning was accomplished throughout this work by masking with the careful application of Scotch tape. Pattern sizes were typically on the order of mm in size, so the use of more complex patterning techniques was unnecessary. The typical pattern was a simple rectangular stripe, roughly 20 mm in width and 8 mm in height. All of the above steps (cleaning and patterning) were performed in a laminar flow hood to reduce surface contamination by airborne particles.

After cleaning and patterning, substrates were placed in a UV-Ozone chamber for 15 minutes to strip any remaining organic surface contaminants, and to decorate the substrate surfaces with -OH groups for better adhesion during spin-coating. After this surface treatment, substrates were coated with either PEDOT:PSS or PEDOT:TOS films, according to the following.

PEDOT:PSS Films

Device fabrication involved depositing and patterning PEDOT:PSS thin films on glass substrates, and subsequently attaching polydimethylsiloxane (PDMS) fluid reservoirs. 20 mL of a PEDOT:PSS aqueous dispersion (Heraeus Clevios™ PH 1000) was mixed with 5 mL of ethylene glycol, 50 µL of dodecylbenzenesul-

fonic acid (DBSA), and 1 wt% of 3-glycidoxypropyltrimethoxysilane (GOPS, as a cross-linker). The resulting dispersion was spin-coated on cleaned glass slides (with tape lift-off masks to pattern the PEDOT:PSS) at 800 rpm for 60 seconds. The films were subsequently baked at 140 °C for 1 hour, and then immersed in phosphate buffered saline (PBS) for several hours to remove excess low molecular weight compounds.

Fe(III):TOS Precursor/Oxidant Layer

PEDOT:TOS thin film fabrication consists of two steps: spin-coating a precursor layer, followed by vapour-phase polymerization of PEDOT. The precursor solution consisted of 0.785 g of Fe(III):TOS hexahydrate (Sigma Aldrich) dissolved into 5 mL of 2-propanol, with 32.1 µL of anhydrous pyridine (Sigma Aldrich, as a base inhibitor) and 500 µL of propylene glycol methyl ether acetate (PGMEA, Sigma Aldrich, as a high boiling point solvent). The inclusion of the PGMEA was introduced to mitigate water-induced crystallization of the Fe(III):TOS film during processing, which resulted in the presence of crystallites in the final PEDOT:TOS film.

The Fe(III):TOS precursor solution was spin-coated on the cleaned substrates at 3000 RPM for 60 s. The films were then baked on a hotplate at 140 °C for 120 s to evaporate any remaining solvents.

Vapour-Phase Polymerization of PEDOT:TOS

PEDOT:TOS is polymerized by vapour-phase condensation of EDOT monomers onto a thin film of an oxidizing species (Fe(III):TOS). The oxidant catalyzes the

polymerization reaction, while a base inhibitor (pyridine) retards the rate of the reaction to allow better film-formation.

The Fe(III):TOS-coated substrates were placed in a ReynoldsTech vapour-phase polymerization (VPP) chamber. The substrates were heated to 35 °C and a crucible containing EDOT monomer solution was heated to 80 °C (as determined by a conductivity optimization study). A membrane pump supplied a vacuum of roughly 100 torr, and the substrates were left in the VPP chamber for 15 minutes.

After polymerization, the transparent yellow Fe(III):TOS films turn transparent blue, indicating the formation of PEDOT. Polymerized films were baked in an oven at 50 °C for 1 hour to allow the films to anneal. After cooling to room temperature, the Scotch tape masks were removed from the substrates, and the substrates were immersed in ethanol for 10 minutes, refreshing the solvent once at 5 minutes, to dissolve remaining Fe salts.

For pixel configuration devices, a dividing line was scribed with a diamond scribe vertically through the middle of the PEDOT (and ITO) stripe, separating the stripe into two unconnected pixels.

Polydimethylsiloxane Reservoirs

Device fabrication is completed by attaching an appropriate fluid reservoir cut from polydimethylsiloxane (PDMS). The PDMS (Sylgard 184) was cast at a ratio of 10:1 base:cross-linker, and cured for 1 h at 60 °C. Reservoirs were cut by hand (razor blade and X-Acto knife), and placed in a UV-Ozone chamber for 10 minutes prior to being attached to the glass substrates.

B.2.2 Adsorbing Fn Monolayers onto Devices

Fn Coating Solution

Fn was dissolved at a concentration of 30 µg/ml in either cell culture media (with or without serum) or in phosphate buffered saline (PBS), for coating devices. In the case of FRET-labeled Fn (Fn-DA) devices, for measuring conformation, the Fn solution contained 10% Fn-DA and 90% unlabeled human plasma Fn.

APPENDIX C

FRET MEASUREMENTS AND ANALYSIS

C.1 Measuring Protein Conformation via FRET

The molecular conformation of surface-adsorbed Fn is assessed via the "molecular ruler" mechanism provided by FRET, as described in Section 1.5.1. Experimentally, this measurement was performed on a (Zeiss LSM 710) confocal microscope, capable of exciting the donor fluorophore via a 488 nm Argon laser while simultaneously measuring the total emission intensity of the donor and acceptor fluorophores in their respective wavelength windows ($\Delta\lambda_{Don} = 514 - 526\,\text{nm},\ \Delta\lambda_{Acc} = 566 - 578\,\text{nm}$).

Images were acquired through a 25× water-immersion objective in 16-bit colour depth (necessary for the low-intensity signal from a monolayer of protein), at a size of 512×512 px^2 (340×340 µm^2) and a pixel dwell-time of 2.55 µm/px.

FRET ratio ($I_{Acceptor}/I_{Donor}$) was calculated for each field of view by integrating the absolute emission of each fluorophore after background subtraction (from a control device); i.e.,

$$\begin{aligned} I_{Donor} &= \int_{514}^{526} |I_{Fn} - I_{Control}|\, d\lambda, \\ I_{Acceptor} &= \int_{566}^{578} |I_{Fn} - I_{Control}|\, d\lambda, \text{ and} \\ \text{FRET} &= I_{Acceptor}/I_{Donor}. \end{aligned}$$

Analysis was performed in MATLAB, with details outlined in Section C.1.1.

C.1.1 Notes on FRET Analysis

Confocal microscope images were acquired in 16-bit colour (greyscale) depth, at 512×512 px resolution, in a two-channel stack. The two channels were exported into individual 16-bit TIFF images via Zeiss' Zen Software, which were then read directly into MATLAB for analysis.

Briefly, a FRET map was generated for each donor-acceptor image pair by pixel-wise division of the acceptor image by the donor image (after application of a smoothing filter and omission of clipping pixels). This FRET image could then be colourized with a heat map for visualization, and analyzed quantitatively with respect to the values of the FRET pixels. Typical quantities that were calculated included: the mean, mode, and standard deviation of the FRET distribution (histogram). Further details of the analysis method and the source code are contained in Section C.2 of Appendix C.

C.1.2 Potential Sources of Error in FRET Measurements

There are a variety of potential sources of error in the FRET measurements described above, originating from both the device architecture itself, as well as from the instrument used to measure the FRET signal. The sources of error encountered in this work are outlined below, along with the strategies used to account for them.

Autofluorescence and background signal from ITO/PEDOT:TOS

The 100 nm thick indium tin oxide layer in the device sandwich was found to autofluoresce strongly in the green wavelength range, under excitation from a 488 nm laser. This presents a significant challenge when measuring the FRET signal (or any fluorescent signal) from single monolayers of adsorbed Fn, as the (background) autofluorescence signal intensity is significantly stronger than the fluorescent emission from either the donor or acceptor fluorophores.

Thankfully, since the ITO layer is separated from the Fn-DA by a 100 nm-thick PEDOT film, there is no concern of FRET (energy transfer) occurring between the ITO and the acceptor fluorophores. Thus, only the background autofluorescence signal from the ITO must be accounted for.

Ideally, this problem can be avoided entirely by not using ITO in the device architecture, or by replacing it with a non-fluorescent conductor. Avoiding the use of the ITO film is possible in the pixel device configuration, however it is necessary in the gradient device configuration in order to ensure the linearity of the voltage gradient. It may be possible to replace the ITO with a non-fluorescent transparent conductor in this configuration (i.e., a thin Au film), however this was not tried.

To measure the autoflourescent signal for background subtraction, a modified device configuration was used, with two adjacent PDMS wells that both spanned the width of the gradient device. One well was filled with Fn-DA in PBS, while the other was filled with just PBS. The PBS-only well served as a control to from which the autofluorescent emission of the ITO was measured as a function of voltage with lambda scans. These background emission spectra

were then subtracted from the full emission spectra measured from the Fn-DA well to give the true FRET signal from the fluorophores.

Differential energy transfer from fluorophores to PEDOT:TOS

PEDOT:TOS is an optoelectronically active material, with an absorbance spectrum that varies with its redox state (the origin of its electrochromic behaviour). This raises the concern that the donor and acceptor fluorophores could individually (and differentially) transfer energy to the underlying PEDOT layer in a parasitic FRET process (fluorescence quenching [131]) that would affect the measured FRET intensity ratio.

By considering the PEDOT thin-film absorbance spectrum as a function of redox voltage [132], we can show that the effect is minimal and has very little effect on the overall FRET trend we observed. As shown in Figure C.1, such additional energy transfer (if any) would be restricted to potentials ranging from $-0.65\,\mathrm{V}$ to $-1\,\mathrm{V}$, i.e., when PEDOT is slightly absorbing in our wavelength range of interest (see Figure C.1). This would therefore have very little effect on our FRET trend, which shows the greatest variation (FRET decrease) occurring from $1\,\mathrm{V}$ to $0\,\mathrm{V}$, i.e., when PEDOT is *not* absorbing, while it is roughly constant from $0\,\mathrm{V}$ to $-1\,\mathrm{V}$.

Photomultiplier Tube (PMT) Detector Sensitivity

The Zeiss LSM 710 Confocal Microscope used to measure FRET has two photomultiplier tubes (PMTs) for simultaneous detection of donor and acceptor emissions. To achieve simultaneous imaging, a beam-splitter is used to split the

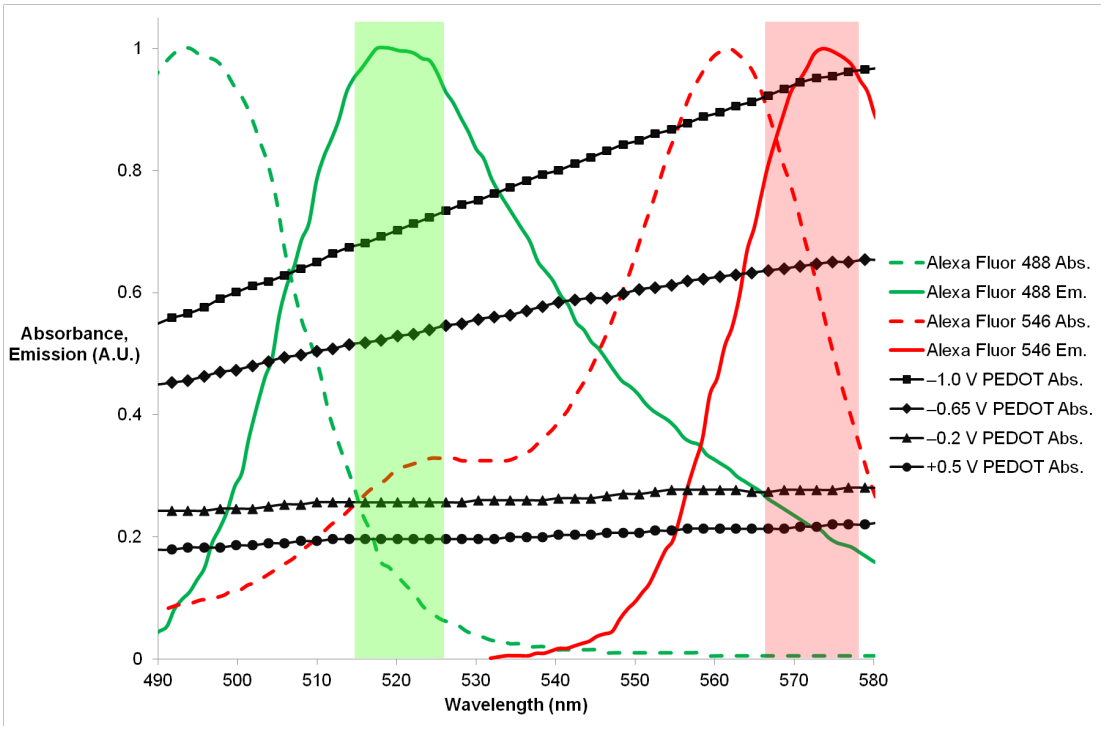

Figure C.1: Absorbance and emission spectra of Donor and Acceptor fluorophores (coloured, dashed lines), overlayed with absorbance spectra of PEDOT at various potentials (from [132]). The green and red rectangles represent the donor and acceptor wavelength windows used to calculate FRET. [11]

incoming light to the two PMTs. Either a difference in PMT sensitivity, or a deviation from a 50/50 split in the beamsplitter, would result in an artifact in the measured FRET ratio. One or both of these may occur, but for the purposes of this study only the total effect is important, and not what its origins are.

This effect is measured fairly easily by measuring the emission from single-labelled Fn molecules, in solution (to avoid photobleaching), successively in PMT1 and PMT2. By repeating this measurement for both the donor and acceptor fluorophores, the difference in PMT sensitivity (or beam-splitter unevenness) is easily measured for a given wavelength range and a given objective lens.

This artificial change in measured FRET ratio can then be normalized out of the FRET ratio calculations with a simple multiplicative factor. At present (August 2012), PMT2 (the acceptor channel) is *more* sensitive than PMT1 (the donor channel) by a factor of roughly 2.2 – 2.4; however, repairs were performed on one (or both) of the microscope's PMTs since my last calibration, so this value may have changed since then.

It should be noted that the Zeiss software does not allow (for some inexplicable reason) for the obvious calibration measurement: to measure FRET from the Donor (Acceptor) fluorophore with PMT1 (PMT2), followed by a reverse measurement of the Acceptor (Donor) fluorophore with PMT1 (PMT2). Additionally, it is prudent to make the calibration measurements described above on a semi-frequent basis (or even during every FRET imaging session), to ensure that internal drift or changes to the microscope setup (due to maintenance, etc.) have not altered the effective PMT sensitivity ratio.

C.2 FRET Analysis in MATLAB

The following code was modified from Delphine Gourdon's BSFRET_V17.m matlab program to batch-process large numbers of FRET images.

```
function BSFRETv17_alwin_fullTIFFs
% ;..;d HARRO WORLD!

pmt_ratio = 2.7;        % Intensity Ratio of PMT2/PMT1 (Acc/Don)
use_time_dependent_pmt_ratio = 0;
globalThresh = 70;
upper_thresh = 65530;   % Upper intensity threshold to discard data

directory = uigetdir(pwd, 'Select Directory with TIFF ...
    channel-images:');
cd(directory);
```

```
mkdir ./dat;   % Output directory for data files

fileindex = dir('PBS_PLG*tif');
% filename_base = ...
    fileindex(1).name(1:findstr(fileindex(1).name,'.')-4);  % ...
    Base name of first file
% t0_fileindex = dir(['../' filename_base '.lsm']); ...
                            % Corresponding LSM file
% t0 = datenum(t0_fileindex(1).date) * 24 * 60; ...
                                % t0 timestamp of LSM file

meanir = zeros(1,length(fileindex));
maxdo = meanir;
maxac = meanir;
meanac = meanir;

% DC and Threshold constants
dc1 = 0; dcSD1 = 0;
dc2 = 0; dcSD2 = 0;

accThresh = globalThresh; donThresh = globalThresh;
upLimit = 1.1; lowLimit = 0.3;
limits = [lowLimit upLimit];

mkdir(['./t' num2str(globalThresh)]);

%number of bins in ir histogram
z = 90; binsize = (upLimit-lowLimit)/z;
%percentage data below ??M input
M0 = 1.02; M1 = 0.76; M2 = 0.68; M4 = 0.54;

% dc_LSMfiles = dir(['../_dc_*.lsm']);
% t0 = datenum(dc_LSMfiles(1).date) * 24 * 60;

for filecount = 1:(length(fileindex))
    tif_file = fileindex(filecount).name;
    tif_data = imread(tif_file);   % ACC, DON, and blank channels
    ac1 = tif_data(:,:,1);   % ACCEPTOR
    do1 = tif_data(:,:,2);   % DONOR

    filename_base = tif_file(1:findstr(tif_file,'.')-1);  % ...
        Remove filename suffix
    %filename_base = ...
        filename_base(findstr(tif_file,'_')+1:end);  % Remove ...
        filename prefix

    %convert to double precision
    ac1 = double(ac1); do1 = double(do1);

    %averaging mask
    ac1 = colfilt(ac1,[4 4],'sliding',@mean); do1 = ...
        colfilt(do1,[4 4],'sliding',@mean);
```

```
55
56      %Remove dark current offset
57      ac1 = ac1 - (dc1 + 3*dcSD1); do1 = do1 - (dc2 + 3*dcSD2);
58
59      %compensate VPMT1=650V instead of 600V
60      %ac1 = ac1*600/650;
61
62      %compensate for 50_50BS intensity attenuation
63      if use_time_dependent_pmt_ratio     % use fit equation for ...
            DC data
64          curr_LSMfile = dir(['./' filename_base '.lsm']);
65          t = datenum(curr_LSMfile(1).date) * 24 * 60;
66          dt = t-t0;
67          pmt_ratio = (9.8e-011*dt^5 - 1.2e-008*dt^4 - ...
                5.8e-008*dt^3 + 6.6e-005*dt^2 - 0.0033*dt + 0.55)*1.2;
68      end
69      do1 = do1*pmt_ratio;
70
71      %eliminate dim pixels
72      for x = 1:size(ac1,1)
73          for y = 1:size(ac1,2)
74              if ac1(x,y) ≤ accThresh || do1(x,y) ≤ ...
                    donThresh*pmt_ratio || ac1(x,y) ≥ upper_thresh ...
                    || do1(x,y) ≥ upper_thresh
75                  ac1(x,y) = 0; do1(x,y) = 0;
76              end
77          end
78      end
79
80      %fret calculation
81      ir = ac1./do1;
82      ac_mean = mean(ac1(:));     ac_std = std(ac1(:));
83      do_mean = mean(do1(:));     do_std = std(do1(:));
84
85      %Convert matrix to image and save to disk
86      limits = [lowLimit upLimit];
87      irImage = mat2gray(ir, limits);
88
89      greyscale_filename = strcat('./t', num2str(accThresh),'/', ...
            filename_base, '_greyscale.tif');
90      imwrite(irImage,greyscale_filename,'tif','compression','none');
91
92      %Remove un-realistic ir values and NaNs
93      M0count = 0; M1count = 0; M2count = 0; M4count = 0;
94      for xx = 1:size(ir,1)
95          for yy = 1:size(ir,2)
96              if isnan(ir(xx,yy)) || ir(xx,yy) ≤ lowLimit || ...
                    ir(xx,yy) ≥ upLimit
97                  ir(xx,yy) = 0;
98              end
99              if ir(xx,yy) ≤ M4 && ir(xx,yy) > 0
100                 M4count = M4count + 1;
```

```
            end
            if ir(xx,yy) ≤ M0 && ir(xx,yy) > 0
                M0count = M0count + 1;
            end
            if ir(xx,yy) ≤ M2 && ir(xx,yy) > 0
                M2count = M2count + 1;
            end
            if ir(xx,yy) ≤ M1 && ir(xx,yy) > 0
                M1count = M1count + 1;
            end
        end
    end

    %determine number of ir pixels and ir statistics
    avgirArray=nonzeros(ir);
    avgirsize=size(avgirArray);
    avgirmean=mean(avgirArray);
    avgirstd=std(avgirArray);
    percentbelowM2 = M2count/(avgirsize(1,1))*100;
    percentbelowM1 = M1count/(avgirsize(1,1))*100;
    percentbelowM4 = M4count/(avgirsize(1,1))*100;
    percentbelowM0 = M0count/(avgirsize(1,1))*100;
    per5 = prctile(avgirArray,5);
    per95 = prctile(avgirArray,95);

    %generate a histogram for ir mode determination and display
    bins = lowLimit:binsize:upLimit;
    [histCounts, histX] = hist(avgirArray,bins);
    [C,I] = max(histCounts);
    modeReal = histX(I);  %Calculate mode from histogram data
    histCounts = histCounts/C;  %normalize the image to scale ...
        from 0.0-1.0

    %Plotting
    subplot(3,1,[1 2]); imagesc(ir, limits);
    axis off; axis square;
    colorbar('horiz');
    set(gca, 'FontName', 'Times New Roman', 'FontSize', 12);
    subplot(3, 1, [3]); bar(histX, histCounts);
    xlabel('intensity ratio (acceptor/donor)', 'FontName', ...
        'Times New Roman', 'FontSize', 12);
    ylabel('events', 'FontName', 'Times New Roman', 'FontSize', ...
        12);
    set(gca, 'FontName', 'Times New Roman', 'FontSize', 12);
    axis([lowLimit upLimit 0 1]);

    %save the final data as a .tiff
    saveas(figure(1), strcat('./t',num2str(accThresh),'/', ...
        filename_base,'_fig'), 'tif');

    %output data for further analysis into a text file
    output = [ avgirmean modeReal avgirstd avgirsize(1,1) ...
```

```
            percentbelowM4 percentbelowM2 percentbelowM1 ...
            percentbelowM0 per5 per95 ac_mean ac_std do_mean do_std ...
            pmt_ratio];
149     out_filename = strcat('./dat/',filename_base, '_data.out');
150     save(out_filename, 'output', '-ASCII', '-tabs');
151     %output histogram data
152     output = [ histX' histCounts' ];
153     out_filename = strcat('./dat/',filename_base, '.hist');
154     save(out_filename, 'output', '-ASCII', '-tabs');
155
156     fprintf('%s ...\t\t(%d/%d)\n', tif_file, filecount, ...
            length(fileindex));
157     meanir(filecount) = avgirmean;
158     maxdo(filecount) = max(do1(:));
159     maxac(filecount) = max(ac1(:));
160     meanac(filecount) = mean(nonzeros(ac1));
161 end
162 fprintf('\nDone!\n');
163
164 fprintf('avg IR = %.3g +/- %.3g\n', mean(meanir), std(meanir));
165 fprintf('max DO = %.3g +/- %.3g\n', mean(maxdo), std(maxdo));
166 fprintf('max AC = %.3g +/- %.3g\n', mean(maxac), std(maxac));
167 fprintf('avg AC = %.3g +/- %.3g\n', mean(meanac), std(meanac));
```

APPENDIX D

NEAR EDGE X-RAY ABSORPTION FINE STRUCTURE (NEXAFS)

D.1 Characterization of PEDOT:PSS Films

Oxidized (+1 V) and reduced (−1 V) PEDOT:PSS thin films were prepared and and scanned by Carol Newby at the Brookhaven National Laboratory synchrotron. The goal was to attempt to characterize the chemical changes that take place under electrochemical oxidation/reduction in the PEDOT:PSS films. Both carbon and oxygen peaks were recorded. While the carbon peaks showed no differences for the oxidized and reduced samples, differences *were* observed in the oxygen peaks, as shown in Figure D.1. No angular dependence was observed for either condition.

Further interpretation of these results is required, and additional scans (perhaps of the sulfur peaks) could yield useful information about the surface chemistry.

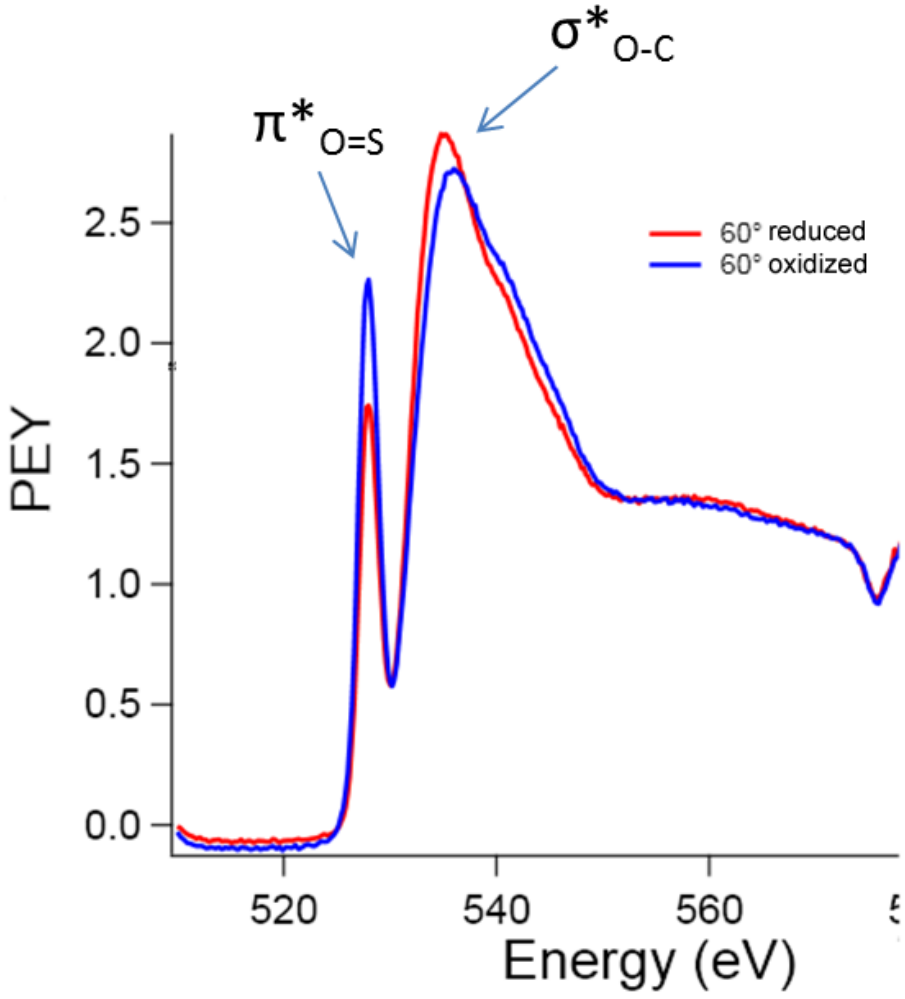

Figure D.1: Oxygen peaks measured by NEXAFS from an oxidized and a reduced PEDOT:PSS film, at an incident angle of 60°.

BIBLIOGRAPHY

1. *Bioelectronics* (eds I. Willner & E. Katz) (Wiley-VCH Verlag GmbH & Co. KGaA, Weinheim, FRG, 2005).

2. T. M. Brown, J. S. Kim, R. H. Friend, F. Cacialli, R. Daik & W. J. Feast. "Built-in field electroabsorption spectroscopy of polymer light-emitting diodes incorporating a doped poly(3,4-ethylene dioxythiophene) hole injection layer." *Applied Physics Letters* **75,** 1679 (1999).

3. J. T. Mabeck & G. G. Malliaras. "Chemical and biological sensors based on organic thin-film transistors." *Analytical and Bioanalytical Chemistry* **384,** 343–53 (2006).

4. D. J. Macaya, M. Nikolou, S. Takamatsu, J. T. Mabeck, R. M. Owens & G. G. Malliaras. "Simple glucose sensors with micromolar sensitivity based on organic electrochemical transistors." *Sensors and Actuators B: Chemical* **123,** 374–378 (2007).

5. A. Elschner & W. Lövenich. "Solution-deposited PEDOT for transparent conductive applications." *MRS Bulletin* **36,** 794–798 (2011).

6. S. Timpanaro, M. Kemerink, F. Touwslager, M. De Kok & S. Schrader. "Morphology and conductivity of PEDOT/PSS films studied by scanningtunneling microscopy." *Chemical Physics Letters* **394,** 339–343 (2004).

7. J. Ouyang, Q. Xu, C.-W. Chu, Y. Yang, G. Li & J. Shinar. "On the mechanism of conductivity enhancement in poly(3,4-ethylenedioxythiophene): poly(styrene sulfonate) film through solvent treatment." *Polymer* **45,** 8443–8450 (2004).

8. Y. Xia & J. Ouyang. "Salt-Induced Charge Screening and Significant Conductivity Enhancement of Conducting Poly(3,4-ethylenedioxythiophene): Poly(styrenesulfonate)." *Macromolecules* **42,** 4141–4147 (2009).

9. G. Malliaras & R. Friend. "An Organic Electronics Primer." *Physics Today* **58,** 53 (2005).

10. A. O. Patil, A. J. Heeger & F. Wudl. "Optical properties of conducting polymers." *Chemical Reviews* **88,** 183–200 (1988).

11. A. M. D. Wan, R. M. Schur, C. K. Ober, C. Fischbach, D. Gourdon & G. G. Malliaras. "Electrical control of protein conformation." *Advanced Materials* **24,** 2501–2505 (2012).

12. K. Aasmundtveit, E. Samuelsen, O Inganäs, L. Pettersson, T Johansson & S Ferrer. "Structural aspects of electrochemical doping and dedoping of poly(3,4-ethylenedioxythiophene)." *Synthetic Metals* **113,** 93–97 (2000).

13. K. Dumpert. "Embryotoxic effects of environmental chemicals: Tests with the South African clawed toad (Xenopus laevis)." *Ecotoxicology and Environmental Safety* **13,** 324–338 (1987).

14. E Cukierman, R Pankov, D. R. Stevens & K. M. Yamada. "Taking cell-matrix adhesions to the third dimension." *Science (New York, N.Y.)* **294,** 1708–12 (2001).

15. R. O. Hynes. "Integrins: Bidirectional, Allosteric Signaling Machines." *Cell* **110,** 673–687 (2002).

16. Y. Mao & J. E. Schwarzbauer. "Fibronectin fibrillogenesis, a cell-mediated matrix assembly process." *Matrix Biology: Journal of the International Society for Matrix Biology* **24,** 389–99 (2005).

17. A. J. Garcia, M. D. Vega & D. Boettiger. "Modulation of Cell Proliferation and Differentiation through Substrate-dependent Changes in Fibronectin Conformation." *Mol. Biol. Cell* **10,** 785–798 (1999).

18. V. Vogel & M. Sheetz. "Local force and geometry sensing regulate cell functions." *Nature Reviews: Molecular Cell Biology* **7,** 265–75 (2006).

19. M. L. Smith, D. Gourdon, W. C. Little, K. E. Kubow, R. A. Eguiluz, S. Luna-Morris & V. Vogel. "Force-Induced Unfolding of Fibronectin in the Extracellular Matrix of Living Cells." *PLoS Biol* **5,** e268 (2007).

20. R. Pankov & K. M. Yamada. "Fibronectin at a glance." *The Journal of Cell Science* **115,** 3861–3863 (2002).

21. R. O. Hynes & K. M. Yamada. "Fibronectins: multifunctional modular glycoproteins." *The Journal of Cell Biology* **95,** 369–377 (1982).

22. E. Klotzsch, M. L. Smith, K. E. Kubow, S. Muntwyler, W. C. Little, F. Beyeler, D. Gourdon, B. J. Nelson & V. Vogel. "Fibronectin forms the most extensible biological fibers displaying switchable force-exposed cryptic binding sites." *Proceedings of the National Academy of Sciences* **106,** 18267–18272 (2009).

23. H. Erickson. "Fibronectin molecule visualized in electron microscopy: a long, thin, flexible strand." *The Journal of Cell Biology* **91,** 673–678 (1981).

24. M. Rocco, M. Carson, R. Hantgan, J. McDonagh & J. Hermans. "Dependence of the shape of the plasma fibronectin molecule on solvent composition. Ionic strength and glycerol content." *J. Biol. Chem.* **258,** 14545–14549 (1983).

25. E. Puklin-Faucher, M. Gao, K. Schulten & V. Vogel. "How the headpiece hinge angle is opened: New insights into the dynamics of integrin activation." *The Journal of Cell Biology* **175,** 349–60 (2006).

26. S. De, O. Razorenova, N. P. McCabe, T. O'Toole, J. Qin & T. V. Byzova. "VEGF-integrin interplay controls tumor growth and vascularization." *Proceedings of the National Academy of Sciences of the United States of America* **102,** 7589–94 (2005).

27. S. Miyamoto, B.-Z. Kathz, R. M. LaFrenie & K. M. Yamada. "Fibronectin and Integrins in Cell Adhesion, Signaling, and Morphogenesis". *Annals of the New York Academy of Sciences* **857,** 119–129 (1998).

28. R. Kalluri & M. Zeisberg. "Fibroblasts in cancer." *Nature Reviews: Cancer* **6,** 392–401 (2006).

29. N. A. Bhowmick, E. G. Neilson & H. L. Moses. "Stromal fibroblasts in cancer initiation and progression." *Nature* **432,** 332–7 (2004).

30. P. Cornelius, O. A. MacDougald & M. D. Lane. "Regulation of adipocyte development." *Annual Review of Nutrition* **14,** 99–129 (1994).

31. T. Förster. "Zwischenmolekulare Energiewanderung und Fluoreszenz." *Annalen der Physik* **437,** 55–75 (1948).

32. T. Wilson. *Confocal Microscopy* 426 (Academic Press, 1990).

33. M. Born, E. Wolf & A. B. Bhatia. *Principles of Optics: Electromagnetic Theory of Propagation, Interference and Diffraction of Light* (Cambridge University Press, 1999).

34. A. Lipson, S. G. Lipson & H. Lipson. *Optical Physics* (Cambridge University Press, 2010).

35. A. M. D. Wan, D. J. Brooks, A. Gumus, C. Fischbach & G. G. Malliaras. "Electrical control of cell density gradients on a conducting polymer surface." *Chemical Communications,* 5278–80 (2009).

36. D. J. Pennisi & T. Mikawa. "Normal patterning of the coronary capillary plexus is dependent on the correct transmural gradient of FGF expression in the myocardium." *Developmental Biology* **279,** 378–90 (2005).

37. L. Liu, B. D. Ratner, E. H. Sage & S. Jiang. "Endothelial cell migration on surface-density gradients of fibronectin, VEGF, or both proteins." *Langmuir* **23,** 11168–73 (2007).

38. C. M. Nelson, W. F. Liu & C. S. Chen. "Manipulation of cell-cell adhesion using bowtie-shaped microwells." *Methods in Molecular Biology (Clifton, N.J.)* **370,** 1–10 (2007).

39. M. M. Rosenkilde & T. W. Schwartz. "The chemokine system – a major regulator of angiogenesis in health and disease." *APMIS : Acta Pathologica, Microbiologica, et Immunologica Scandinavica* **112,** 481–95 (2004).

40. C.-L. E. Helm, M. E. Fleury, A. H. Zisch, F. Boschetti & M. A. Swartz. "Synergy between interstitial flow and VEGF directs capillary morphogenesis in vitro through a gradient amplification mechanism." *Proceedings of the National Academy of Sciences of the United States of America* **102,** 15779–84 (2005).

41. S.-Y. Cheng, S. Heilman, M. Wasserman, S. Archer, M. L. Shuler & M. Wu. "A hydrogel-based microfluidic device for the studies of directed cell migration." *Lab on a chip* **7,** 763–9 (2007).

42. J. Y. Wong, R. Langer & D. E. Ingber. "Electrically Conducting Polymers can Noninvasively Control the Shape and Growth of Mammalian Cells". *Proceedings of the National Academy of Sciences* **91,** 3201–3204 (1994).

43. C. E. Schmidt, V. R. Shastri, J. P. Vacanti & R Langer. "Stimulation of neurite outgrowth using an electrically conducting polymer." *Proceedings of the National Academy of Sciences* **94,** 8948–8953 (1997).

44. C. Saltó, E. Saindon, M. Bolin, A. Kanciurzewska, M. Fahlman, E. W. H. Jager, P. Tengvall, E. Arenas & M. Berggren. "Control of neural stem cell adhesion and density by an electronic polymer surface switch." *Langmuir : the ACS journal of surfaces and colloids* **24,** 14133–8 (2008).

45. B. Winther-Jensen & K. West. "Vapor-Phase Polymerization of 3,4-Ethylenedioxythiophene: A Route to Highly Conducting Polymer Surface Layers." *Macromolecules* **37,** 4538–4543 (2004).

46. J. Gustafsson, B. Liedberg & O. Inganas. "In situ spectroscopic investigations of electrochromism and ion transport in a poly (3,4-ethylenedioxythiophene) electrode in a solid state electrochemical cell." *Solid State Ionics* **69,** 145–152 (1994).

47. K. M. Yamada, K. Olden & I. Pastan. "Transformation-Sensitive Cell Surface Protein: Isolation, Characterization, and Role in Cellular Morphology and Adhesion." *Annals of the New York Academy of Sciences* **312,** 256–277 (1978).

48. S. Y. Yang, J. A. Defranco, Y. A. Sylvester, T. J. Gobert, D. J. Macaya, R. M. Owens & G. G. Malliaras. "Integration of a surface-directed microfluidic system with an organic electrochemical transistor array for multi-analyte biosensors." *Lab on a Chip* **9,** 704–8 (2009).

49. A. Gumus, J. P. Califano, A. M. D. Wan, J. Huynh, C. A. Reinhart-King & G. G. Malliaras. "Control of cell migration using a conducting polymer device." *Soft Matter* **6,** 5138 (2010).

50. P. A. DiMilla, K. Barbee & D. A. Lauffenburger. "Mathematical model for the effects of adhesion and mechanics on cell migration speed." *Biophysical Journal* **60,** 15–37 (1991).

51. D. A. Lauffenburger & A. F. Horwitz. "Cell migration: a physically integrated molecular process." *Cell* **84,** 359–69 (1996).

52. G. Chan & D. J. Mooney. "New materials for tissue engineering: towards greater control over the biological response." *Trends in Biotechnology* **26,** 382–92 (2008).

53. B. K. Brandley & R. L. Schnaar. "Tumor cell haptotaxis on covalently immobilized linear and exponential gradients of a cell adhesion peptide." *Developmental Biology* **135,** 74–86 (1989).

54. S. A. DeLong, J. J. Moon & J. L. West. "Covalently immobilized gradients of bFGF on hydrogel scaffolds for directed cell migration." *Biomaterials* **26,** 3227–34 (2005).

55. C. M. Lo, H. B. Wang, M Dembo & Y. L. Wang. "Cell movement is guided by the rigidity of the substrate." *Biophysical Journal* **79,** 144–52 (2000).

56. S. R. Peyton, C. M. Ghajar, C. B. Khatiwala & A. J. Putnam. "The emergence of ECM mechanics and cytoskeletal tension as important regulators of cell function." *Cell Biochemistry and Biophysics* **47,** 300–320 (2007).

57. A. Curtis & C. Wilkinson. "Topographical control of cells." *Biomaterials* **18,** 1573–1583 (1997).

58. M. Berggren & A. Richter-Dahlfors. "Organic Bioelectronics." *Advanced Materials* **19,** 3201–3213 (2007).

59. D.-H. Kim, S. Richardson-Burns, L. Povlich, M. R. Abidian, S. Spanninga, J. L. Hendricks & D. C. Martin. in *Indwelling Neural Implants: Strategies for Contending with the In-Vivo Environment.* (ed W. M. Reichert) 177–220 (CRC Press, 2008).

60. J. Isaksson, P. Kjäll, D. Nilsson, N. D. Robinson, M. Berggren & A. Richter-Dahlfors. "Electronic control of Ca2+ signalling in neuronal cells using an organic electronic ion pump." *Nature Materials* **6,** 673–9 (2007).

61. D. T. Simon, S. Kurup, K. C. Larsson, R. Hori, K. Tybrandt, M. Goiny, E. W. H. Jager, M. Berggren, B. Canlon & A. Richter-Dahlfors. "Organic electronics for precise delivery of neurotransmitters to modulate mammalian sensory function." *Nature Materials* **8,** 742–6 (2009).

62. J. Isaksson, C. Tengstedt, M. Fahlman, N. Robinson & M. Berggren. "A Solid-State Organic Electronic Wettability Switch." *Advanced Materials* **16,** 316–320 (2004).

63. H. G. Othmer, S. R. Dunbar & W. Alt. "Models of dispersal in biological systems." *Journal of Mathematical Biology* **26,** 263–298 (1988).

64. Y.-L. Hu, S. Li, H. Miao, T.-C. Tsou, M. A. del Pozo & S. Chien. "Roles of microtubule dynamics and small GTPase Rac in endothelial cell migration and lamellipodium formation under flow." *Journal of Vascular Research* **39,** 465–76 (2002).

65. X. Lin & B. P. Helmke. "Micropatterned structural control suppresses mechanotaxis of endothelial cells." *Biophysical Journal* **95,** 3066–78 (2008).

66. S. P. Palecek, J. C. Loftus, M. H. Ginsberg, D. A. Lauffenburger & A. F. Horwitz. "Integrin-ligand binding properties govern cell migration speed through cell-substratum adhesiveness." *Nature* **385,** 537–40 (1997).

67. J. T. Smith, J. K. Tomfohr, M. C. Wells, T. P. Beebe, T. B. Kepler & W. M. Reichert. "Measurement of cell migration on surface-bound fibronectin gradients." *Langmuir* **20,** 8279–86 (2004).

68. S. B. Carter. "Haptotaxis and the Mechanism of Cell Motility." *Nature* **213,** 256–260 (1967).

69. E. M. Chandler, M. P. Saunders, C. J. Yoon, D Gourdon & C Fischbach. "Adipose progenitor cells increase fibronectin matrix strain and unfolding in breast tumors." *Physical biology* **8,** 015008 (2011).

70. M. Carrion-Vazquez. "Atomic force microscopy captures length phenotypes in single proteins." *Proceedings of the National Academy of Sciences* **96,** 11288–11292 (1999).

71. A. F. Oberhauser, P. K. Hansma, M. Carrion-Vazquez & J. M. Fernandez. "Stepwise unfolding of titin under force-clamp atomic force microscopy." *Proceedings of the National Academy of Sciences* **98,** 468–472 (2001).

72. C. G. Galbraith, K. M. Yamada & M. P. Sheetz. "The relationship between force and focal complex development." *The Journal of cell biology* **159,** 695–705 (2002).

73. A. del Rio, R. Perez-Jimenez, R. Liu, P. Roca-Cusachs, J. M. Fernandez & M. P. Sheetz. "Stretching Single Talin Rod Molecules Activates Vinculin Binding." *Science* **323,** 638–641 (2009).

74. R. M. Owens & G. G. Malliaras. "Organic Electronics at the Interface with Biology." English. *MRS Bulletin* **35,** 449–456 (2010).

75. K. Svennersten, M. H. Bolin, E. W. H. Jager, M. Berggren & A. Richter-Dahlfors. "Electrochemical modulation of epithelia formation using conducting polymers." *Biomaterials* **30,** 6257–64 (2009).

76. M. Asplund, T. Nyberg & O. Inganäs. "Electroactive polymers for neural interfaces." *Polymer Chemistry* **1,** 1374 (2010).

77. S. Huveneers, H. Truong, R. Fässler, A. Sonnenberg & E. H. J. Danen. "Binding of soluble fibronectin to integrin alpha5 beta1 - link to focal adhesion redistribution and contractile shape." *Journal of Cell Science* **121,** 2452–62 (2008).

78. M. D. Pierschbacher & E Ruoslahti. "Cell attachment activity of fibronectin can be duplicated by small synthetic fragments of the molecule." *Nature* **309,** 30–33 (1984).

79. S Aota, M Nomizu & K. M. Yamada. "The short amino acid sequence Pro-His-Ser-Arg-Asn in human fibronectin enhances cell-adhesive function." *The Journal of Biological Chemistry* **269,** 24756–24761 (1994).

80. E. C. Williams, P. A. Janmey, J. D. Ferry & D. F. Mosher. "Conformational states of fibronectin. Effects of pH, ionic strength, and collagen binding." *The Journal of Biological Chemistry* **257,** 14973–14978 (1982).

81. R. P. Grant, C Spitzfaden, H Altroff, I. D. Campbell & H. J. Mardon. "Structural requirements for biological activity of the ninth and tenth FIII domains of human fibronectin." *The Journal of Biological Chemistry* **272,** 6159–66 (1997).

82. H Altroff, C. F. van der Walle, J Asselin, R Fairless, I. D. Campbell & H. J. Mardon. "The eighth FIII domain of human fibronectin promotes inte-

grin alpha5beta1 binding via stabilization of the ninth FIII domain." *The Journal of Biological Chemistry* **276,** 38885–92 (2001).

83. T. Nyberg, O. Inganas & H. Jerregard. "Polymer Hydrogel Microelectrodes for Neural Communication." *Biomedical Microdevices* **4,** 43–52 (2002).

84. M. H. Bolin, K. Svennersten, X. Wang, I. S. Chronakis, A. Richter-Dahlfors, E. W. Jager & M. Berggren. "Nano-fiber scaffold electrodes based on PEDOT for cell stimulation." *Sensors and Actuators B: Chemical* **142,** 451–456 (2009).

85. A. L. Berrier & K. M. Yamada. "Cell-matrix adhesion." *Journal of cellular physiology* **213,** 565–73 (2007).

86. S. Stenman. "Distribution of a major connective tissue protein, fibronectin, in normal human tissues." *Journal of Experimental Medicine* **147,** 1054–1064 (1978).

87. J. G. Steele, G Johnson & P. A. Underwood. "Role of serum vitronectin and fibronectin in adhesion of fibroblasts following seeding onto tissue culture polystyrene." *Journal of biomedical materials research* **26,** 861–84 (1992).

88. J Labat-Robert. "Fibronectin in malignancy." *Seminars in cancer biology* **12,** 187–95 (2002).

89. C. Gaggioli, G. Robert, C. Bertolotto, O. Bailet, P. Abbe, A. Spadafora, P. Bahadoran, J.-P. Ortonne, V. Baron, R. Ballotti & S. Tartare-Deckert. "Tumor-derived fibronectin is involved in melanoma cell invasion and regulated by V600E B-Raf signaling pathway." *The Journal of investigative dermatology* **127,** 400–10 (2007).

90. T Sethi, R. C. Rintoul, S. M. Moore, A. C. MacKinnon, D Salter, C Choo, E. R. Chilvers, I Dransfield, S. C. Donnelly, R Strieter & C Haslett. "Extracellular matrix proteins protect small cell lung cancer cells against apoptosis: a mechanism for small cell lung cancer growth and drug resistance in vivo." *Nature medicine* **5,** 662–8 (1999).

91. P. Singh, C. Carraher & J. E. Schwarzbauer. "Assembly of fibronectin extracellular matrix." *Annual Review of Cell and Developmental Biology* **26,** 397–419 (2010).

92. A. Subramanian & H.-Y. Lin. "Crosslinked chitosan: its physical properties and the effects of matrix stiffness on chondrocyte cell morphology and proliferation." *Journal of Biomedical Materials Research, Part A* **75,** 742–53 (2005).

93. T. A. Ulrich, E. M. de Juan Pardo & S. Kumar. "The mechanical rigidity of the extracellular matrix regulates the structure, motility, and proliferation of glioma cells." *Cancer Research* **69,** 4167–74 (2009).

94. A. J. Engler, S. Sen, H. L. Sweeney & D. E. Discher. "Matrix elasticity directs stem cell lineage specification." *Cell* **126,** 677–89 (2006).

95. M. J. Paszek, N. Zahir, K. R. Johnson, J. N. Lakins, G. I. Rozenberg, A. Gefen, C. A. Reinhart-King, S. S. Margulies, M. Dembo, D. Boettiger, D. A. Hammer & V. M. Weaver. "Tensional homeostasis and the malignant phenotype." *Cancer Cell* **8,** 241–54 (2005).

96. A. Mammoto, K. M. Connor, T. Mammoto, C. W. Yung, D. Huh, C. M. Aderman, G. Mostoslavsky, L. E. H. Smith & D. E. Ingber. "A mechanosensitive transcriptional mechanism that controls angiogenesis." *Nature* **457,** 1103–8 (2009).

97. P. Carmeliet & R. K. Jain. "Molecular mechanisms and clinical applications of angiogenesis." *Nature* **473,** 298–307 (2011).

98. V Ozeri, A Tovi, I Burstein, S Natanson-Yaron, M. G. Caparon, K. M. Yamada, S. K. Akiyama, I Vlodavsky & E Hanski. "A two-domain mechanism for group A streptococcal adherence through protein F to the extracellular matrix." *The EMBO Journal* **15,** 989–98 (1996).

99. S. Kim, K. Bell, S. A. Mousa & J. A. Varner. "Regulation of Angiogenesis in Vivo by Ligation of Integrin $\alpha 5\beta 1$ with the Central Cell-Binding Domain of Fibronectin." *The American Journal of Pathology* **156,** 1345–1362 (2000).

100. G. Malik, L. M. Knowles, R. Dhir, S. Xu, S. Yang, E. Ruoslahti & J. Pilch. "Plasma fibronectin promotes lung metastasis by contributions to fibrin clots and tumor cell invasion." *Cancer Research* **70,** 4327–34 (2010).

101. H. Xing, Y. Cao, D. Weng, W. Tao, X. Song, W. Wang, L. Meng, G. Xu, J. Zhou, S. Wang & D. Ma. "Fibronectin-mediated activation of Akt2 protects human ovarian and breast cancer cells from docetaxel-induced apoptosis via inhibition of the p38 pathway." *Apoptosis : An International Journal on Programmed Cell Death* **13,** 213–23 (2008).

102. T. A. Petrie, J. R. Capadona, C. D. Reyes & A. J. García. "Integrin specificity and enhanced cellular activities associated with surfaces presenting a recombinant fibronectin fragment compared to RGD supports." *Biomaterials* **27,** 5459–70 (2006).

103. J. C. Friedland, M. H. Lee & D. Boettiger. "Mechanically activated integrin switch controls alpha5beta1 function." *Science* **323,** 642–4 (2009).

104. M. Mitsi, Z. Hong, C. E. Costello & M. A. Nugent. "Heparin-mediated conformational changes in fibronectin expose vascular endothelial growth factor binding sites." *Biochemistry* **45,** 10319–28 (2006).

105. A García. "Integrin–fibronectin interactions at the cell-material interface: initial integrin binding and signaling." *Biomaterials* **20,** 2427–2433 (1999).

106. T. Sun, S. Jackson, J. W. Haycock & S. MacNeil. "Culture of skin cells in 3D rather than 2D improves their ability to survive exposure to cytotoxic agents." *Journal of biotechnology* **122,** 372–81 (2006).

107. H. Baharvand, S. M. Hashemi, S. Kazemi Ashtiani & A. Farrokhi. "Differentiation of human embryonic stem cells into hepatocytes in 2D and 3D culture systems in vitro." *The International journal of developmental biology* **50,** 645–52 (2006).

108. M Pickl & C. H. Ries. "Comparison of 3D and 2D tumor models reveals enhanced HER2 activation in 3D associated with an increased response to trastuzumab." *Oncogene* **28,** 461–8 (2009).

109. M. C. Gutiérrez, M. L. Ferrer & F. del Monte. "Ice-Templated Materials: Sophisticated Structures Exhibiting Enhanced Functionalities Obtained after Unidirectional Freezing and Ice-Segregation-Induced Self-Assembly." *Chemistry of Materials* **20,** 634–648 (2008).

110. S. Deville, E. Saiz, R. K. Nalla & A. P. Tomsia. "Freezing as a path to build complex composites." *Science (New York, N.Y.)* **311,** 515–8 (2006).

111. S. Deville, E. Maire, G. Bernard-Granger, A. Lasalle, A. Bogner, C. Gauthier, J. Leloup & C. Guizard. "Metastable and unstable cellular solidification of colloidal suspensions." *Nature materials* **8,** 966–72 (2009).

112. E. Munch, E. Saiz, A. P. Tomsia & S. Deville. "Architectural Control of Freeze-Cast Ceramics Through Additives and Templating." *Journal of the American Ceramic Society* **92,** 1534–1539 (2009).

113. J. Halloran. "Materials science. Making better ceramic composites with ice." *Science (New York, N.Y.)* **311,** 479–80 (2006).

114. H. Zhang, I. Hussain, M. Brust, M. F. Butler, S. P. Rannard & A. I. Cooper. "Aligned two- and three-dimensional structures by directional freezing of polymers and nanoparticles." *Nature materials* **4,** 787–93 (2005).

115. C. A. L. Colard, R. A. Cave, N. Grossiord, J. A. Covington & S. A. F. Bon. "Conducting Nanocomposite Polymer Foams from Ice-Crystal-Templated Assembly of Mixtures of Colloids." *Advanced Materials* **21,** 2894–2898 (2009).

116. M. C. Gutiérrez, Z. Y. García-Carvajal, M. Jobbágy, F. Rubio, L. Yuste, F. Rojo, M. L. Ferrer & F. del Monte. "Poly(vinyl alcohol) Scaffolds with Tailored Morphologies for Drug Delivery and Controlled Release." *Advanced Functional Materials* **17,** 3505–3513 (2007).

117. M. D. Gawryla, L. Liu, J. C. Grunlan & D. A. Schiraldi. "pH Tailoring Electrical and Mechanical Behavior of Polymer-Clay-Nanotube Aerogels." *Macromolecular Rapid Communications* **30,** 1669–73 (2009).

118. S. M. Alhassan, S. Qutubuddin & D. Schiraldi. "Influence of electrolyte and polymer loadings on mechanical properties of clay aerogels." *Langmuir : the ACS journal of surfaces and colloids* **26,** 12198–202 (2010).

119. L. Estevez, A. Kelarakis, Q. Gong, E. H. Da'as & E. P. Giannelis. "Multifunctional graphene/platinum/Nafion hybrids via ice templating." *Journal of the American Chemical Society* **133,** 6122–5 (2011).

120. X. Zhang, C. Li & Y. Luo. "Aligned/unaligned conducting polymer cryogels with three-dimensional macroporous architectures from ice-segregation-induced self-assembly of PEDOT-PSS." *Langmuir : the ACS journal of surfaces and colloids* **27,** 1915–23 (2011).

121. I. Levental, P. C. Georges & P. A. Janmey. "Soft biological materials and their impact on cell function." en. *Soft Matter* **3,** 299 (2007).

122. M. H. Bolin, K. Svennersten, D. Nilsson, A. Sawatdee, E. W. H. Jager, A. Richter-Dahlfors & M. Berggren. "Active Control of Epithelial Cell-Density Gradients Grown Along the Channel of an Organic Electrochemical Transistor." *Advanced Materials* **21,** 4379–4382 (2009).

123. C. Fischbach & D. Mooney. in *Polymers for Regenerative Medicine* (ed C. Werner) (Springer-Verlag, Berlin/Heidelberg, 2006). doi:10.1007/11604228.

124. C. P. Tan, B. R. Seo, D. J. Brooks, E. M. Chandler, H. G. Craighead & C. Fischbach. "Parylene peel-off arrays to probe the role of cell-cell interactions in tumour angiogenesis." *Integrative biology : quantitative biosciences from nano to macro* **1,** 587–94 (2009).

125. C. D. James, R. C. Davis, L. Kam, H. G. Craighead, M. Isaacson, J. N. Turner & W. Shain. "Patterned Protein Layers on Solid Substrates by Thin Stamp Microcontact Printing". *Langmuir* **14,** 741–744 (1998).

126. R Kane. "Patterning proteins and cells using soft lithography." *Biomaterials* **20,** 2363–2376 (1999).

127. D. Falconnet, D. Pasqui, S. Park, R. Eckert, H. Schift, J. Gobrecht, R. Barbucci & M. Textor. "A Novel Approach to Produce Protein Nanopatterns

by Combining Nanoimprint Lithography and Molecular Self-Assembly." *Nano Letters* **4,** 1909–1914 (2004).

128. J. D. Hoff, L.-J. Cheng, E. Meyhöfer, L. J. Guo & A. J. Hunt. "Nanoscale Protein Patterning by Imprint Lithography." *Nano Letters* **4,** 853–857 (2004).

129. Z. Zhang, T. Chao, S. Chen & S. Jiang. "Superlow fouling sulfobetaine and carboxybetaine polymers on glass slides." *Langmuir : the ACS journal of surfaces and colloids* **22,** 10072–7 (2006).

130. K. Zuber, M. Fabretto, C. Hall & P. Murphy. "Improved PEDOT Conductivity via Suppression of Crystallite Formation in Fe(III) Tosylate During Vapor Phase Polymerization." *Macromolecular Rapid Communications* **29,** 1503–1508 (2008).

131. P. Åsberg, P. Nilsson & O. Inganäs. "Fluorescence quenching and excitation transfer between semiconducting and metallic organic layers." *Journal of Applied Physics* **96,** 3140 (2004).

132. A. Baba, J. Lübben, K. Tamada & W. Knoll. "Optical Properties of Ultrathin Poly(3,4-ethylenedioxythiophene) Films at Several Doping Levels Studied by In Situ Electrochemical Surface Plasmon Resonance Spectroscopy." *Langmuir* **19,** 9058–9064 (2003).